Magnetic Resonance Echo Planar Neuroimaging – Methodological Advances and Current applications in Psychiatry

Manoliu, Andrei

Abstract: Although the burden of mental disorders continues to grow worldwide, their neurobiology still remains insufficiently understood. Over the last quarter century, methodological advances in neuroimaging have transformed the field of neuroscience. The advent of magnetic resonance imaging (MRI) and more particularly the development of echo planar imaging (EPI) pulse sequences, enabled novel applications, including functional magnetic resonance imaging (fMRI) and diffusion weighted/tensor imaging (DWI/DTI). Together, both methods allow for a characterization of the neuronal circuitry, which may serve as a specific biomarker for mental disorders. However, the functional architecture of the human brain remains elusive, while methodological limitations are still hampering our scientific progress. The six articles selected for this habilitation thesis address different aspects of EPI based MR neuroimaging with an emphasis on two main aspects: First, the application of fMRI in clinical populations with mental illness to explore associations between the functional connectome and behaviour, disease course and/or neuropathology. Second, the development and optimization of novel DWI/DTI approaches and their subsequent validation in peripheral neuronal structures. Using fMRI, we found a relationship between altered subcortical-cortical functional connectivity and psychotic symptoms in patients with schizophrenia, described an association between aberrant graph-theoretical network- topology and the course of disease in patients with depression and demonstrated an intricate interaction between brain activity during rest, task, cognitive performance and amyloid- (A) as measured with A -specific positron-emission tomography in patients with prodromal Alzheimer's disease. In addition, we validated the reproducibility of a novel DWI/DTI approach with optimized slice-wise shimming, tested the feasibility and performance of DTI in fine neuronal structures applying a novel readout segmented EPI and evaluated to which extent the acquisition can be accelerated without impeding the data quality. With its two main focuses within the framework of MR EPI neuroimaging, this work presents potential applications of already established methods to investigate the neurobiology underlying mental disorders as well as novel methodological developments in MR neuroimaging. The integration of methodological developments and applications in clinical research settings according to hypotheses derived from clinical observations may allow for the detection of biomarkers, which might have an influence on diagnostics and clinical decision making in the future.

Medizinische Fakultät der Universität Zürich
Psychiatrische Universitätsklinik Zürich
Klinik für Psychiatrie, Psychotherapie und Psychosomatik
Direktor: Prof. Dr. Erich Seifritz

Magnetic Resonance Echo Planar Neuroimaging – Methodological Advances and Current applications in Psychiatry

Kumulative Habilitationsschrift

Zur Erlangung der Venia Legendi an der Universität Zürich

vorgelegt von
Ioan-Andrei Manoliu, Dr. med., Ph.D.
02.04.2018

Table of content

1. Introduction

1.1. Background

Mental disorders are characterized by a combination of abnormal cognitive, affective, perceptive, behavioural and inter-social functions and are associated with relevant functional disability and mortality (1). According to the World Health Organization (WHO), the burden of mental disorders continues to grow worldwide, causing tremendous implications for global health as well as major social, human rights and economic consequences (2). With around 23% of all years lost due to disability, mental disorders are the leading cause of disability worldwide (3). Furthermore, mental disorders represent an important risk factor for other diseases, unintentional and intentional injury and are commonly associated with stigma and discrimination, preventing affected individuals to seek mental health care (4). Historically, this stigma stems mainly from the fact that until recently, an association between psychiatric disorders and neurobiological aspects was insufficiently possible, further nourishing the concept of mind-body-dualism throughout our society and – although to a much lesser extent - even within the field of academic psychiatry. Despite intensive efforts to elucidate the causes of mental disorders at a biological level and to infer on potential targets for treatment, the neurobiology of mental disorders still remains not sufficiently understood.

1.2. Motivation

In contrast to other medical disciplines, professionals working in the field of psychiatry face the unique challenge to perform diagnostics, clinical decision-making, treatment monitoring as well as the assessment of treatment success or failure mainly based on their clinical observations of patients' individual behaviour (5). This issue is largely owed by the absence of established biological measures (i.e. biomarkers), which might yield the potential to provide guidance for clinicians, patients and their supporters (6). Furthermore, the lack of measurable and/or quantifiable biomarkers, which historically separated psychiatric from neurologic disorders, strongly contributed not only to a certain stigmatization of affected individuals, but also to the phenomenon that until a quarter century ago, the sheer idea of examining the human brain as a means to unravel

the mysterious nature of psychiatric illness was regarded as obscure and treated with derision, even within mainstream psychiatry (7).

Correspondingly and in accordance with their historic origin, our current classification systems still define mental illness based on nosological clusters of symptoms rather than underlying pathology (8). However, according to new research, mental disorders may rather represent a behaviourally perceptible common final pathway of various disorders with distinct underlying pathophysiologies (9). Nevertheless, despite wide recognition of this notion, the diagnostic process remains entrenched in the concept of categorical classifications, and succeeding treatment selection relies predominantly on a trial-and-error process (10). To address this problem, the National Institute of Mental Health proposed with the Research Domain Criteria (RDoC) project a framework for trans-dimensional classification systems that transcend traditional diagnostic categories (11). The RDoC project aspired to identify specific behaviours and their distinct underlying neural circuits (12). Those features are referred to as "endophenotypes" and are suggested to represent a better fit for the complex interaction between neurobiology and environment compared to current diagnostic classifications (13).

Historically, clinical neuroscience was divided between the concept of localism, which stems from classical lesion studies and perceives the brain as a set of discrete processing modules, and the concept of processing distribution, which stems from theories of equipotentiality and postulates a complete distribution of neurocognitive functions throughout the brain (14). With the rise of modern neuroimaging and the novel possibility to investigate the connectome (i.e. comprehensive map of neural connections in the brain), the newly described dynamic spatiotemporal models provided a framework that reconciled these two concepts and may serve to unravel sensitive biomarkers for mental disorders as proposed within the RDoC project (15). In the healthy brain, network nodes (i.e. distinct brain regions) serve as elements within highly interactive networks responsible for processing a wide variety of cognitive, emotional and behavioural processes (16). While some nodes are specialized in mediating locally specific processes (such as the primary motor cortex), other nodes are rather mediating global network activities (such as the anterior insular cortex / anterior cingulate cortex, which mediate the switching between self-referential, internally oriented and goal-oriented, externally oriented brain networks) (17).

The detection and investigation of such large-scale brain networks associated with distinct neurocognitive functions is of utmost interest with respect to our understanding of the neurobiological underpinnings of mental disorders. In addition, such biomarkers may not only serve as symptom/syndrome/disease-specific biomarkers that might be included in the diagnostic process, but may also be used for risk identification or prediction of treatment response in a trans-diagnostic fashion within the framework of personalized medicine, analogous to what is done today routinely in other areas of clinical medicine, such as oncology (18).

1.3. Theoretical and methodological considerations

Due to constant methodological advances over the last quarter century, modern neuroimaging enabled the investigation of large-scale neuronal networks and transformed the field of neuroscience. The functional imaging revolution began in the 1980s, when first research and medical centres came to use a new method called positron emission tomography (PET) to detect and quantify regional cerebral metabolism using radiolabelled glucose (18-fluorodeoxyglucose; FDG-PET) or regional cerebral blood flow (rCBF) using radiolabelled oxygen (H2-15-O-PET). The scientific outputs derived from these approaches provided primarily resting-state investigations with an emphasis on physiological quantification of blood flow and metabolism, providing our first insights into neural circuit dysfunction associated with mental disorders or syndromes/symptoms in a regionally specific fashion (5). Using specific tracers, such as thioflavine-T-derivate [^{11}C]6-OH-BTA-1 (Pittsburgh Compound-B, PiB), whose binding is dominated by the amyloid component, and not by other aspects, such as Tau-pathology, PET can also be used to measure amyloid plaque deposition in vivo in neurodegenerative disorders, such as Alzheimer's disease (19).

Around the same time, magnetic resonance imaging (MRI), a method that proved pivotal in shaping the landscape of today's neuroimaging, was introduced (20). In general, MRI exploits the interaction between biological tissue, static/dynamic electromagnetic fields and radiofrequency (RF) pulses to generate and detect signals. The measured signal is recorded in a temporary image space referred to as k-space, where each point of the

resulting matrix encodes specific frequency, phase and signal intensity information (21). Inverse Fourier transformation is performed, resulting in the final image of the measured biological tissue (22). Although this method provided the possibility to depict high-resolution anatomical brain images of patients with mental disorders in vivo without using radiation for the first time, the temporal resolution of this technique was still not sufficient to reliably detect and analyse neurophysiological signals, which would be necessary to infer on the functional neuronal circuitry.

Echo planar imaging (EPI), a very fast magnetic resonance (MR) imaging technique capable of acquiring an entire MR image in only a fraction of a second, fulfils this requirement by using an intricate train of gradient echoes for spatial encoding (23). In particular, EPI pulse sequences acquire multiple lines of imaging data within the k-space after one single RF excitation. The development and wide implementation of this technique around the 1990s set the stage for two EPI-based applications, which are crucial for modern neuroimaging and reshaped the landscape of psychiatric research: functional MRI (fMRI) and diffusion weighted MRI (DWI) (24).

Functional Magnetic resonance imaging (fMRI) represents one application method of EPI and can be applied to infer on mental activity under physiological and/or pathological conditions by exploiting the interrelation between physiological processes, metabolism and blood supply (25). In general, neuronal activation is associated with changes in cerebral blood flow (CBF), cerebral blood volume (CBV), cerebral blood oxygenation (CBO2) and cerebral metabolism (26, 27). According to suggested models, signalling in neurons and astrocytes trigger the hemodynamic response (HR), i.e. vasoactive cascades to arterioles and capillaries, resulting in dilatation of upstream arterial vessels and a consecutive increase in CBF. Since CBF increases to a relatively larger extent that the cerebral metabolic rate of oxygen utilization (CMRO2), the ratio between oxygenated hemoglobin (O2-Hb) and deoxygenated hemoglobin (dO2-Hb) increases in relation to the baseline state (28). Due to different magnetic properties of O2-Hb and dO2-Hb, a signal decay can be measured when performing gradient-echo EPI sequences, which is referred to as blood oxygenated level-dependent (BOLD) signal (29, 30). This signal can subsequently be used in a great variety of ways to infer on the sought-after functional architecture of the human brain, including statistical analyses of brain activation patterns during specific tasks or even during rest, where synchronous co-activity between

different brain regions is regarded as a marker for functional connectivity (FC) within distinct intrinsic connectivity networks (ICN) (31). To measure brain activity associated with discrete states of mind is one of the greatest aims of cognitive neuroscience (7). When performed with sufficient temporal resolution, differences in spatiotemporal properties of the connectome can provide insight into transient or dynamic states that may relate to internal states of mind (32). In contrast, resting-state fMRI, which is assessed over a continous duration of time, provides insights regarding the connectome properties during steady-state, which might improve our understanding regarding certain neurobiological traits distinguishing health from disease (33). Therefore, application of this technique can be used to detect and analyse specific brain networks in such a way that findings may contribute to our understanding of the observed clinical phenomenology, course of disease and possibly even treatment response (34).

Another application method of EPI sequences is diffusion weighted imaging (DWI), which detects the degree of thermally driven Brownian motion of molecules in fluids along specific directions to infer on different properties of neuronal microstructure (35). Diffusion tensor imaging (DTI), which is based on DWI, derives estimates of water diffusion in a specific tissue using voxel-wise calculations of tissue fiber orientation on the basis of tensor as a 3-dimensional ellipsoid model (36). The quantitative degree of water diffusion anisotropy can be described by the fractional anisotropy (FA), which can provide a characterization of the investigated white matter (for instance, reduced FA values were observed in peripheral nerves under abnormal conditions associated with Wallerian degeneration (37)). Using fiber tractography, aforementioned data can be used to determine the course as well as various properties of axonal structures within the brain to infer on the underlying structural connectome, both in health and mental disorder (38). However, it is to note that performing DTI / fiber tractography in the brain still yields several challenges due to considerable limitations of the aforementioned tensor model in brain tissue, which are mainly explained by the incapability of currently widely used DWI/DTI pulse sequences and/or tensor models to truthfully assess axonal structures in the presence of complex axonal geometries, which are frequent in the human brain (39). For instance, while in peripheral nerves, where bundles of axons run in parallel in one principal direction and the nerve surrounding myelin sheaths limit the diffusion of water molecules in perpendicular directions (37), performing DTI in the brain still yields several challenges due to considerable limitations of the aforementioned tensor model in brain

tissue, which consists largely of regions characterized by complex axonal geometries that might confound calculated results. Given this observation, the design of new pulse sequences (with increased performance, such as increased acquisition speed (40) or spatial resolution (35)), novel analysis methods (with a greater sensitivity towards the representation of underlying axonal structures, such as the calculation of fiber density (FD) (41)) or both are mandatory in addition to hardware-optimization (42–44) in order to reliably investigate the structural connectome of the human brain in future studies.

1.4. Own work and motivation of the current habilitation thesis.

Less than 25 years since its inception, the field of neuroimaging, using fMRI and DTI, has reached a high level of maturity and methodological sophistication. Nevertheless, many questions regarding the functional architecture of the human brain remain elusive, while methodological challenges are still hampering our scientific progress. During my research career, I have had the opportunity to work within two main domains equally relevant for modern Neuroimaging: I applied EPI-based BOLD fMRI to assess novel trans-diagnostic properties of the connectome in mental disorders and conceptualized novel EPI-based DWI/DTI techniques, which I successfully validated in peripheral nerves.

Accordingly, the six articles selected for this habilitation thesis address different aspects of echo planar imaging pulse sequences in magnetic resonance neuroimaging with an emphasis on two main aspects: First, the application of EPI BOLD fMRI in clinical populations with mental disorders with a focus on the correlation between the functional connectome, symptoms/behaviour, clinical disease course and/or neuropathology. Second, the conceptualization and validation of novel EPI DWI/DTI sequences, which aim to optimize the performance of applied diffusion pulse sequences for neuroimaging.

2. Summary of included papers

Article 1: „Reduced functional connectivity between putamen and right anterior insula in psychotic patients with schizophrenia", British Journal of Psychiatry, 2017. (IF = 6.347)

Schizophrenia is characterized by striatal dopaminergic dysfunction and aberrant subcortical connectivity. During psychosis, which is characterized by positive symptoms such as delusions or hallucinations, connectivity is altered within the dorsal striatum, while during remission, which might be accompanied by negative symptoms such as anhedonia or apathy, connectivity is altered within the ventral striatum (45). Furthermore, functional connectivity within and between core cortical brain networks, including the Default-Mode-Network (DMN), Salience Network (SN) and Central Executive Network (CEN) are altered in individuals with schizophrenia during psychosis and remission (31, 46). However, a potential interaction between these findings has not been found to date. In this work, we hypothesized that the functional connectivity of the putamen shows aberrant distinctiveness with respect to cortical regions. To test this hypothesis, we acquired resting-state fMRI images using a gradient-echo EPI in 21 patients with schizophrenia during psychosis and a control group of 42 healthy individuals. To assess intrinsic functional connectivity, we performed seed-based connectivity analysis on the preprocessed data. We found that patients showed a decreased functional connectivity between the putamen and the right anterior insular cortex, the putamen and the dorsal prefrontal cortex and the ventral striatum and the left anterior insular cortex. Furthermore, the connectivity between the putamen and the right anterior insular cortex correlated with the severity of hallucinations, even after correcting for possible confounders, such as age, gender or the amount of antipsychotic (antidopaminergic) medication. These results demonstrate aberrant subcortical-cortical connectivity between the striatum and important cortical structures, which are involved in the mediation of context-dependent switching between brain networks mediating self-referential and goal-oriented behaviour in patients with schizophrenia. Most importantly, our results provide further evidence for the "aberrant salience hypothesis" of schizophrenia, which might have implications regarding the future development of targeted therapies (47).

Article 2: „Aberrant topology of striatum´s connectivity is associated with the number of episodes in depression", Brain, 2014. (IF = 10.292)

With a lifetime prevalence of 16% major depressive disorder (MDD) is one of the most frequent psychiatric disorders (48). In 35–85% of cases the course of MDD contains the recurrence of depressive episodes, whereas the number of depressive episodes is one of the most important predictors for relapse (49). However, our understanding regarding neuronal mechanisms contributing to relapse is still incomplete. Since recent research provided evidence that aberrant connectivity (50) and altered topological network properties of brain networks, such as modularity (i.e. the organization of regions with increased functional connectivity within the respective modules) might be associated with disease load (51), we hypothesized that aberrant topological characteristics of neural networks might be associated with the course of disease in MDD. To investigate this hypothesis, we acquired resting-state fMRI data in 25 patients with MDD and 25 controls. Based on the acquired data, we performed wavelet-transformation to decompose the residual regional time series in distinct frequency scales and calculated wavelet-correlation matrices for the frequency scale in the range of 0.060-0.125Hz across different brain regions, resulting in a connectivity matrix representing individual whole brain functional connectivity for each subject, respectively. Subsequently, we performed a graph-based analysis, which yielded distinct outcome measures as surrogate of intrinsic network topology, including global topological properties of path length, global efficiency and global betweeness-centrality (reflecting functional integration) as well as clustering coefficient and small-worldness (reflecting functional segregation and it's relation to functional integration). In general, we found that for patients with MDD, global efficiency was reduced and global betweenness-centrality was increased, while small-world topology was preserved. Furthermore, aberrant nodal efficiency and centrality of regional connectivity was found in the dorsal striatum, inferior frontal and orbitofrontal cortex. Inferior frontal alterations were associated with current symptoms, while aberrant network topology of the right putamen was associated with the number of episodes, even when controlling for grey matter volume, medication and total disease duration. These results provide first evidence that aberrant subcortical network topology is associated with the course of disease and contributes to relapse risk in MDD, which might contribute to future developments for predicting the course of disease.

Article 3: „Disrupted intrinsic networks link Amyloid-beta Pathology and Impaired Cognition in Prodromal Alzheimer´s Disease", Cerebral Cortex, 2015. (IF = 6.559)

Contributing to around 60% of cases, Alzheimer's disease (AD) is the most frequent cause auf dementia (52). AD is inter alia characterized by impaired cognition and Amyloid-β pathology (Aβ), but the mechanisms linking these two observations are still not fully understood. Recent studies showed that in patients with AD, intrinsic brain networks are altered, affected by Aβ pathology and involved in aberrant information processing (53). Therefore, we hypothesized in this work, that regional changes of distinct brain networks, which persist during rest and cognitive tasks, might link Aβ with aberrant cognitive performance in AD. To test this hypothesis, we assessed patients with pro-dromal AD (pAD; i.e., with mild cognitive impairment and biological signs of AD) and healthy older adults by resting-state functional MRI (rs-fMRI) to identify intrinsic connectivity networks, task-fMRI (during an attention-demanding task with different difficulty levels) to reveal network-relevant changes in consistent for attention-relevant task- and rest-states, positron emission tomography (PET) imaging using the tracer [11C]-Pittsburgh compound B (PiB, a radioactive analog of thioflavin T, which is a selective marker for Aβ-plaques in neuronal tissue) to estimate Aβ-pathology load via PiB-uptake in vivo, and neuro-psychological assessment to estimate general cognitive performance. Independent component analysis (ICA) of fMRI data was used to quantify the networks' connectivity pattern during rest and task and correlated with Aβ-load as well as behavioural data. We found that compared to healthy controls, patients with pAD showed reduced functional connectivity during rest as well as increased functional connectivity during the attention-demanding task in the medial parietal cortex within the Default-Mode-Network. Furthermore, functional connectivity in this region was associated with the severity of patients' cognitive impairment and local PiB-uptake. In addition, similar results were found within the right lateral parietal region of an attentional network. Lastly, structural equation modelling demonstrated a direct influence of the resting-state functional connectivity within the DMN on the association between Aβ-pathology and cognitive impairment. These results provide evidence that disrupted intrinsic network connectivity links Aβ-pathology with cognitive impairment in early AD, which extends our knowledge about AD and might contribute to the development of methods for disease detection and monitoring in (prodromal) AD.

Article 4: "Evaluation of reproducibility of diffusion tensor imaging in the brachial plexus at 3.0 Tesla", Investigative Radiology, 2017. (IF = 5.195)

Due to the capability to provide insights into neuronal microstructure, DWI / DTI have not only been used to assess structural connectivity in the human brain, but also to visualize and assess the structural integrity of neuronal structures in general. For instance, DTI can be used to quantitatively assess distinct properties of peripheral nerves or nerve roots (35). In general, DWI/DTI, particularly fiber tractography in neuronal tissue proves to be methodological challenging due to many aspects, including the small size of the target structures (and subsequent lower signal-to-noise ratio (SNR)), susceptibility to partial volume effects and increased distortion effects caused by the heterogeneous nature of the anatomical surroundings. Furthermore, EPI quality suffers from the presence of residual fat signal as well as from local B0 field inhomogeneities due to its intrinsically low bandwidth along the phase-encoding direction. Until recently, established shim procedures (i.e. procedures aiming to homogenize the B0 field) used single, static settings of first (or high-order) shim fields according to average optimization criteria throughout the complete measurement for all acquired image slices. In this study, we aimed to test the feasibility of DWI/DTI applying a novel EPI pulse sequence prototype supporting localized, slice-specific shim optimizations through switching shim settings synchronously with the acquisition of each slice. To test and validate the data quality achieved with slice-specific shimming, we investigated the reproducibility of DTI parameter measurements, more particularly fractional anisotropy (FA) and mean diffusivity (MD) values in the nerve roots of the brachial plexus (C5 to T1) by scanning ten healthy volunteers twice. The DTI scans were performed with b-values of 0 and 800 s/mm^2 in 30 gradient directions. After the first scan, the scan was repeated a second time using identical scan parameters for each subject on the same day in the same scanner (including repositioning of the volunteer, coil replacement and acquisition of new localizer scans). All datasets were analyzed by 2 independent readers. Intra-reader, inter-reader and test-retest showed excellent reproducibility of FA and MD values in almost all levels of the trunks of the brachial plexus. These results demonstrated, that slice-specific shimming represents a promising approach to increase EPI-acquired DWI/DTI data quality and reproducibility in the future, which could also be used to investigate neuronal tissue in the brain, particularly with respect to a wide range of neuropsychiatric diseases.

Article 5: „MR neurographic orthopantomogram: Ultra-short echo-time (UTE) imaging of the mandibular bone and teeth complemented with high-resolution morphological and functional MR neurography“, Journal of Magnetic Resonance Imaging, 2016. (IF = 3.083)

Compared to the brachial plexus, DWI/DTI imaging of cranial nerves and their branches, such as the inferior alveolar nerve (IAN), which is a branch of the mandibular nerve (which itself is a branch of the trigeminal nerve) can be considered as even more challenging. For instance, such structures are very small, which requires a high spatial resolution. Furthremore, structural inhomogeneities as the oral cavity induce massive susceptibility artifacts. Normal EPI pulse sequences use whole k-space sampling following a single excitation, resulting in longer echo-times and thus increased susceptibility to artifacts due to spin dephasing. In contrast, a novel method referred to as readout segmented EPI (rs-EPI) uses multiple excitations with segmented k-space acquisitions in readout direction, which allows a considerable shortening of the echo-spacing/echo time which subsequently results in reduced susceptibility artifacts and T2-blurring but comes at the cost of longer acquisition times. In this work, we evaluated the feasibility of performing DTI imaging of the IAN in 10 healthy volunteers using a simultaneous multislice (SMS) acceleration technique for rs-EPI and correlated the results with selective structural imaging of the IAN by performing a steady-state precession pulse sequence with inherent vascular signal suppression (3D-PSIF) in addition to a standard sequences for neural tissue characterization (Sampling Perfection with Application optimized Contrasts using different flip angle evolution with short tau inversion recovery (3D T2W SPACE STIR)) as well as an ultra-short echo time sequence (pointwise Encoding Time reduction with radial acquisition, 3D-PETRA) for imaging the cortical bone and thus the mandibular canal. Merging morphological and functional images resulted in an MR neurographic orthopantomogram without artifacts. DTI-based fiber tractography revealed physiological quantitative DTI values for the bilateral IAN, including FA and MD. The demonstrated technique provides evidence for the feasibility of robust EPI-based DTI even in small neuronal structures, which – together with additional structural data derived from other pulse sequences, can be used to perform a comprehensive assessment of neural microarchitecture and its surroundings. This method might be of high interest in order to truthfully delineate axonal structures in the presence of complex axonal geometries, which are common in the human brain (39).

Article 6: "Simultaneous multislice-readout segmented echo planar imaging for accelerated diffusion tensor imaging of the mandibular nerve : A feasibility study", Journal of Magnetic Resonance Imaging, 2017. (IF = 3.083)

As discussed above, readout segmented EPI (rs-EPI) sequences divide the k-space trajectory into multiple segments in the readout direction, which allows for an encoding-time reduction and therefore a greater robustness regarding susceptibility artifacts (35). However, this technique comes at the cost of increased scan time, since every segment in k-space requires a separate radiofrequency pulse (54). The technique of simultaneous multislice (SMS) acquisition with blipped controlled aliasing in parallel imaging (blipped-CAIPI) represents a novel approach to reduce scantime for rs-EPI. In the current study, we investigated whether the combination of rs-EPI and SMS with blipped-CAIPI provides a robust acquisition of DWI/DTI data of the IAN, even when increasing the accelerations to higher factors, such as a three-fold acceleration. To test the feasibility of this novel technique, we performed DTI-based fiber tractography of the IAN in eight healthy volunteers. We assessed signal-to-noise ratio (SNR), FA, MD as well as the number of calculated tracts. Artifacts were evaluated qualitatively on Likert scales. To avoid individual bias, all analyses were performed by two independent readers. In order to test for potential signal loss due to movement, which occurs more frequently in patients, we additionally tested the clinical feasibility of accelerated rs-EPI in four patients with pain symptoms or incidental findings. In contrast to conventional rs-EPI, two-fold accelerated rs-EPI yielded similar SNR, FA and MD values as well as similar number of calculated tracts. In contrast, fiber tractography based on three-fold accelerated rs-EPI yielded lower SNR, MD and decreased number of calculated tracts. Likewise, two-fold accelerated rs-EPI sequences did not result in increased artifacts, while three-fold accelerated rs-EPI yielded stronger artifacts and lower overall image quality compared to conventional and two-fold accelerated rs-EPI. These results illustrate that the application of intricate techniques to increase acquisition speed for DTI is feasible and might either contribute to an increased acquisition time in diffusion imaging, which might be of particular interest for neuroimaging in populations with mental disorders, since participants with severe mental illness usually experience difficulties during scans of long duration. This notion is further supported by the successful test of this technique in patients with chronic and/or fulminant pain symptoms.

3. Conclusion and personal outlook

The articles of the current habilitation thesis illuminated various aspects of magnetic resonance echo planar neuroimaging, ranging from the application of established methods to investigate the neurobiology underlying mental disorders to the validation and optimization of methodological developments to enhance the performance of current neuroimaging methods.

Using EPI fMRI, we assessed neuroimaging-derived biomarkers in terms of aberrant subcortical-cortical functional connectivity in patients with schizophrenia, described a functional biomarker associated with the course of disease in patients with MDD based on graph-theoretical analysis of neuroimaging data and demonstrated the intricate interaction between brain activity during rest, brain activity during task, cognitive performance and neuropathological disease load as measured with PiB-PET in patients with prodromal AD. In addition, we validated the reproducibility of a novel EPI DWI/DTI approach with optimized slice-wise shimming, tested the feasibility and performance of DTI in fine neuronal structures applying a novel readout segmented EPI and evaluated, to which extent the acquisition can be accelerated without impeding the data quality given the application of simultaneous multislice excitation technique for readout segmented EPI pulse sequences. All these techniques might contribute to improving diffusion imaging in clinical populations.

The main purpose of the presented research was two-fold: On the one hand to ask and answer novel questions regarding the large-scale neurocircuitry in patients with mental disorders using established, robust and reliable methods, such as fMRI. On the other hand, to push the methodological boundaries in neuroimaging by establishing and further optimizing novel methodological approaches through investigating well described structures (such as distinct diffusion properties of peripheral neuronal structures). Logically, the multimodal integration of methodological developments and applications in clinical research settings according to hypotheses derived from clinical observations is essential to answer the open questions in psychiatric research.

In order to use synergistic effects between method development and clinical research, an appropriate training in both disciplines is beneficial and corresponding expertise has to

be promoted. In addition to the personal formation on an individual level, a strong interdisciplinary academic exchange is mandatory to answer the imminent academic questions in the field of psychiatry. Given the fast developments in computer and software technology as well as continuous methodological advances in the fields of physics and bioengineering, collaboration rather than competition might become the key to successful science in the future. During my research career, I always worked in transdisciplinary groups and promoted interdisciplinary collaborations between clinical research in psychiatry and basic methodological research. I strongly believe that we are living in an era of change with respect to our understanding of mental disorders and that current scientific advances will likely have a considerable impact on our future clinical work.

My personal long-term motivation is to generate, validate and apply novel interdisciplinary methods to contribute to the best of my abilities to the improvement of our understanding of mental disorders and to translate these insights into clinical practice with respect to diagnosis, risk identification and treatment response prediction. To this end, my forthcoming SNSF-funded research stay at the Max-Planck UCL centre for computational psychiatry and the Wellcome Trust Centre for Neuroimaging at the University College London, UK, will complement my education in MR neuroimaging by providing an exceptional environment to learn sophisticated experimental designs and computational psychiatry techniques from internationally leading scientists in an inspiring interdisciplinary environment. After my return to the Psychiatric University Hospital Zurich, I will not only apply my newly acquired knowledge in patient populations, but also diffuse my acquired knowledge to colleagues and students at the University of Zurich through collaboration and teaching. Behind this lies the vision to improve treatment quality in psychiatry and, eventually, the quality of life of our patients.

4. References

1. Association AP. Diagnostic and Statistical Manual of Mental Disorders, Fourth Edition, Text Revision (DSM-IV-TR), Washington, DC, USA. 2000
2. Kessler RC, Berglund P, Demler O, Jin R, Merikangas KR, Walters EE. Lifetime prevalence and age-of-onset distributions of DSM-IV disorders in the National Comorbidity Survey Replication. Arch Gen Psychiatry. 2005;62:593-602.
3. GBD DAIIAPC. Global, regional, and national incidence, prevalence, and years lived with disability for 328 diseases and injuries for 195 countries, 1990-2016: a systematic analysis for the Global Burden of Disease Study 2016. Lancet. 2017;390:1211-1259.
4. Wainberg ML, Scorza P, Shultz JM et al. Challenges and Opportunities in Global Mental Health: a Research-to-Practice Perspective. Curr Psychiatry Rep. 2017;19:28.
5. Neuroimaging in psychiatry: bringing neuroscience into clinical practice. [editorial]. Br J Psychiatry 2012;201(1):1.
6. Silbersweig DA, Rauch SL. Neuroimaging in Psychiatry: A Quarter Century of Progress. Harv Rev Psychiatry. 2017;25:195-197.
7. Dolan RJ. Neuroimaging of cognition: past, present, and future. Neuron. 2008;60:496-502.
8. Hyman SE. Can neuroscience be integrated into the DSM-V. Nat Rev Neurosci. 2007;8:725-732.
9. Pizzagalli DA. Depression, stress, and anhedonia: toward a synthesis and integrated model. Annu Rev Clin Psychol. 2014;10:393-423.
10. Stephan KE, Bach DR, Fletcher PC et al. Charting the landscape of priority problems in psychiatry, part 1: classification and diagnosis. Lancet Psychiatry. 2016;3:77-83.
11. Insel TR. The NIMH Research Domain Criteria (RDoC) Project: precision medicine for psychiatry. Am J Psychiatry. 2014;171:395-397.
12. Cuthbert BN, Insel TR. Toward the future of psychiatric diagnosis: the seven pillars of RDoC. BMC Med. 2013;11:126.
13. Insel TR, Cuthbert BN. Medicine. Brain disorders? Precisely. Science. 2015;348:499-500.
14. Matthews PM, Hampshire A. Clinical Concepts Emerging from fMRI Functional Connectomics. Neuron. 2016;91:511-528.
15. Sprooten E, Rasgon A, Goodman M et al. Addressing reverse inference in psychiatric neuroimaging: Meta-analyses of task-related brain activation in common mental disorders. Hum Brain Mapp. 2017;38:1846-1864.
16. Bassett DS, Sporns O. Network neuroscience. Nat Neurosci. 2017;20:353-364.
17. Seeley WW, Menon V, Schatzberg AF et al. Dissociable intrinsic connectivity networks for salience processing and executive control. J Neurosci. 2007;27:2349-2356.

18. Aggarwal S. Targeted cancer therapies. Nat Rev Drug Discov. 2010;9:427-428.
19. Drzezga A, Grimmer T, Henriksen G et al. Imaging of amyloid plaques and cerebral glucose metabolism in semantic dementia and Alzheimer's disease. Neuroimage. 2008;39:619-633.
20. Mansfield P, Maudsley AA. Medical imaging by NMR. Br J Radiol. 1977;50:188-194.
21. Pruessmann KP, Weiger M, Scheidegger MB, Boesiger P. SENSE: sensitivity encoding for fast MRI. Magn Reson Med. 1999;42:952-962.
22. Pruessmann KP, Weiger M, Bornert P, Boesiger P. Advances in sensitivity encoding with arbitrary k-space trajectories. Magn Reson Med. 2001;46:638-651.
23. Mansfield P, Coxon R, Glover P. Echo-planar imaging of the brain at 3.0 T: first normal volunteer results. J Comput Assist Tomogr. 1994;18:339-343.
24. Poustchi-Amin M, Mirowitz SA, Brown JJ, McKinstry RC, Li T. Principles and applications of echo-planar imaging: a review for the general radiologist. Radiographics. 2001;21:767-779.
25. Bandettini PA. Functional MRI: A confluence of fortunate circumstances. Neuroimage. 2012
26. Bandettini PA, Kwong KK, Davis TL et al. Characterization of cerebral blood oxygenation and flow changes during prolonged brain activation. Hum Brain Mapp. 1997;5:93-109.
27. Kwong KK, Belliveau JW, Chesler DA et al. Dynamic magnetic resonance imaging of human brain activity during primary sensory stimulation. Proc Natl Acad Sci U S A. 1992;89:5675-5679.
28. Fox PT, Raichle ME. Focal physiological uncoupling of cerebral blood flow and oxidative metabolism during somatosensory stimulation in human subjects. Proc Natl Acad Sci U S A. 1986;83:1140-1144.
29. Ogawa S, Lee TM, Kay AR, Tank DW. Brain magnetic resonance imaging with contrast dependent on blood oxygenation. Proc Natl Acad Sci U S A. 1990;87:9868-9872.
30. Ogawa S. Finding the BOLD effect in brain images. Neuroimage. 2012;62:608-609.
31. Manoliu A, Riedl V, Zherdin A et al. Aberrant dependence of default mode/central executive network interactions on anterior insular salience network activity in schizophrenia. Schizophr Bull. 2014;40:428-437.
32. Spiers HJ, Maguire EA. Decoding human brain activity during real-world experiences. Trends Cogn Sci. 2007;11:356-365.
33. Smith SM, Fox PT, Miller KL et al. Correspondence of the brain's functional architecture during activation and rest. Proc Natl Acad Sci U S A. 2009;106:13040-13045.
34. Brakowski J, Spinelli S, Dörig N et al. Resting state brain network function in major depression - Depression symptomatology, antidepressant treatment effects, future research. J Psychiatr Res. 2017;92:147-159.
35. Manoliu A, Ho M, Nanz D et al. Diffusion Tensor Imaging of Lumbar Nerve Roots: Comparison Between Fast Readout-Segmented and Selective-Excitation Acquisitions. Invest Radiol. 2016;51:499-504.

36. Basser PJ, Jones DK. Diffusion-tensor MRI: theory, experimental design and data analysis - a technical review. NMR Biomed. 2002;15:456-467.
37. Ho MJ, Manoliu A, Kuhn FP et al. Evaluation of Reproducibility of Diffusion Tensor Imaging in the Brachial Plexus at 3.0 T. Invest Radiol. 2017;52:482-487.
38. Fornito A, Zalesky A, Breakspear M. The connectomics of brain disorders. Nat Rev Neurosci. 2015;16:159-172.
39. Jeurissen B, Leemans A, Tournier JD, Jones DK, Sijbers J. Investigating the prevalence of complex fiber configurations in white matter tissue with diffusion magnetic resonance imaging. Hum Brain Mapp. 2013;34:2747-2766.
40. Manoliu A, Ho M, Piccirelli M et al. Simultaneous multislice readout-segmented echo planar imaging for accelerated diffusion tensor imaging of the mandibular nerve: A feasibility study. J Magn Reson Imaging. 2017
41. Stämpfli P, Sommer S, Czell D et al. Investigation of Neurodegenerative Processes in Amyotrophic Lateral Sclerosis Using White Matter Fiber Density. Clin Neuroradiol. 2018
42. Manoliu A, Spinner G, Wyss M et al. Magnetic Resonance Imaging of the Temporomandibular Joint at 7.0 T Using High-Permittivity Dielectric Pads: A Feasibility Study. Invest Radiol. 2015
43. Manoliu A, Spinner G, Wyss M et al. Quantitative and qualitative comparison of MR imaging of the temporomandibular joint at 1.5 Tesla and 3.0 Tesla using an optimized high-resolution protocol. Dentomaxillofac Radiol. 201520150240.
44. Manoliu A, Spinner G, Wyss M et al. Comparison of a 32-channel head coil and a 2-channel surface coil for MR imaging of the temporomandibular joint at 3.0 Tesla. Dentomaxillofac Radiol. 201620150420.
45. Sorg C, Manoliu A, Neufang S et al. Increased intrinsic brain activity in the striatum reflects symptom dimensions in schizophrenia. Schizophr Bull. 2013;39:387-395.
46. Manoliu A, Riedl V, Doll A et al. Insular Dysfunction Reflects Altered Between-Network Connectivity and Severity of Negative Symptoms in Schizophrenia during Psychotic Remission. Front Hum Neurosci. 2013;7:216.
47. Dopamine and the aberrant salience hypothesis of schizophrenia. [editorial]. World Psychiatry 2016;15(1):3.
48. Manoliu A, Bosch OG, Brakowski J, Brühl AB, Seifritz E. The potential impact of biochemical mediators on telomere attrition in major depressive disorder and implications for future study designs: A narrative review. J Affect Disord. 2018;225:630-646.
49. Hardeveld F, Spijker J, De Graaf R, Nolen WA, Beekman AT. Recurrence of major depressive disorder and its predictors in the general population: results from the Netherlands Mental Health Survey and Incidence Study (NEMESIS). Psychol Med. 2013;43:39-48.
50. Manoliu A, Meng C, Brandl F et al. Insular dysfunction within the salience network is associated with severity of symptoms and aberrant inter-network connectivity in major

depressive disorder. Front Hum Neurosci. 2013;7:930.

51. Tao H, Guo S, Ge T et al. Depression uncouples brain hate circuit. Mol Psychiatry. 2013;18:101-111.
52. Ferri CP, Prince M, Brayne C et al. Global prevalence of dementia: a Delphi consensus study. Lancet. 2005;366:2112-2117.
53. Myers N, Pasquini L, Göttler J et al. Within-patient correspondence of amyloid-β and intrinsic network connectivity in Alzheimer's disease. Brain. 2014;137:2052-2064.
54. Manoliu A, Ho M, Nanz D et al. MR neurographic orthopantomogram: Ultrashort echo-time imaging of mandibular bone and teeth complemented with high-resolution morphological and functional MR neurography. J Magn Reson Imaging. 2016

5. Reprints of discussed publications

1. Peters H, Riedl V, **Manoliu A**, Scherr M, Schwerthöffer D, Zimmer C, Förstl H, Bäuml J, Sorg C, Koch K: „Reduced functional connectivity between putamen and right anterior insula in psychotic patients with schizophrenia“, Br J Psychiatry. 2017;210(1):75-82, IF = 6.347

2. Meng C, Brandl F, Tahmasian M, Shao J, **Manoliu A**, Scherr M, Schwerthöffer D, Bäuml J, Förstl H, Zimmer C, Wohlschläger AM, Riedl V, Sorg C: „Aberrant topology of striatum´s connectivity is associated with the number of episodes in depression“, Brain. 2014;137(Pt 2):598-609, IF = 10.292

3. Koch K, Myers NE, Göttler J, Pasquini L, Grimmer T, Förster S, **Manoliu A**, Neitzel J, Kurz A, Förstl H, Riedl V, Wohlschläger AM, Drzezga A, Sorg C: „Disrupted intrinsic networks link Amyloid-beta Pathology and Impaired Cognition in Prodromal Alzheimer´s Disease“, Cereb Cortex. 2015;25(12):4678-88, IF = 6.559

4. Ho M, **Manoliu A**, Kuhn FP, Klarhöfer M, Nanz D, Ettlin DA, Boss A, Andreisek G : "Evaluation of reproducibility of diffusion tensor imaging in the brachial plexus at 3.0 Tesla", Invest Radiol. 2017;52(8):482-487, IF = 5.195

5. **Manoliu A**, Nanz D, Ho M, Dappa E, Boss A, Andreisek G, Kuhn FP: „MR neurographic orthopantomogram: Ultra-short echo-time (UTE) imaging of the mandibular bone and teeth complemented with high-resolution morphological and functional MR neurography“, J Magn Reson Imaging. 2016;44(2):393-400, IF = 3.083

6. **Manoliu A**, Ho M, Piccirelli M, Nanz D, Filli L, Dappa E, Liu E, Ettlin DA, Boss A, Andreisek G, Kuhn FP : "Simultaneous multislice-readout segmented echo planar imaging for accelerated diffusion tensor imaging of the mandibular nerve : A feasibility study", J Magn Reson Imaging. 2017;46(3):663-677, IF = 3.083

BJPsych | The British Journal of Psychiatry (2017)
210, 75–82. doi: 10.1192/bjp.bp.114.151928

Changes in extra-striatal functional connectivity in patients with schizophrenia in a psychotic episode

Henning Peters, Valentin Riedl, Andrei Manoliu, Martin Scherr, Dirk Schwerthöffer, Claus Zimmer, Hans Förstl, Josef Bäuml, Christian Sorg* and Kathrin Koch*

Background
In patients with schizophrenia in a psychotic episode, intra-striatal intrinsic connectivity is increased in the putamen but not ventral striatum. Furthermore, multimodal changes have been observed in the anterior insula that interact extensively with the putamen.

Aims
We hypothesised that during psychosis, putamen extra-striatal functional connectivity is altered with both the anterior insula and areas normally connected with the ventral striatum (i.e. altered functional connectivity distinctiveness of putamen and ventral striatum).

Method
We acquired resting-state functional magnetic resonance images from 21 patients with schizophrenia in a psychotic episode and 42 controls.

Results
Patients had decreased functional connectivity: the putamen with right anterior insula and dorsal prefrontal cortex, the ventral striatum with left anterior insula. Decreased functional connectivity between putamen and right anterior insula was specifically associated with patients' hallucinations. Functional connectivity distinctiveness was impaired only for the putamen.

Conclusions
Results indicate aberrant extra-striatal connectivity during psychosis and a relationship between reduced putamen–right anterior insula connectivity and hallucinations. Data suggest that altered intrinsic connectivity links striatal and insular pathophysiology in psychosis.

Declaration of interest
None.

The pathophysiology of the striatum is one of the key elements in our understanding of schizophrenia, particularly of psychotic states.[1,2] Increased striatal dopamine has been suggested as a 'final common pathway to psychosis'.[2] This idea is supported by findings of increased striatal dopamine transmission during prodromal and psychotic states.[3,4] Levels of hyperdopaminergia correlate with psychosis severity and antidopaminergic drugs reduce psychotic symptoms in most cases.[2,5] Recent in-vivo positron emission tomography studies indicate that particularly the presynaptic dopamine concentration is increased, mainly in the dorsal striatum.[4] This regional specificity is further supported by resting-state functional magnetic resonance imaging (rs-fMRI) results, demonstrating that functional connectivity of ongoing activity within the striatum is selectively increased in the putamen. Such intra-striatal functional connectivity changes have been shown to be only present during psychosis and associated with the severity of positive symptoms, whereas functional connectivity changes within the ventral striatum were only found during psychotic remission and linked with negative symptoms.[6] Because of striatum's involvement in cortico-basal-ganglia-thalamo-cortical loops, the question arises whether, beyond specifically aberrant intra-striatal connectivity, extra-striatal functional connectivity with cortical regions is also specifically changed, in particular for the putamen.

First, patterns of cortical extra-striatal functional connectivity are distinct for dorsal and ventral striatum.[7] While ventral striatum functional connectivity includes the ventromedial prefrontal cortex and orbitofrontal cortex, the putamen is mainly linked with the anterior insula, anterior cingulate cortex and medial/lateral prefrontal cortex.[7,8] Previous imaging studies demonstrated changes in extra-striatal connectivity in patients with schizophrenia.[6] For example, during cognitive tasks such as attentional oddball, decreased frontostriatal functional connectivity was found in patients, with progressive decreases being associated with disorder severity and task duration.[9] Resting-state studies of ongoing brain activity revealed aberrant functional connectivity from various frontal regions including the anterior cingulate cortex, dorsolateral prefrontal cortex and orbitofrontal cortex with the striatum in prodromal state and patients with psychosis.[10–13] Most recently, altered striatal functional connectivity with cortical regions has been observed from increased to decreased connectivity along a ventral–dorsal axis within the striatum in patients with first-episode psychosis and their relatives; this result indicates complex and disease risk-related reorganisation of extra-striatal functional connectivity across striatal subregions in schizophrenia.[14] Particularly across different striatal subsystems, this complex pattern suggests less distinctiveness of functional connectivity for different subregions especially in psychosis. More specifically, accounting for putamen's prominent role in psychosis and its intra-striatal reorganisation, we hypothesised that – relative to the ventral striatum – putamen functional connectivity with the cortex might be increased for regions that are normally more strongly connected with the ventral striatum.

Second, from the perspective of intrinsic networks (i.e. consistent spatial patterns of coherent ongoing brain activity), the putamen is intimately associated with the salience network.[8] The salience network covers insula, anterior cingulate cortex and parts of the dorsomedial and dorsolateral prefrontal cortex. It

*These authors contributed equally to this work.

processes emotionally salient stimuli from the body and external world and controls, particularly via its right anterior insula, interactions between other networks such as default mode or central executive network.[15] Recently, aberrant salience network connectivity and control function was observed in patients in a psychotic episode and associated with hallucinations with aberrations converging on the right anterior insula.[16,17] These findings were specific for psychosis, since during psychotic remission left rather than right anterior insula connectivity was relevant for aberrant network interactions and patients' negative symptoms.[16] Together with intra-striatal changes, these data suggest that selective changes of the putamen and right anterior insula in psychosis might be related. Based on these findings, we hypothesised that putamen's extra-striatal functional connectivity with the right anterior insula is specifically altered in patients in a psychotic episode and less distinct relative to the ventral striatum.

To test these hypotheses, we measured blood oxygenation level-dependent (BOLD) activity in 42 healthy controls and 21 patients with schizophrenia in a psychotic episode by use of rs-fMRI. Imaging data of half of the healthy volunteers were used as independent regional priors for subsequent group comparisons between patients and the other half of the controls, to increase specificity of findings. Main outcome measures were individual β-maps of seed-based functional connectivity applied to putamen and ventral striatum. To estimate group differences, β-maps were compared across groups via voxelwise two-sample *t*-tests. To investigate the relationship between psychotic symptoms and aberrant extra-striatal functional connectivity in patients, correlation analysis was performed. To analyse distinctiveness of extra-striatal functional connectivity for putamen and ventral striatum, we defined distinct functional connectivity by averaged incongruent seed-target-functional connectivity values (i.e. averaged functional connectivity values of functional connectivity seed in the putamen and functional connectivity target as defined by the functional connectivity map of the ventral striatum and *vice versa*[18]).

Method

Participants

In total, 42 healthy controls (control group) and 21 patients with schizophrenia in a psychotic episode (schizophrenia group) participated in the study. All patients and 21 healthy controls had been investigated in a previous study mentioned above,[6] which investigated intra-striatal functional connectivity changes. For the current study of extra-striatal functional connectivity, an additional 21 group-matched healthy controls were recruited as an independent control group to improve extra-striatal functional connectivity analysis sensitivity and specificity. Written informed consent in accordance with the Human Research Committee guidelines of the Klinikum Rechts der Isar, Technische Universität München was obtained from all participants. Patients were recruited from the Department of Psychiatry, Klinikum Rechts der Isar TU München and controls by word-of-mouth advertising. Participants' examination included medical history, psychiatric interview, psychometric assessment, urine drug screening and additionally blood tests for the schizophrenia group. The global level of social, occupational, and psychological functioning was measured with the Global Assessment of Functioning Scale (GAF).[19] Psychiatric diagnoses relied on the DSM-IV.[20] To assess psychiatric diagnoses, the Structured Clinical Interview for DSM-IV (SCID-I) was used.[19] For rating severity of clinical symptoms on the day of scanning, the Positive and Negative Syndrome Scale (PANSS) was applied.[21] Clinical psychometric assessment was completed by psychiatrists (D.S. and M.S.) who have been professionally trained for SCID and PANSS-based interviews with interrater reliability of more than 95%.

Inclusion criteria for the study were diagnosis of schizophrenia, acute psychosis, particularly during the fMRI session (at least three positive PANSS subscores $\geqslant 3$), and age between 18 and 60 years. Exclusion criteria were current or past neurological or internal systemic disorder, current depressive or manic episode, substance misuse (except for nicotine) and cerebral pathology on MRI.

All the schizophrenia group were diagnosed with paranoid schizophrenia during acute psychosis as indicated by clinical exacerbation and increased positive symptom scores on the PANSS (Table 1). In total, 7 out of 21 had significant hallucinations (PANSS P3 $\geqslant 3$), 15 delusions (PANSS P1 $\geqslant 3$). The mean duration of illness was 7.15 years (s.d. = 6.89), the mean number of hospital admissions was 2.98 (s.d. = 2.48). Concerning medication, three patients were free of any antipsychotic medication. All other patients received mono- or dual therapy with atypical antipsychotic medication (see Table 1 and online Table DS1). All patients have been treated previously with antipsychotic drugs (i.e. none of the patients was treatment naive). The control group were all free of any current or past psychiatric, neurological or systemic disorder or psychotropic medication.

Behavioural and imaging data from the schizophrenia group and 21 controls (the 'comparison control group') were used in a previous study,[6] which focused on intra-striatal functional connectivity. An additional 21 group-matched healthy controls were recruited as an independent control group to improve functional connectivity analysis sensitivity and specificity (see below).

MRI data acquisition

MRI was carried out using a 3T whole-body MR scanner (Achieva, Philips, The Netherlands) using an eight-channel phased-array head coil. T_1-weighted anatomical data were obtained by a magnetisation-prepared rapid acquisition gradient echo sequence (echo time (TE) = 4 ms, repetition time (TR) = 9 ms, inversion time (TI) = 100 ms, flip angle 5°, field of view (FoV) = 240 × 240 mm, matrix 240 × 240, 170 slices, voxel size 1 × 1 × 1 mm). Data from rs-fMRI were obtained by a gradient-echo echo-planar imaging (EPI) sequence (TE = 35 ms, TR = 2000 ms, flip angle 82°, FoV = 220 × 220 mm, matrix 80 × 80, 32 slices, slice thickness 4 mm, and 0 mm interslice gap). All participants underwent 10 min of rs-fMRI resulting in 300 volumes. As in most previous rs-fMRI studies (e.g. Di Martino *et al*,[7] Seeley *et al*[8]), we instructed participants to keep their eyes closed and not to fall asleep. We verified that participants stayed awake by interrogating via intercom immediately after the rs-fMRI scan.

MRI data analysis

Preprocessing

For each participant, the first three rs-fMRI scans were discarded because of magnetisation effects. SPM8 (Wellcome Department of Cognitive Neurology, London) was used for motion correction, spatial normalisation into the stereotactic space of the Montreal Neurological Institute (MNI) and spatial smoothing with an 8 × 8 × 8 mm Gaussian kernel. To ensure data quality, particularly concerning motion-induced artefacts, temporal signal-to-noise ratio (tSNR) and point-to-point head motion were estimated for each participant.[22,23] Point-to-point motion was defined as the absolute displacement of each brain volume compared with its previous volume. Moreover, root mean square (RMS) of the translational head movement parameters was calculated for each

Table 1 Demographic and clinical characteristics

Measure	Independent control group ($n=21$)	Comparison control group ($n=21$)	Schizophrenia group ($n=21$)	Schizophrenia group ($n=21$) *v.* comparison control group ($n=21$)[a]	
Age, mean (s.d.)	33.49 (12.9)	33.57 (13.6)	34.05 (12.27)	−0.121	0.904
Gender (men/women), *n*	10/11	10/11	10/11		
Positive and Negative Syndrome Scale, mean (s.d.)					
Total	–	30.14 (0.65)	80.76 (20.77)	8.96	<0.001*
Positive	–	7.05 (0.22)	19.4 (6.09)	9.091	<0.001*
Negative	–	7.10 (0.44)	21.14 (8.20)	7.84	<0.001*
General	–	16.05 (0.22)	39.81 (11.06)	9.846	<0.001*
Global Assessment of Functioning Scale, mean (s.d.)	–	99.76 (1.09)	39.62 (11.68)	−23.492	<0.001*
Chlorpromazine-equivalent dose, mean (s.d.)	–		388.61 (384.67)		

a. Two-sample *t*-test
*Significant at $P<0.05$ corrected for multiple comparisons.

participant.[23] Excessive head motion (cumulative motion translation >3 mm and mean point-to-point translation or rotation >0.15 mm or 0.1) was applied as exclusion criterion. None of the participants had to be excluded. Two-sample *t*-tests yielded no significant differences between groups regarding mean point-to-point translation or rotation of any direction ($P>0.15$), RMS ($P>0.2$), or tSNR ($P>0.40$). Further control for head motion effects was carried out in the individual-level functional connectivity analysis.

Individual-level functional connectivity analysis

Seeds of functional connectivity analysis were selected according to coordinates of group-different regions derived from our first study in patients during acute psychosis (putamen) and after remission (ventral striatum) relative to healthy controls.[6] We created spherical regions of interest (ROIs, 6 mm radius) for the dorsal striatum, i.e. left and right putamen (+/–24, 12, 0) and the ventral striatum, i.e. nucleus accumbens (+/–12, 9, –9), respectively, by the use of MarsBaR (v0.42, http://marsbar.sourceforge.net/). Centres of ROIs were derived from the study of Martinez and colleagues and corresponded to centres in our previous study.[6,24]

After Butterworth bandpass-filtering of all voxel time courses for the frequency range from 0.009 to 0.08 Hz, we extracted voxel time courses of seed ROIs and reduced them to ROI-representative time courses by singular value decomposition. Each time course was entered into a first-level fixed-effects general linear model in SPM8, and four separate functional connectivity analyses (i.e. left/right ventral striatum, left/right putamen) were performed for each participant yielding four functional connectivity maps for subsequent second-level analyses. Regressors for global grey matter, white matter, cerebrospinal fluid (CSF) BOLD-signal, and six movement parameters for each participant were included as covariates of no interest in each model.[7] As the global grey matter signal is thought to reflect a combination of physiological processes (such as cardiac and respiratory fluctuations) and scanner drift, it was included as a nuisance signal to minimise the influence of such factors.[25] To extract the nuisance covariate time series for grey matter, white matter and CSF, each individual's high-resolution T_1-weighted structural image was segmented. Mean images of study sample's T_1-segmentation were used to create ROIs for the extraction of grey matter, white matter and CSF nuisance signals.

Group-level functional connectivity analysis

Group analyses were performed using β-maps from individual-level functional connectivity analysis in separate flexible factorial models of analysis of variance (ANOVA). More specifically, all ANOVA models included covariates of no interest (gender, age, seed regional volumes of ventral striatum and putamen, respectively; see voxel-based morphometry (VBM) analysis below) and were restricted to explicit masks of ventral striatum and putamen functional connectivity, respectively. Masks were created by use of a flexible factorial ANOVA model of putamen/ventral striatum functional connectivity images of the independent control group (factors: hemisphere with levels left/right and seed-ROI with levels ventral striatum/putamen); appropriate *post-hoc* *t*-tests revealed positively correlated functional connectivity maps for the ventral striatum and putamen, respectively ($P<0.05$ uncorrected for masks; $P<0.05$ family-wise error (FWE)-corrected on voxel level for online Fig. DS1). Then, to analyse group differences of putamen functional connectivity, a flexible factorial ANOVA ($P<0.05$ FWE-corrected on voxel level and restricted to a mask of the independent control group) was applied to putamen functional connectivity images of currently symptomatic patients and the comparison control group with factors group (levels: patient/control) and seed-ROI (levels: left/right putamen). Analogous ANOVA was applied for ventral striatum functional connectivity. For both ANOVA models, the main effect of group (and corresponding *post-hoc* *t*-tests to reveal direction of change) was the effect of interest. Reported voxel coordinates correspond to standardised MNI space. To visualise results, we used MRIcroN (http://www.nitrc.org/projects/mricron).

Brain–behaviour relationship

To investigate the relationship between striatal functional connectivity differences and psychotic symptoms, β-values of regional group differences in putamen and ventral striatum functional connectivity for each cluster and patient were averaged across voxels and entered into partial correlation analyses. According to previous results, we chose subscores instead of the summed positive symptom score. Since only hallucinations and delusions correlated with striatal functional connectivity decreases, we limited analyses to these subscores.[6] Covariates of no interest were age and gender as well as medication levels reflected by chlorpromazine-equivalent units (CPZ).[26] The significance threshold was set to $P<0.007$, Bonferroni-corrected for seven group-different clusters of functional connectivity decreases (the seven clusters are listed in Table 2).

Distinct functional connectivity

We expected that in the schizophrenia group, putamen's functional connectivity is changed both with the anterior insula and with areas that are typically connected more strongly with the ventral striatum. To examine such altered distinctiveness of putamen and ventral striatum connectivity, we defined distinct

Table 2 Decreased functional connectivity in the schizophrenia group: schizophrenia group < control group

Seed	Anatomical regions	Side	Cluster size in voxels, *k*	MNI, peak voxel coordinates, *x*, *y*, *z*	*z*-score	*P*[a]
Putamen	Inferior frontal gyrus (opercular, orbital) Anterior insula	Right	236	45, 15, −6	5.21	<0.0001
	Superior frontal gyrus	Right	87	51, 36, 6	4.57	0.027
	Inferior frontal gyrus (triangular) Middle frontal gyrus	Right	61	12, 12, 48	5.50	<0.0001
	Middle frontal gyrus	Right	48	36, 48, 30	4.16	0.044
	Middle frontal gyrus	Left	36	−36, 48, 27	4.27	0.029
	Middle cingulate cortex	Right	20	9, 15, 39	4.33	0.023
Ventral striatum	Anterior insula Inferior frontal gyrus (orbital)	Left	26	−36, 21, −9	4.37	0.011

MNI, Montreal Neurological Institute.
a. Two-sample *t*-test, *P*<0.05 familywise error -corrected for multiple comparisons on voxel level.

functional connectivity in terms of averaged incongruent seed-target functional connectivity values of striatal seeds. For example, the connectivity of the putamen with regions that were normally coupled more strongly with the ventral striatum than the putamen is referred to as incongruent seed-target connectivity of the putamen. By the use of appropriate *post-hoc* *t*-tests for the above-mentioned ANOVA model (factors seed (putamen/ventral striatum) and side (left/right) of the independent control group) ($P<0.05$ FWE-corrected), we first obtained distinct functional connectivity maps of the putamen (main effect seed putamen > ventral striatum) and ventral striatum (main-effect seed ventral striatum > putamen).[18] We used these distinct functional connectivity maps as masks to calculate averaged incongruent seed-target functional connectivity values (for example, for a given participant and the putamen as seed, β-values of putamen functional connectivity map were averaged across all voxels of the ventral striatum-distinct functional connectivity mask). Incongruent seed-target-functional connectivity values reflect distinctiveness of striatal functional connectivity and were compared across the schizophrenia and comparison control group by use of two-sample *t*-tests ($P<0.05$). Accordingly, increased incongruent seed-target connectivity for a striatal seed would be interpreted as reduced distinctiveness of striatal functional connectivity because of an enlarged functional connectivity for this seed.

Voxel-based morphometry

To control for effects of striatal structure on functional connectivity results, we included ventral striatum and putamen volumes as covariates of no interest into statistical models of group comparisons. We used previous results of VBM analysis in the schizophrenia group and the comparison control group as described in the online supplement DS1 and elsewhere.[6] Briefly, VBM volumes of patients' left and right putamen and ventral striatum were not different from those of the comparison control group.

Results

In the independent control group, significant functional connectivity was found for the putamen with bilateral inferior, middle, and superior frontal gyrus, anterior insula, anterior and middle cingulate cortex, pallidum and caudate nucleus, for the ventral striatum with orbital parts of the inferior frontal gyrus, the medial superior frontal gyrus, anterior insula, anterior cingulate cortex and pallidum ($P<0.05$ FWE-corrected, online Fig. DS1, Table DS2). Putamen and ventral striatum functional connectivity maps of the schizophrenia group and the comparison control group were largely consistent with these patterns, indicating that the basic pattern of putamen and ventral striatum functional connectivity is preserved in patients (online Fig. DS1).

Group comparisons, which were masked by functional connectivity patterns of the independent control group, revealed that in the schizophrenia group putamen functional connectivity was decreased for bilateral middle frontal gyrus and superior frontal gyrus, the right opercular and triangular part of the inferior frontal gyrus, right anterior insula and right middle cingulate cortex ($P<0.05$ FWE-corrected, online Fig. DS2, Table 2). The schizophrenia group's ventral striatum functional connectivity was decreased with the left anterior insula, extending to the orbital part of the left inferior frontal gyrus ($P<0.05$ FWE-corrected, online Fig. DS2, Table 2).

The partial correlation analyses for the patients' decreased regional functional connectivity values and psychotic symptoms ($P<0.007$, Bonferroni-corrected for multiple testing because of seven group-different clusters) showed the decreased functional connectivity between putamen and right anterior insula to be negatively correlated with hallucinations ($P<0.001$, Fig. 1). Neither delusions nor other regions' group-different functional connectivity showed significant results.

To investigate distinctiveness of striatal functional connectivity for putamen and ventral striatum, averaged incongruent seed-target functional connectivity was calculated for putamen and ventral striatum for each participant. In the schizophrenia group only, the putamen showed significantly increased incongruent seed-target functional connectivity values relative to ventral striatum and different to those of the control group (one- and two-sample *t*-test, $P<0.05$, Fig. 2).

Discussion

Main findings

Extra-striatal cortical functional connectivity of the putamen and ventral striatum was studied in patients with schizophrenia during psychosis and in healthy controls using rs-fMRI and seed-based functional connectivity analysis. In patients, putamen's functional connectivity was reduced with the right anterior insula and the dorsomedial and dorsolateral prefrontal cortex, whereas ventral striatum's functional connectivity was decreased with the left anterior insula. Only putamen's aberrant functional connectivity with the right anterior insula was significantly associated with patients' hallucinations. Putamen's functional connectivity in patients was increased with areas regularly connected with the ventral striatum, indicating specifically less distinctive functional connectivity of the putamen relative to the ventral striatum. Data provide evidence that aberrant extra-striatal cortical functional connectivity during psychosis is centred on the putamen, with

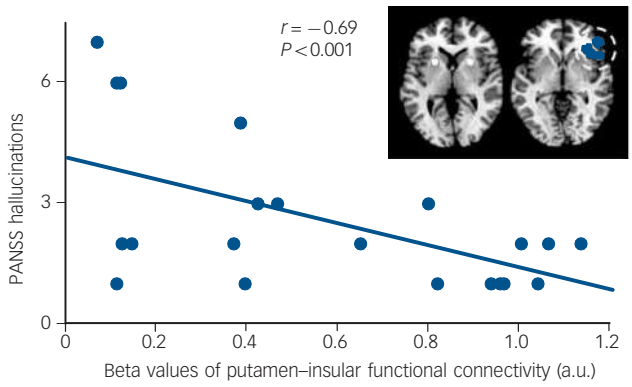

Fig. 1 Negative correlation between hallucinations and functional connectivity between putamen and right anterior insula.

Partial correlation analyses on averaged beta values of functional connectivity group-different clusters in online Fig. DS2 with hallucinations and delusion score on the Positive and Negative Syndrome Scale (PANSS) revealed only for the functional connectivity between putamen and right anterior insula a significant relationship with hallucinations (partial correlation coefficient $r = -0{,}69$, $P < 0.001$, Bonferroni-corrected for multiple testing (i.e. number of group-different clusters). To control for confounding effects, medication levels (chlorpromazine-equivalent dose units), age and gender were included in partial correlation models. a.u., arbitrary units.

both less distinct connectivity focused on the putamen and decreased connectivity between putamen and right anterior insula specifically related to psychotic symptoms. Particularly the last finding suggests aberrant functional connectivity to link striatal and insular pathophysiology in psychosis.

Comparison with findings from other studies

In the schizophrenia group, we found reduced functional connectivity for both putamen and ventral striatum with cortical regions (online Fig. DS2, Table 2). Putamen functional connectivity was reduced in right anterior insula and dorsomedial and dorsolateral prefrontal cortex, whereas ventral striatum functional connectivity was decreased with the left anterior insula. Group differences were independent of age, gender and striatal volume effects, for which we controlled statistically. Spatial putamen and ventral striatum functional connectivity maps of those in the schizophrenia group were largely comparable with those of the control group, indicating that basic extra-striatal functional connectivity is preserved in schizophrenia (online Fig. DS1). Reduced functional connectivity between putamen and dorsal prefrontal cortex is in line with previous findings.[11–14] For example, Zhou and colleagues[11,12] found reduced middle frontal gyrus functional connectivity with the dorsal striatum and Fornito and colleagues[14] recently observed reduced functional connectivity between the dorsocaudal putamen and dorsal prefrontal cortex in patients with first-episode psychosis, with striatal seed coordinates very near to those of our study. Furthermore, for the same prefrontal cortex areas, authors reported that putamen functional connectivity was also reduced in unaffected first-degree relatives of patients with schizophrenia, suggesting that these connectivity changes may express a specific disease risk more associated with disease trait than state-dependent symptoms. Our finding that reduced functional connectivity between putamen and dorsal prefrontal cortex is not related to psychotic symptoms, supports this suggestion.

On the other hand, we found reduced functional connectivity with right and left anterior insula in patients for both putamen and ventral striatum (online Fig. DS2). This finding is in line with previous findings of reduced striatoinsular functional connectivity in patients in prodromal psychotic states and psychosis.[14,27] More specifically, Orliac and colleagues recently reported reduced striatal functional connectivity within the salience network centred on anterior insula in patients with schizophrenia.[28] It should be noted, however, that in the study by Orliac *et al*, the salience network included the bilateral anterior insula whereas we identified reduced connectivity between the putamen and the right anterior insula in association with reduced connectivity between the ventral striatum and the left anterior insula. The salience network and especially the anterior insula is crucially involved in processing salient internal/external stimuli and controlling interactions between two distinct core cognitive networks, namely the default mode network – involved in self-referential cognition – and the central executive network – involved in goal-driven tasks.[8] In patients with schizophrenia, the anterior insula is characterised by various structural and functional alterations such as atrophy, impaired white matter structure and aberrant functional connectivity. In particular aberrant functional connectivity of the anterior insula within the salience network is associated with aberrant default-mode network/central executive network interactions and the severity of patients' symptoms.[16,29] Our finding of reduced functional connectivity between striatum and anterior insula indicates that a disrupted connectivity between striatum and central components of the salience network may constitute a core mechanism underlying the pathophysiology of schizophrenia.

Concerning laterality of aberrant striatal functional connectivity, patients' functional connectivity was reduced for the putamen with the right anterior insula and for the ventral striatum with left anterior insula. Previously we found that only right anterior insula functional connectivity within the salience network was associated with positive symptoms during psychosis,[17] whereas during remission, left anterior insula connectivity was specifically linked with negative symptoms.[29] Correspondingly, for the striatum we found that during psychosis, only putamen intra-striatal functional connectivity was increased and linked with positive symptoms, whereas during remission, only ventral striatum functional connectivity was increased and linked with negative symptoms.[6] Together, it seems that putamen and right anterior insula connectivity is related more with psychosis and positive symptoms, whereas ventral striatum and left anterior insula is related more with remission and negative symptoms. Since the control of vegetative nervous system activity is asymmetrically represented in the anterior insula with sympathetic parts more related to the right anterior insula whereas parasympathetic parts relate more with the left anterior insula,[30] one might speculate whether lateralised striatal functional connectivity changes in putamen and ventral striatum in psychosis reflect this rather basic asymmetry. Future studies are necessary to investigate such a potential link.

Psychosis and putamen functional connectivity

With respect to psychosis, two additional findings specify decreased extra-striatal functional connectivity in schizophrenia: (a) aberrant functional connectivity seems to be centred on the putamen relative to the ventral striatum and (b) putamen's decreased functional connectivity with right anterior insula is specifically relevant for psychotic symptoms.

Abnormal distinctiveness of dorsal striatum functional connectivity

We found less distinct functional connectivity of the striatum in the form of increased putamen functional connectivity with regions regularly connected with the ventral striatum (Fig. 2). This finding suggests that in patients, areas which are preferentially linked with the ventral striatum, show on average increased functional connectivity with the putamen. This finding is focused on the putamen, as distinct functional connectivity of the ventral striatum relative to the putamen was normal in patients (Fig. 2).

This spatial focus on the dorsal striatum in psychosis corresponds well with previous findings concerning other aspects of striatal pathophysiology. For example, intra-striatal functional connectivity is selectively increased in the putamen during psychosis, and presynaptic dopamine activity is increased during prodromal and psychotic states, especially in the dorsal striatum.[1,3,4,6] Since such relative dominance of the dorsal striatum is characteristic for habit-like behaviour, some theoretical accounts suggested that patients' pronounced changes in the dorsal striatum might point at a habit-like nature of psychotic symptoms.[31,32]

Aberrant putamen functional connectivity and severity of hallucinations

In line with this relative dominance of dorsal striatum changes in psychosis, we found explicit evidence that only patients' decreased putamen functional connectivity with the right anterior insula is significantly linked with the degree of hallucinations (Fig. 1). Fornito and colleagues[14] argue that the previously reported relationship between reduced dorsal striatum functional connectivity and symptom severity may constitute a state-independent risk marker. However, they mainly discussed functional connectivity with dorsolateral and medial prefrontal cortex and did not consider PANSS subscores. Our finding fit with previous results very well: first, aberrant right anterior insula functional connectivity within the salience network is specifically associated with psychosis, particularly with hallucinations; second, putamen's intra-striatal functional connectivity is selectively associated with psychosis and the degree of psychotic symptoms.[6] The current result provides a link between these previous findings by extending isolated findings centred on either anterior insula or the dorsal striatum and showing that disrupted functional connectivity between putamen and right anterior insula is specifically related to psychotic key symptoms.

Link between proximal salience, motivational salience and dopamine

More generally, these data suggest a link between two relevant models of psychosis in schizophrenia, namely the proximal salience model of Palaniyappan[17,33] and the motivational salience model of Kapur.[34,35] Although these two concepts integrate a lot of data that are critical for explaining psychotic symptoms in schizophrenia, they emphasise distinct neurocognitive mechanisms centred on distinct key regions, namely the anterior insula and the striatum. More specifically, the concept of proximal salience describes a momentary interoceptive state resulting from the appraisal of external and internal stimuli, which modulates both succeeding learning processes and the selection of actions/cognitions to improve future evaluation.[17] In contrast, the concept of motivational salience describes the assignment of a specific motivational value to an internal or external stimulus following its appraisal based on reward prediction error processes.[34,35] In a neurobiological context, proximal salience has been proposed to be mediated by the anterior insula within the salience network, particularly via modulation of the interaction between other intrinsic connectivity networks, such as the default mode network and central executive network, whereas motivational salience depends highly on striatal activity, which, in turn, is strongly controlled by striatal dopaminergic activity.[31,36] Latest studies provide strong evidence that psychosis in schizophrenia is characterised by altered functional connectivity within the dorsal striatum as well as in the right anterior insula within the salience network and by aberrant functional connectivity between intrinsic brain networks.[16,37] However, a direct link between these findings is still missing. Recently, Cole and colleagues[38] demonstrated that striatoinsular functional connectivity is influenced by pharmacological modulation of striatal dopamine levels. Moreover, Lui *et al*[39] reported increased functional connectivity between the dorsal striatum and the bilateral prefrontal cortex, the parietal cortex and the left superior temporal cortex after short-term treatment with second-generation antipsychotic medication in patients with first-episode schizophrenia. Of note, the increase in functional connectivity was associated with a reduction of clinical symptoms implicating that a pharmacologically induced alteration in functional connectivity leads to significant clinical improvement.

Future studies are required that focus explicitly on the linking potential of striatoinsular intrinsic connectivity between

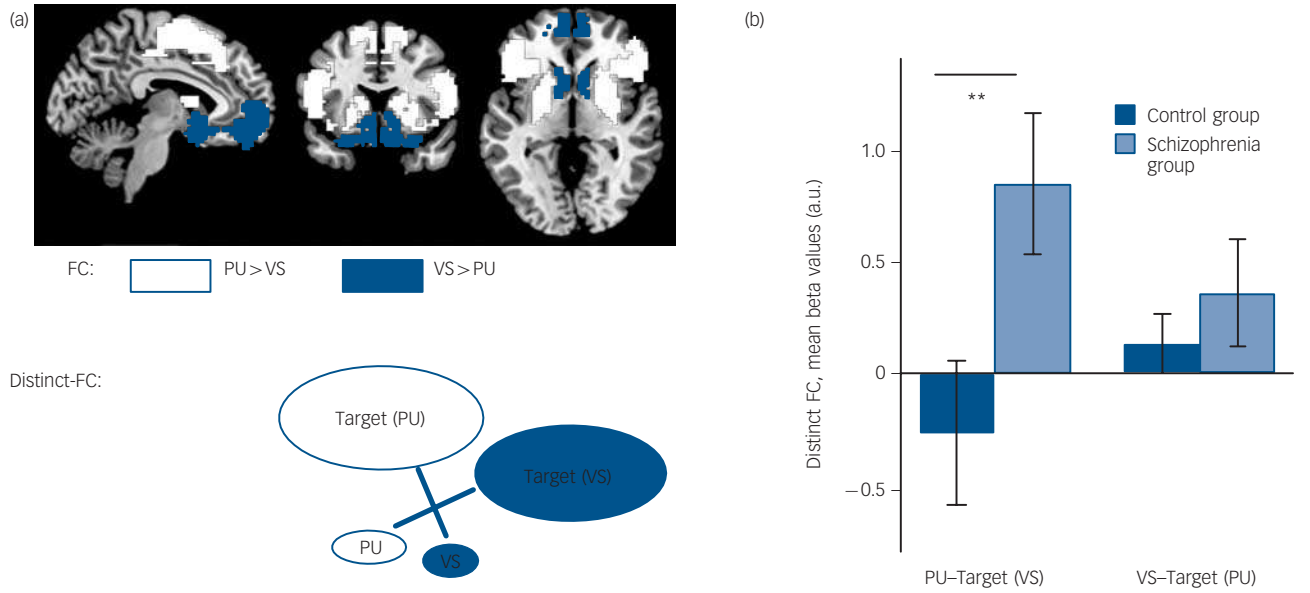

Fig. 2 Distinctiveness of functional connectivity (FC) of putamen (PU) and ventral striatum (VS).

(a) White and blue maps represent binary spatial connectivity maps of the independent control group based on *post-hoc t*-tests (putamen < ventral striatum, putamen > ventral striatum) of ANOVA with factors seed (putamen, ventral striatum) and seed side (left, right), $P_{FWE}<0.05$ corrected for family-wise error (FWE)). The idea of distinct functional connectivity is based on averaged incongruent seed-target functional connectivity for example averaged functional connectivity of the putamen in white with the regular target of the ventral striatum in blue. (b) Mean beta values for distinct functional connectivity for the schizophrenia and the control group are presented. **Indicates significant group differences in distinct functional connectivity (two-sample *t*-tests $P<0.05$). a.u., arbitrary units.

dopaminergic reward prediction error activity in the dorsal striatum, right anterior insula control function on interacting intrinsic networks and psychotic symptoms.

Methodological issues and limitations

The fact that almost all of the schizophrenia group in our study were medicated may limit the explanatory power of our findings. An influence of antipsychotic medication on functional brain connectivity has been shown.[39,40] However, a previous comparison between patient subsamples receiving antipsychotics and those who were medication-free did not yield a significant difference in striatal functional connectivity.[14] To control for the potential confound of medication, we included – with respect to the analysis of the relationship between aberrant functional connectivity and psychotic symptoms – CPZ units in the statistical model of patients' functional connectivity, which did not yield a significant explanatory effect of functional connectivity in the present study.[6,16] Nevertheless, antipsychotic medication has to be considered when evaluating the current study's results. Future studies in patients who are drug-free might be helpful; however studies in patients who are drug-free but in a psychotic episode might have strong practical and ethical problems.

In conclusion, our results provide evidence that in patients with schizophrenia in a psychotic episode, striatal functional connectivity with the frontoinsular cortex is decreased. Changes were pronounced for the putamen relative to the ventral striatum and decreased connectivity between putamen and right anterior insula was specifically related to psychotic symptoms. Data suggest a link between striatal and anterior insular pathophysiology of psychosis via functional connectivity.

Henning Peters, MD, PhD, Department of Psychiatry and TUM-Neuroimaging Center Klinikum rechts der Isar, Technische Universität München, Munich, Germany; **Valentin Riedl**, MD, PhD, Department of Psychiatry, Department of Neuroradiology, Department of Nuclear Medicine and TUM-Neuroimaging Center Klinikum rechts der Isar, Technische Universität München, Munich, Germany; **Andrei Manoliu**, MD, Department of Neuroradiology and TUM-Neuroimaging Center Klinikum rechts der Isar, Technische Universität München, Munich, Germany and Department of Radiology, University Hospital Zürich, Rämistrasse 100, 8091 Zürich, Switzerland; **Martin Scherr**, MD, **Dirk Schwerthöffer**, MD, Department of Psychiatry, Technische Universität München, Munich, Germany; **Claus Zimmer**, MD, Department of Neuroradiology, Technische Universität München, Munich, Germany; **Hans Förstl**, MD, **Josef Bäuml**, MD, Department of Psychiatry, Technische Universität München, Munich, Germany; **Christian Sorg**, MD, Department of Psychiatry, Department of Neuroradiology, Department of Nuclear Medicine and TUM-Neuroimaging Center Klinikum rechts der Isar, Technische Universität München, Munich, Germany; **Kathrin Koch**, PhD, Department of Neuroradiology and TUM-Neuroimaging Center Klinikum rechts der Isar, Technische Universität München, Munich, Germany

Correspondence: Kathrin Koch, Department of Neuroradiology and TUM-Neuroimaging Center Klinikum rechts der Isar, Technische Universität München, Ismaninger strasse 22, 81675 Munich, Germany. Email: kathrin.koch@tum.de

First received 26 May 2014, final revision 15 Dec 2014, accepted 27 May 2015

Funding

This work was supported by the German Federal Ministry of Education and Research (BMBF 01ER0803 to C.S.), the Alzheimer Forschung Initiative (AFI 08860 to V.R.) and the Kommission für Klinische Forschung of the Klinikum Rechts der Isar der Technischen Universität München (KKF 8765162 to C.S). We are grateful to the participants of the study and the staff of the Department of Psychiatry and Neuroradiology for their help in recruitment and data collection.

References

1 Howes OD, Egerton A, Allan V, McGuire P, Stokes P, Kapur S. Mechanisms underlying psychosis and antipsychotic treatment response in schizophrenia: insights from PET and SPECT imaging. *Curr Pharm Des* 2009; **15**: 2550–9.

2 Howes OD, Kapur S. The dopamine hypothesis of schizophrenia: version III – the final common pathway. *Schizophr Bull* 2009; **35**: 549–62.

3 Howes OD, Montgomery AJ, Asselin MC, Murray RM, Valli I, Tabraham P, et al. Elevated striatal dopamine function linked to prodromal signs of schizophrenia. *Arch Gen Psychiatry* 2009; **66**: 13–20.

4 Kegeles LS, Abi-Dargham A, Frankle WG, Gil R, Cooper TB, Slifstein M, et al. Increased synaptic dopamine function in associative regions of the striatum in schizophrenia. *Arch Gen Psychiatry* 2010; **67**: 231–9.

5 Agid O, Mamo D, Ginovart N, Vitcu I, Wilson AA, Zipursky RB, et al. Striatal vs extrastriatal dopamine D2 receptors in antipsychotic response – a double-blind PET study in schizophrenia. *Neuropsychopharmacology* 2007; **32**: 1209–15.

6 Sorg C, Manoliu A, Neufang S, Myers N, Peters H, Schwerthoffer D, et al. Increased intrinsic brain activity in the striatum reflects symptom dimensions in schizophrenia. *Schizophr Bull* 2013; **39**: 387–95.

7 Di Martino A, Scheres A, Margulies DS, Kelly AM, Uddin LQ, Shehzad Z, et al. Functional connectivity of human striatum: a resting state FMRI study. *Cereb Cortex* 2008; **18**: 2735–47.

8 Seeley WW, Menon V, Schatzberg AF, Keller J, Glover GH, Kenna H, et al. Dissociable intrinsic connectivity networks for salience processing and executive control. *J Neurosci* 2007; **27**: 2349–56.

9 Morey RA, Inan S, Mitchell TV, Perkins DO, Lieberman JA, Belger A. Imaging frontostriatal function in ultra-high-risk, early, and chronic schizophrenia during executive processing. *Arch Gen Psychiatry* 2005; **62**: 254–62.

10 Salvador R, Martinez A, Pomarol-Clotet E, Sarro S, Suckling J, Bullmore E. Frequency based mutual information measures between clusters of brain regions in functional magnetic resonance imaging. *Neuroimage* 2007; **35**: 83–8.

11 Zhou Y, Liang M, Tian L, Wang K, Hao Y, Liu H, et al. Functional disintegration in paranoid schizophrenia using resting-state fMRI. *Schizophr Res* 2007; **97**: 194–205.

12 Zhou Y, Liang M, Jiang T, Tian L, Liu Y, Liu Z, et al. Functional dysconnectivity of the dorsolateral prefrontal cortex in first-episode schizophrenia using resting-state fMRI. *Neurosci Lett* 2007; **417**: 297–302.

13 Tu PC, Lee YC, Chen YS, Li CT, Su TP. Schizophrenia and the brain's control network: aberrant within- and between-network connectivity of the frontoparietal network in schizophrenia. *Schizophr Res* 2013; **147**: 339–47.

14 Fornito A, Harrison BJ, Goodby E, Dean A, Ooi C, Nathan PJ, et al. Functional dysconnectivity of corticostriatal circuitry as a risk phenotype for psychosis. *JAMA Psychiatry* 2013; **70**: 1143–51.

15 Menon V, Uddin LQ. Saliency, switching, attention and control: a network model of insula function. *Brain Struct Funct* 2010; **214**: 655–67.

16 Manoliu A, Riedl V, Zherdin A, Muhlau M, Schwerthoffer D, Scherr M, et al. Aberrant dependence of default mode/central executive network interactions on anterior insular salience network activity in schizophrenia. *Schizophr Bull* 2014; **40**: 428–37.

17 Palaniyappan L, Liddle PF. Does the salience network play a cardinal role in psychosis? An emerging hypothesis of insular dysfunction. *J Psychiatry Neurosci* 2012; **37**: 17–27.

18 Etkin A, Prater KE, Schatzberg AF, Menon V, Greicius MD. Disrupted amygdalar subregion functional connectivity and evidence of a compensatory network in generalized anxiety disorder. *Arch Gen Psychiatry* 2009; **66**: 1361–72.

19 Spitzer RL, Williams JB, Gibbon M, First MB. The Structured Clinical Interview for DSM-III-R (SCID). I: history, rationale, and description. *Arch Gen Psychiatry* 1992; **49**: 624–9.

20 American Psychiatric Association. *Diagnostic and Statistical Manual of Mental Disorder (4th edn) (DSM-IV)*. APA, 1994.

21 Kay SR, Fiszbein A, Opler LA. The positive and negative syndrome scale (PANSS) for schizophrenia. *Schizophr Bull* 1987; **13**: 261–76.

22 Murphy K, Bodurka J, Bandettini PA. How long to scan? The relationship between fMRI temporal signal to noise ratio and necessary scan duration. *Neuroimage* 2007; **34**: 565–74.

23 Van Dijk KR, Sabuncu MR, Buckner RL. The influence of head motion on intrinsic functional connectivity MRI. *Neuroimage* 2012; **59**: 431–8.

24 Martinez D, Slifstein M, Broft A, Mawlawi O, Hwang DR, Huang Y, et al. Imaging human mesolimbic dopamine transmission with positron emission tomography. Part II: amphetamine-induced dopamine release in the functional subdivisions of the striatum. *J Cereb Blood Flow Metab* 2003; **23**: 285–300.

25 Birn RM, Murphy K, Bandettini PA. The effect of respiration variations on independent component analysis results of resting state functional connectivity. *Hum Brain Mapp* 2008; **29**: 740–50.

26 Woods SW. Chlorpromazine equivalent doses for the newer atypical antipsychotics. *J Clin Psychiatry* 2003; **64**: 663–7.

27 Dandash O, Fornito A, Lee J, Keefe RS, Chee MW, Adcock RA, et al. Altered striatal functional connectivity in subjects with an at-risk mental state for psychosis. *Schizophr Bull* 2014; **40**: 903–14.

28 Orliac F, Naveau M, Joliot M, Delcroix N, Razafimandimby A, Brazo P, et al. Links among resting-state default-mode network, salience network, and symptomatology in schizophrenia. *Schizophr Res* 2013; **148**: 74–80.

29 Manoliu A, Meng C, Brandl F, Doll A, Tahmasian M, Scherr M, et al. Insular dysfunction within the salience network is associated with severity of symptoms and aberrant inter-network connectivity in major depressive disorder. *Front Hum Neurosci* 2013; **7**: 930.

30 Craig AD. How do you feel? Interoception: the sense of the physiological condition of the body. *Nat Rev Neurosci* 2002; **3**: 655–66.

31 Fletcher PC, Frith CD. Perceiving is believing: a Bayesian approach to explaining the positive symptoms of schizophrenia. *Nat Rev Neurosci* 2009; **10**: 48–58.

32 Corlett PR, Taylor JR, Wang XJ, Fletcher PC, Krystal JH. Toward a neurobiology of delusions. *Prog Neurobiol* 2010; **92**: 345–69.

33 Palaniyappan L, White TP, Liddle PF. The concept of salience network dysfunction in schizophrenia: from neuroimaging observations to therapeutic opportunities. *Curr Top Med Chem* 2012; **12**: 2324–38.

34 Kapur S. Psychosis as a state of aberrant salience: a framework linking biology, phenomenology, and pharmacology in schizophrenia. *Am J Psychiatry* 2003; **160**: 13–23.

35 Kapur S, Mizrahi R, Li M. From dopamine to salience to psychosis – linking biology, pharmacology and phenomenology of psychosis. *Schizophr Res* 2005; **79**: 59–68.

36 Murray GK, Corlett PR, Clark L, Pessiglione M, Blackwell AD, Honey G, et al. Substantia nigra/ventral tegmental reward prediction error disruption in psychosis. *Mol Psychiatry* 2008; **13**: 67–76.

37 Palaniyappan L, Simmonite M, White TP, Liddle EB, Liddle PF. Neural primacy of the salience processing system in schizophrenia. *Neuron* 2013; **79**: 814–28.

38 Cole DM, Oei NY, Soeter RP, Both S, van Gerven JM, Rombouts SA, et al. Dopamine-dependent architecture of cortico-subcortical network connectivity. *Cereb Cortex* 2013; **23**: 1509–16.

39 Lui S, Li T, Deng W, Jiang L, Wu Q, Tang H, et al. Short-term effects of antipsychotic treatment on cerebral function in drug-naive first-episode schizophrenia revealed by ''resting state'' functional magnetic resonance imaging. *Arch Gen Psychiatry* 2010; **67**: 783–92.

40 Sambataro F, Blasi G, Fazio L, Caforio G, Taurisano P, Romano R, et al. Treatment with olanzapine is associated with modulation of the default mode network in patients with schizophrenia. *Neuropsychopharmacology* 2010; **35**: 904–12.

doi:10.1093/brain/awt290 Brain 2014: 137; 598–609 | 598

BRAIN
A JOURNAL OF NEUROLOGY

Aberrant topology of striatum's connectivity is associated with the number of episodes in depression

Chun Meng,[1,2,3,*] Felix Brandl,[1,2,*] Masoud Tahmasian,[1,2,4] Junming Shao,[1,2] Andrei Manoliu,[1,2,5] Martin Scherr,[5,6] Dirk Schwerthöffer,[5] Josef Bäuml,[5] Hans Förstl,[5] Claus Zimmer,[1] Afra M. Wohlschläger,[1,2,3,7] Valentin Riedl[1,2,4] and Christian Sorg[1,2,5]

1 Department of Neuroradiology, Technische Universität München TUM, Ismaninger Strasse 22, 81675 Munich, Germany
2 TUM-Neuroimaging Centre of Klinikum rechts der Isar, Technische Universität München TUM, Ismaninger Strasse 22, 81675 Munich, Germany
3 Graduate School of Systemic Neurosciences GSN, Ludwig-Maximilians-Universität München LMU, Biocenter, Großhaderner Strasse 2, 82152 Munich, Germany
4 Department of Nuclear Medicine, Technische Universität München TUM, Ismaninger Strasse 22, 81675 Munich, Germany
5 Department of Psychiatry, Technische Universität München TUM, Ismaninger Strasse 22, 81675 Munich, Germany
6 Department of Neurology, Christian Doppler Klinik, Paracelsus Medical University Salzburg, Ignaz-Harrer-Straße 79, 5020 Salzburg, Austria
7 Department of Neurology, Technische Universität München TUM, Ismaninger Strasse 22, 81675 Munich, Germany

*These authors contributed equally to this work.

Correspondence to: Christian Sorg,
Department of Psychiatry and Neuroradiology,
Klinikum rechts der Isar,
Technische Universität München,
Ismaninger Strasse 22,
81675 Munich,
Germany
E-mail: c.sorg@lrz.tu-muenchen.de

In major depressive disorder, depressive episodes reoccur in ~60% of cases; however, neural mechanisms of depressive relapse are poorly understood. Depressive episodes are characterized by aberrant topology of the brain's intrinsic functional connectivity network, and the number of episodes is one of the most important predictors for depressive relapse. In this study we hypothesized that specific changes of the topology of intrinsic connectivity interact with the course of episodes in recurrent depressive disorder. To address this hypothesis, we investigated which changes of connectivity topology are associated with the number of episodes in patients, independently of current symptoms and disease duration. Fifty subjects were recruited including 25 depressive patients (two to 10 episodes) and 25 gender- and age-matched control subjects. Resting-state functional magnetic resonance imaging, Harvard-Oxford brain atlas, wavelet-transformation of atlas-shaped regional time-series, and their pairwise Pearson's correlation were used to define individual connectivity matrices. Matrices were analysed by graph-based methods, resulting in outcome measures that were used as surrogates of intrinsic network topology. Topological scores were subsequently compared across groups, and, for patients only, related with the number of depressive episodes and current symptoms by partial correlation analysis. Concerning the whole brain connectivity network of patients, small-world topology was preserved but global efficiency was reduced and global betweenness-centrality increased. Aberrant nodal efficiency and centrality of regional connectivity was found in the dorsal striatum, inferior frontal and orbitofrontal cortex as well as in the occipital and somatosensory cortex. Inferior frontal changes were associated with current symptoms, whereas aberrant right putamen network topology was associated with the number of episodes. Results were controlled for effects of total grey matter volume, medi-

Received January 24, 2013. Revised August 20, 2013. Accepted September 2, 2013. Advance Access publication October 26, 2013

cation, and total disease duration. This finding provides first evidence that in major depressive disorder aberrant topology of the right putamen's intrinsic connectivity pattern is associated with the course of depressive episodes, independently of current symptoms, medication status and disease duration. Data suggest that the reorganization of striatal connectivity may interact with the course of episodes in depression thereby contributing to depressive relapse risk.

Keywords: major depressive disorder; recurrent episodes; striatum; intrinsic functional connectivity; graph analysis
Abbreviation: HAM-D = Hamilton Rating Scale for Depression

Introduction

Major depressive disorder is one of the most frequent psychiatric disorders with a lifetime prevalence of ~16% (Kessler *et al.*, 2003). Major depression is characterized by single or recurrent major depressive episodes, which include depressed mood, reduced energy, impaired cognition, vegetative symptoms, and suicidal tendency with suicide rates of 4% (American Psychiatric Association, 2000). In 35–85% of cases the course of major depression includes the recurrence of depressive episodes (Hardeveld *et al.*, 2010; Lewis *et al.*, 2010; Farb *et al.*, 2011). However, our knowledge about factors and mechanisms contributing to episode relapse is only fragmentary.

Depressive episodes are associated with widespread structural and functional brain changes (Greicius *et al.*, 2007; Erk *et al.*, 2010; Sheline *et al.*, 2010; Aizenstein *et al.*, 2011; Lui *et al.*, 2011; Li *et al.*, 2012; Mwangi *et al.*, 2012; Zeng *et al.*, 2012; for review Savitz and Drevets, 2009; Hamilton *et al.*, 2012; Whitfield-Gabrieli and Ford, 2012). For example, aberrant resting-state functional connectivity, which has been proved to separate patients from healthy control subjects by pattern classification, was found in the default mode network, salience network, occipital areas, subcortical areas and the cerebellum (Zeng *et al.*, 2012). Particularly, connectivity changes in the default mode and salience networks, which are both intrinsic networks of synchronous ongoing activity (Greicius *et al.*, 2007; Seeley *et al.*, 2007), have been linked with patients' impaired self-focused processing and aberrant emotional reactivity (Sheline *et al.*, 2010; Hamilton *et al.*, 2011, 2012; Whitfield-Gabrieli and Ford, 2012). These widespread functional brain changes, which are detectable even during rest, indicate altered large-scale organization of intrinsic brain activity in depressive episodes. Graph-based network analysis allows us to map such brain organization changes by quantifying topological properties of functional networks consisting of nodes (i.e. brain regions) and edges (i.e. functional connectivity between regions) (Bullmore and Sporns, 2009). Using resting-state functional MRI and graph-based methods, Zhang *et al.* (2011) found aberrant global efficiency of the whole brain intrinsic functional connectivity network as well as changed nodal centrality of specific brain regions' connectivity in patients with first depressive episode. Such aberrant topology of connectivity during episodes is modulated by early life experience such as childhood neglect (Wang *et al.*, 2013), and its modularity (i.e. the organization in ensembles of regions with strong within-module functional connectivity) is distinctively changed depending on whether patients suffer from their first or long-term therapy resistant episode (Tao *et al.*, 2013). Because of these findings we hypothesized that specific changes of the topology of intrinsic connectivity, particularly those reflecting functional integration (i.e. efficiency, centrality or modularity), may interact with the course of major depression.

Besides sub-depressive residuals, the number of previous depressive episodes has strongest influence on the course of major depression (Kendler *et al.*, 2001; Hardeveld *et al.*, 2010; Moylan *et al.*, 2013). A recent meta-analysis demonstrated the number of episodes to be one of the best predictors for the episode relapse risk in major depression (Hardeveld *et al.*, 2010). However, it remains poorly understood which neural mechanisms might contribute to such relationship (Robinson and Sahakian, 2008). Because of the course-sensitive aberrant topology of brain connectivity during episodes, we hypothesized that selective changes of intrinsic connectivity, which reflect altered functional integration, interact with the course of episodes in major depression. In more detail, we aimed to address the question whether and how the topology of intrinsic functional connectivity is related to the number of episodes in patients with recurrent major depression, independently of current symptoms and the total duration of the disease.

Therefore, patients with recurrent major depression and healthy control subjects were assessed by resting-state functional MRI and graph-based analysis. Resting-state blood oxygenation level-dependent signal fluctuations were used as a surrogate for intrinsic brain activity (Fox and Raichle, 2007; Raichle, 2010). Graph-based topological scores were restricted to measures of functional integration (i.e. estimates reflecting the efficiency of the interaction between distributed brain areas) and centrality (i.e. degree and betweenness-centrality both reflecting the importance of nodes for functional integration) (Rubinov and Sporns, 2010). We used the Harvard-Oxford brain atlas and functional connectivity across regions to determine each subject's functional connectivity matrix. Topological scores were derived from these matrices, compared across groups and, in patients only, related to the number of depressive episodes and current depressive symptoms by partial correlation analysis. Because of previous findings that demonstrate a link between structural changes and the course of major depression (Sheline *et al.*, 1999; MacQueen *et al.*, 2003; Frodl *et al.*, 2008; Kronmuller *et al.*, 2009), we controlled analyses for structural changes. In addition, effects of medication, disease duration, and accumulated stress, which may interact with the course of depression (Robinson and Sahakian, 2008; Hardeveld *et al.*, 2010), were controlled.

Materials and methods

Subjects

Twenty-five patients with recurrent major depression (two to 10 depressive episodes; mean age of 48.8 years; 13 female) and 25 healthy persons (mean age of 44.0 years; 14 female) participated in this study (Table 1). All participants provided informed consent in accordance with the Human Research Committee guidelines of the Klinikum rechts der Isar, Technische Universität München. Patients were recruited from the Department of Psychiatry by treating psychiatrists, healthy control subjects from the area of Munich by word-of-mouth advertizing. Participants' examination included medical history, psychiatric interview, and psychometric assessment. Psychiatric diagnoses were based on Diagnostic and Statistical Manual of Mental Disorders-IV (DSM-IV; American Psychiatric Association, 2000). The Structured Clinical Interview for DSM-IV (SCID) was used to assess the presence of psychiatric diagnoses (Spitzer *et al.*, 1992). Severity of clinical symptoms was measured with the Hamilton Rating Scale for Depression (HAM-D; Hamilton, 1960). The global level of social, occupational, and psychological functioning was measured with the Global Assessment of Functioning Scale (Spitzer *et al.*, 1992). Psychiatrists D.S. and M.S. performed clinical-psychometric assessment; they have been professionally trained for SCID interviews with inter-rater reliability for diagnoses and scores of >95%.

Recurrent major depression was the primary diagnosis for all patients. Patients with recurrent major depression constitute a heterogeneous clinical group, varying in severity of current symptoms, age of disorder onset, duration of the disorder, number of depressive episodes, family history of major depression, co-morbidity of other disorders, and type of medication. Since the goal of the present study was to determine the relationship between the topology of the brain's functional connectivity network and the course of major depression common to most patients with recurrent major depression, we adopted selection criteria from a previous study on recurrent major depression to obtain a clinically representative patient sample (Hennings *et al.*, 2009). Recurrence implies the return of an entirely new episode after clinical recovery. Due to the unreliable self-report in major depression because of patients' potential memory problems, the determination of episode number was based on the review of patients' medical records. Only patients whose records enabled us to determine a consistent episode number were included in the study. The number of episodes of all patients ranged from two to 10 following a continuous distribution (Supplementary Fig. 1). All patients met criteria for a current depressive episode with an average episode length of 16.6 weeks [standard deviation (SD) 6.6] and an averaged HAM-D score of 22 (SD 7.1). The average age of major depression onset was 32 years (SD 8), and all patients experienced their first episode before 45 years of age. The average duration of major depression was 16.7 years (SD 10.2) and on average, patients had experienced five to six episodes (mean 5.6, SD 2.5). On average 1.7 episodes (SD 1.1) were triggered by stressful life events; episodes triggered by a stressful life event were defined as episodes that started within 1 month after a stressful life event. Four patients had a positive family history of major depression. Fourteen patients had psychiatric co-morbidities: six generalized anxiety disorder, three somatization disorder, and five avoidant or dependent personality disorders. Patients with psychotic symptoms, schizophrenia, schizoaffective disorder, bipolar disorder, and substance abuse were excluded from this study. Additional exclusion criteria were pregnancy, neurological or severe internal systemic diseases, and general contraindications for MRI. One patient was free of any psychotropic medication during MRI assessment. Seven patients were treated by antidepressant mono-therapy [three cases: citalopram 30 mg/d (mean dose); three cases: sertraline 200 mg/d; one case: mirtazapine 30 mg/d]; 12 patients by dual-therapy (five cases: citalopram 37.5 mg/d + mirtazapine 30 mg/d; two cases: citalopram 40 mg/d + venlafaxine 225 mg/d; one case: citalopram 30 mg/d + quetiapine 200 mg/d; one case: sertraline 200 mg/d + mirtazapine 30 mg/d; three cases: venlafaxine 225 mg/d + mirtazapine 30 mg/d); and five patients by triple-therapy (two cases: citalopram 30 mg/d + venlafaxine 187.5 mg/d + amisulprid 200 mg/d; two cases: citalopram 30 mg/d + mirtazapine 30 mg/d + quetiapine 200 mg/d; 1 case: venlafaxine 22 mg/d + mirtazapine 30 mg/d + quetiapine 200 mg/d). All healthy control subjects were free of any current or past neurological or psychiatric disorder or psychotropic medication.

Table 1 Demographic, clinical and psychometric data

	Patients with major depression	Healthy controls	*P*-value
Subjects [total number]	25	25	
Age [years]	48.76 (14.83)	44.08 (14.78)	>0.05
Gender	13F/12M	14F/11M	>0.05
Number of episodes	5.6 (2.5)	NA	
Duration of major depression [years]	16.7 (10.2)	NA	
Current episode			
Duration [weeks]	16.6 (6.6)	NA	
HAM-D	22 (7.1)	0	<0.001
GAF	50 (10.5)	99.5 (1.1)	<0.001

Group comparisons: two-sample *t*-tests for age, HAM-D, and GAF; χ^2-test for gender. Data are presented as mean and SD (in brackets). GAF = Global Assessment of Functioning.

Data acquisition and preprocessing

All participants underwent 10 min of resting-state functional MRI with the instruction to keep their eyes closed and not to fall asleep. We verified that subjects stayed awake by interrogating via intercom immediately after the resting-state functional MRI scan. No patient dropped out during the scanning session.

Data acquisition

MRI was performed on a 3 T MR scanner (Achieva, Philips) using an 8-channel phased-array head coil. For co-registration and volumetric analysis, T_1-weighted anatomical data were obtained by using a MP-RAGE sequence (echo time = 4 ms, repetition time = 9 ms, inversion time = 100 ms, flip angle = 5°, field of view = 240 × 240 mm^2, matrix = 240 × 240, 170 slices, slice thickness = 1 mm, and 0 mm interslice gap, voxel size = 1 × 1 × 1 mm^3). Functional MRI data were obtained by using a gradient echo EPI sequence (echo time = 35 ms, repetition time = 2000 ms, flip angle = 82°, field of view = 220 × 220 mm^2, matrix = 80 × 80, 32 slices, slice thickness = 4 mm, and 0 mm interslice gap, voxel size = 2.75 × 2.75 × 4 mm^3; 300 volumes).

Preprocessing

The first three functional images of each subject's data set were discarded because of magnetization effects. The remaining resting-state functional MRI data were preprocessed by SPM8 (Wellcome Department of Cognitive Neurology, London) including head motion correction, spatial normalization into the standard stereotactic space of

the Montreal Neurological Institute with isotropic voxel of $3 \times 3 \times 3\,mm^3$, and spatial smoothing with a $6 \times 6 \times 6\,mm^3$ Gaussian kernel to reduce spatial noise. To ensure data quality, particularly concerning motion-induced artefacts, temporal signal-to-noise ratio and point-to-point head motion were estimated for each subject (Murphy *et al.*, 2007; Van Dijk *et al.*, 2012). Excessive head motion (cumulative motion translation or rotation >3 mm or 3° and mean point-to-point translation or rotation >0.15 mm or 0.1°) was applied as an exclusion criterion. Point-to-point motion was defined as the absolute displacement of each brain volume compared with its previous volume. None of the participants had to be excluded. Two-sample *t*-tests yielded no significant differences between groups regarding mean point-to-point translation or rotation of any direction ($P > 0.10$) as well as temporal signal-to-noise ratio ($P > 0.50$). Further control for head motion effects was carried out in the network construction procedure.

Topological analysis of whole brain functional connectivity network

Network construction

For each subject, the whole brain functional connectivity network was constructed from preprocessed resting-state functional MRI data. We defined 112 nodes by anatomical parcellation of the whole brain using Harvard-Oxford atlas (Supplementary Table 1; FSL, Oxford University). Time series of functional MRI signal were extracted from each voxel and subsequently averaged within each region of interest. The regional time courses were then regressed against confounding covariates (comprising six time courses of head motion and signals derived from whole grey matter, white matter and CSF). Maximal overlap discrete wavelet transform was applied to decompose the residual regional time series into the following four frequency scales: scale 1 (0.125–0.250 Hz), scale 2 (0.060–0.125 Hz), scale 3 (0.030–0.060 Hz) and scale 4 (0.015–0.030 Hz) (Percival and Walden, 2000). Absolute wavelet correlation coefficients at the low-frequency scale 2 (0.060–0.125 Hz) were used for further analysis according to previous studies (Lynall *et al.*, 2010; Alexander-Bloch *et al.*, 2012). Finally, a 112×112 connectivity matrix representing individual whole brain functional connectivity network was obtained for each subject.

Network analysis

To prepare graph-based topological analysis of the functional connectivity network, binary networks were generated for the cost range from 0.05–0.50 (with intervals of 0.01) using Prim's algorithm of minimum spanning tree in-line with previous work (Alexander-Bloch *et al.*, 2012). The cost of a network is defined as the number of existing edges divided by the number of all possible edges and serves as a basic 'economical' constraint on brain networks (Bullmore and Sporns, 2012). Cost range 0.05–0.5 was selected because networks with cost <0.05 are too sparse to obtain stable network topology and those with cost >0.50 become increasingly random and lose their small-world property that is characteristic for human brains (Humphries *et al.*, 2006; Lynall *et al.*, 2010). In addition, to investigate the impact of costs on network topology, four arbitrary quasi-equidistant cost sub-ranges (i.e. 0.05–0.14, 0.15–0.24, 0.25–0.34 and 0.35–0.50) were defined.

Graph analysis of binary networks was carried out in Matlab using the Brain Connectivity Toolbox (Rubinov and Sporns, 2010). Global topological properties of characteristic path length, global efficiency, and global betweenness-centrality (all reflecting functional integration; Rubinov and Sporns, 2010), and clustering coefficient and small-worldness (reflecting functional segregation and its relation to functional integration; Rubinov and Sporns, 2010) were calculated (Supplementary Methods) and averaged across costs for each subject. Group comparison was carried out for each cost sub-range by permutation test (100 000 iterations; $P < 0.05$) controlling for age, gender and total grey matter volume (Supplementary Methods, grey matter volume was provided by structural voxel-based morphometry analysis). Correspondingly, to analyse the topology of nodal connectivity, nodal efficiency and centrality (represented by nodal degree and betweenness-centrality; Rubinov and Sporns, 2010) were calculated and compared across groups (permutation test, 100 000 iterations, $P < 0.05$). One should note that, although efficiency, degree and betweenness-centrality reflect different aspects of functional integration, they are not completely independent among each other (i.e. they correlate significantly for specific nodes (Valente *et al.*, 2008; Lynall *et al.*, 2010; Bassett *et al.*, 2012; Zuo *et al.*, 2012). Nodal analysis was restricted to scores of centrality and efficiency within the low cost sub-range (0.05–0.14) due to results of global property analysis. After previous studies, false positive correction for *N*-node statistical comparison was applied using 1 / (amount of nodes) = 1 / 112 = 0.009 as significance threshold (Lynall *et al.*, 2010).

Partial correlation analysis for topology scores, number of depressive episodes and current symptoms

To analyse the relationship of both the course of major depression and current depressive symptoms with topological properties of nodal connectivity independently of each other, we calculated the partial correlation coefficients between topological scores and both the number of depressive episodes and HAM-D scores in patients ($P < 0.009$, false positive correction); partial correlation analysis was controlled for several variables including particularly structural changes, medication and disease duration (see below). Partial correlation analysis was used because it allows for measuring the degree of association between two random variables (i.e. topological score and number of episodes), with the effect of controlling variables removed (e.g. current symptoms reflected by HAM-D). In more detail, the partial correlation between a given topological score and the number of depressive episodes given controlling variables Z = (HAM-D, age, gender, grey matter volume, duration, medication), written as ρ(Top score, Number of depressive episodes;·Z), is the correlation between the residuals R(Top score) and R(Number of depressive episodes) resulting from the linear regression of Top score with Z and of Number of depressive episodes with Z, respectively. Therefore, a partial correlation-based approach enables the analysis of the relationship between a topological property and the course of major depression while controlling for the effect of current symptoms and vice versa.

To control for potential confounding effects, we included age, gender, grey matter volume, medication, accumulated stress, and disease duration as covariates-of-no-interest into our partial correlation approach. First, the functional connectivity of intrinsic brain networks depends on widespread structural integrity of polysynaptic pathways (Lu *et al.*, 2011). As we focus on changes of functional integration among the whole brain network that are independent of structural changes (MacQueen *et al.*, 2003; Frodl *et al.*, 2008; Kronmuller *et al.*, 2009), we included total grey matter volume scores as covariate-of-no-interest in the above mentioned functional connectivity analyses to control for this influence of structural variations (for structural changes in patients see voxel-based morphometry analysis in the Supplementary Methods). Second, patients of our study were treated by antidepressant medication, which has been demonstrated to affect intrinsic functional connectivity (Delaveau *et al.*, 2011). Therefore,

control for medication effects is necessary. Different from antipsychotic drugs, which can be compared by chlorpromazine equivalents, no comparable approach exists currently for antidepressants. We developed two ways to control for antidepressant effects and evaluated them among each other and with previous findings: (i) we divided applied antidepressants and augmentation medication into four classes (selective serotonin reuptake inhibitor, serotonin-norepinephrine reuptake inhibitor, noradrenergic and specific serotonergic antidepressants, and atypical antipsychotics); then we defined a medication covariate by the number of different classes a patient received in the partial correlation analysis; (ii) in a validation analysis, we defined four covariates (i.e. one for each medication class) with numbers 1 or 0: 1 means the patient was treated by this medication class whereas 0 means they were not. Third, as we were interested in the relationship between nodal connectivity topology and number of episodes independent of disease duration and accumulated stress, we included disease duration and the number of episodes triggered by stressful life events as additional covariates. Thereby we assume that the number of such stress-triggered episodes reflects patient's accumulated stress relevant for depression course.

Results

Global and regional atrophy in patients

Patients' total grey matter volume was reduced; regional brain volume reduction was found in the anterior cingulate cortex, dorsal prefrontal cortex, and hippocampus amongst other areas (Supplementary Fig. 2 and Supplementary Table 2). This result is in line with previous findings (Savitz and Drevets, 2009).

Aberrant global functional integration in patients

For the first cost-sub-range from 0.05 to 0.14, all subjects had small-worldness scores >1.22, demonstrating for all subjects brain networks with small-world property (Supplementary Table 3). Across groups, small-worldness and global clustering coefficient did not differ significantly (Fig. 1 and Table 2). In patients, global efficiency was reduced, global betweenness-centrality and characteristic path length were increased (Fig. 1 and Table 2). Cost range analysis revealed that changes of global topological scores were mainly driven by the low-cost sub-range (0.05–0.14), i.e. by connections of strong functional connectivity (Fig. 1).

Aberrant nodal efficiency and centrality in patients

Altered nodal centrality and efficiency of node-centred connectivity was found for several regions in patients (Fig. 2 and Table 3). In the striatum, patients had increased nodal betweenness-centrality in the right putamen and decreased nodal degree and efficiency in the caudate. In the frontal cortex, patients had decreased nodal degree in the inferior frontal gyrus pars triangularis and decreased nodal efficiency in the orbital gyrus. Furthermore, patients had increased nodal degree in the occipito-temporal cortex and decreased nodal betweenness-centrality in the postcentral gyrus.

Depressive symptoms were associated with the nodal connectivity topology of areas known to be part of the salience and default mode networks

To investigate the relationship among connectivity topology, disease course and depressive symptoms, we applied partial correlation analysis of corresponding scores with additional covariates of age, gender, grey matter volume, medication, accumulated stress and disease duration. To control for medication effects, we used two different ways to model medication influences; as results of both models differed only marginally, we report only results of the first model in which the number of medication classes administered to the patient constituted the medication covariate. To facilitate comprehensive evaluation of partial correlation results, we first examined the relationship among covariates by Pearson's correlation: HAM-D and the number of depressive episodes were not correlated ($r = 0.041$, $P = 0.844$); number of depressive episodes was correlated with disease duration ($r = 0.784$, $P < 0.001$), and HAM-D with the number of medication classes administered to the patient ($r = 0.569$, $P = 0.003$). No further covariate showed significant correlation with number of depressive episodes or HAM-D ($P > 0.05$). Additionally, total grey matter volume was significantly correlated with age ($r = -0.649$, $P = 0.0004$) and disease duration was also correlated with age ($r = 0.459$, $P = 0.021$). For partial correlation results regarding connectivity topology, critically, we found that patients' HAM-D scores were negatively correlated with nodal degree of the inferior frontal gyrus and positively correlated with nodal betweenness-centrality of the posterior supramarginal gyrus (Table 4). The inferior frontal gyrus is a hub of the salience network, and the posterior supramarginal gyrus of the default mode network.

The number of depressive episodes is associated with aberrant topology of striatal connectivity independently of current symptoms

In patients' right putamen, the number of depressive episodes was positively correlated with nodal efficiency of connectivity, independently of current symptoms, medication status, disease duration and additional covariates (Fig. 3 and Table 4). In addition, significant association between nodal degree of the nucleus accumbens' connectivity and number of depressive episodes was found (Fig. 3 and Table 4).

Discussion

To analyse how the topology of the brain's intrinsic functional connectivity network is linked with the course of depressive episodes in major depression, we applied resting-state functional MRI and

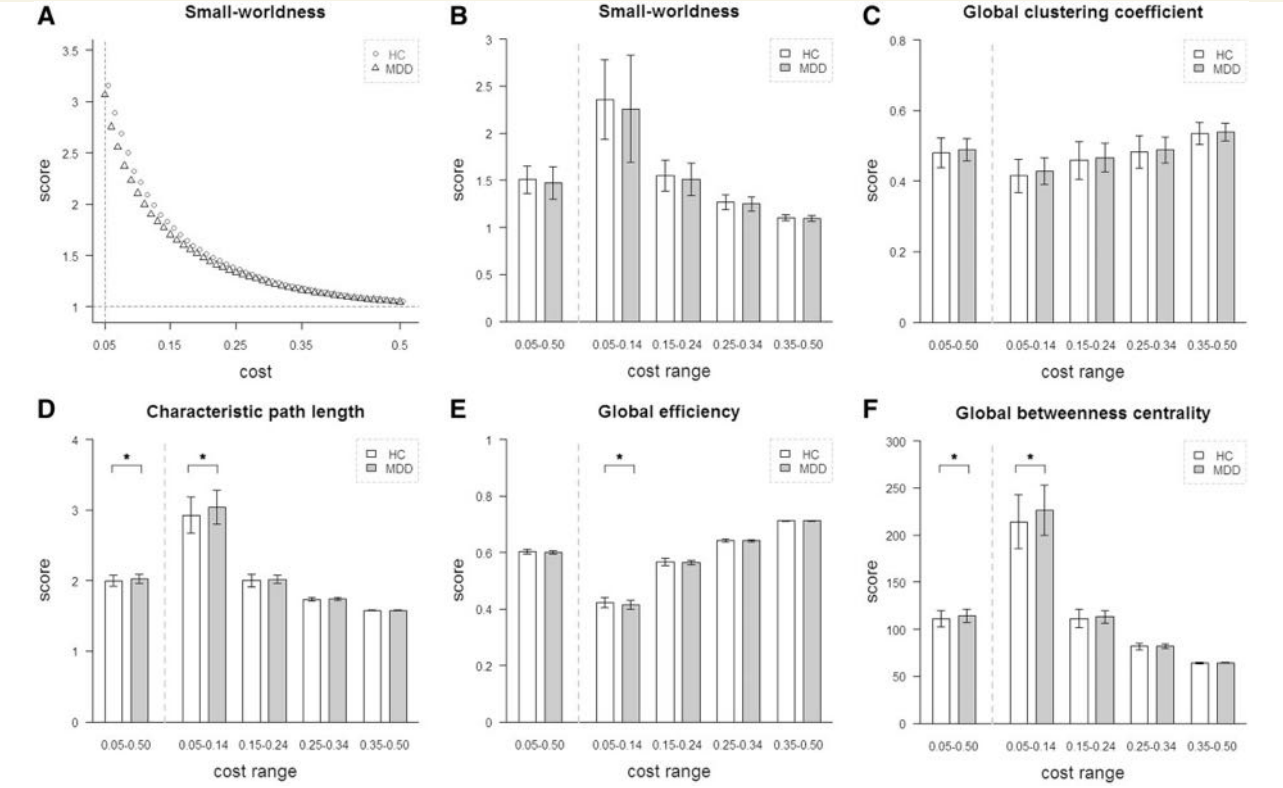

Figure 1 Global network topology in recurrent major depression. Group comparisons were based on permutation tests controlled for age, gender, and grey matter, $P < 0.05$, 100 000 permutations. (**A**) For both groups of healthy control subjects (HC) and patients with recurrent major depression (MDD), whole brain intrinsic functional connectivity networks had small-world architecture (>1.22) for the investigated cost range (0.05–0.50). Small-world properties decrease with increasing network costs. At the cost of 0.14, averaged small-worldness was 1.77 in major depression and 1.83 in control subjects. (**B** and **C**) Small-worldness and global clustering coefficient were not significantly different across groups. (**D–F**) Significant group differences were found for characteristic path length ($P = 0.029$), global efficiency ($P = 0.029$), and global betweenness-centrality ($P = 0.029$) for the cost sub-range (0.05–0.14) (i.e. for networks of spatially sparse but strong functional connectivity). *Significant group difference.

Table 2 Global topological network properties in recurrent major depression

	Healthy controls	Patients with MDD	*P*-Value
Small-worldness	2.344 ± 0.407	2.271 ± 0.570	0.300
Global clustering coefficient	0.412 ± 0.044	0.431 ± 0.037	0.055
Characteristic path length	2.923 ± 0.244	3.049 ± 0.215	0.029*
Global efficiency	0.423 ± 0.018	0.414 ± 0.014	0.029*
Global betweenness-centrality	213.492 ± 27.086	227.438 ± 23.841	0.029*

Group comparisons: permutation tests (100 000 permutations); *Significant result for $P < 0.05$; group comparisons were controlled for age, gender, and total grey matter volume. Global network scores are reported as mean and SD for cost sub-range 0.05-0.14. MDD = major depressive disorder.

graph-based network analysis in patients with recurrent major depression, and healthy control subjects. We found selective association between aberrant topology of the right putamen's connectivity and patients' number of depressive episodes, independently of current depressive symptoms, medication status, accumulated stress and disease duration. This result provides first evidence that intrinsic functional network organization is linked with the course of major depression, more specifically that the aberrant topology of striatal connectivity is associated with the number of episodes in depression. Data suggest that striatum's connectivity may interact with the course of depressive episodes, potentially contributing to depressive relapse risk in major depression.

Aberrant topology of striatal connectivity is associated with the course of major depression

Topology of striatal connectivity was found to be associated with the course of depressive episodes in patients with recurrent major

depression (Fig. 3, Tables 3 and 4). Specifically, we found a positive correlation between the number of episodes of major depression and nodal efficiency of right putamen intrinsic connectivity in patients (Fig. 3 and Table 4). Right putamen's centrality was significantly increased in patients (Fig. 2 and Table 3), i.e. the stronger the putamen's hubness, the more depressive episodes. Both efficiency and centrality (the latter comprising degree and betweenness-centrality) reflect functional integration in the brain i.e. the ability to rapidly combine information from distributed brain regions (Bullmore and Sporns, 2009; Rubinov and Sporns, 2010). Furthermore, we found correspondent results for the ventral striatum (Fig. 3 and Table 4) (i.e. we found a positive correlation between nucleus accumbens' centrality and the number of depressive episodes), suggesting that the topology of whole striatum's connectivity is associated with the course of episodes in major depression. Findings were not explained by age, gender, medication effects or total grey matter changes, for which we controlled statistically. Findings were also controlled for total disease duration and number of episodes triggered by stressful life events, suggesting that specifically the number of episodes and not disease duration or accumulated stress is linked with the topology of striatal connectivity. Importantly, results were also controlled for the degree of current symptoms, indicating that the topology of striatal connectivity reflects major depression's course rather than its symptoms.

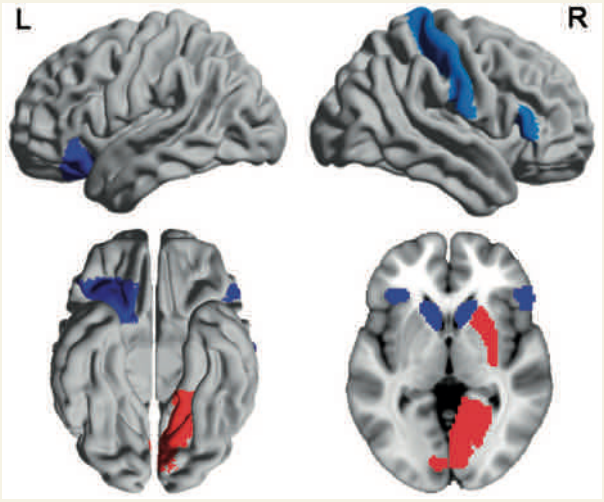

Figure 2 Brain regions with aberrant nodal efficiency and centrality in recurrent major depression. Group comparisons were based on permutation tests controlled for age, gender and grey matter volume, $P < 0.009$ based on false positive correction for multiple testing, 100 000 permutations. Coloured regions indicate significantly changed nodal intrinsic functional connectivity network topology (i.e. nodal efficiency or centrality) in patients. Blue/red indicates decrease/increase of a topological property in patients. For more details see Table 3. L = left; R = right. This figure was visualized with the BrainNet Viewer (http://www.nitrc.org/projects/bnv/).

Between-group differences of nodal network topology included bilateral caudate and right putamen (Fig. 2 and Table 3). Putamen's intrinsic functional connectivity pattern is preferentially linked with the insula and anterior cingulate cortex, i.e. with key regions of the salience network, whereas the caudate's connectivity links more with areas of the default mode network (such as the medial prefrontal and posterior cingulate cortex) (Di Martino *et al.*, 2008). Both salience and default mode networks are strongly involved in major depression (Greicius *et al.*, 2007; Sheline *et al.*, 2010; Hamilton *et al.*, 2011; for review Whitfield-Gabrieli and Ford, 2012; Hamilton *et al.*, 2013). A previous study reported increased putamen and caudate centrality/efficiency in first-episode major depression patients (Zhang *et al.*, 2011). Concerning putamen we found consistent results in patients with recurrent major depression, and concerning caudate we found reduced centrality and efficiency in patients with recurrent major depression. It might be that within the dorsal striatum, network topology of sub-areas (like putamen and caudate) develops distinctively in the course of recurrent major depression potentially because of a specific intrinsic connectivity pattern (see further

Table 3 Nodal network topology in recurrent major depression

Lobe	Node / Region of interest	Side	Mode	Healthy controls	Patients with MDD	P-Value
Patients with MDD > Healthy controls						
Subcortical	Putamen	R	BC	175.898 ± 126.037	346.133 ± 230.110	<0.001
Occipital	Intracalcarine cortex	R	Deg	7.672 ± 4.071	11.031 ± 4.838	0.006
		L	Deg	7.615 ± 4.095	12.446 ± 5.376	<0.001
	Lingual gyrus	R	Deg	8.649 ± 4.593	12.801 ± 6.334	0.005
Patients with MDD < Healthy controls						
Subcortical	Caudate	R	E_{nodal}	0.390 ± 0.071	0.319 ± 0.088	0.002
		L	Deg	9.162 ± 5.632	5.071 ± 4.237	0.002
			E_{nodal}	0.402 ± 0.074	0.325 ± 0.081	0.001
Frontal	Frontal orbital cortex	L	E_{nodal}	0.462 ± 0.048	0.417 ± 0.059	0.003
	Inferior frontal gyrus, pars triangularis	R	Deg	10.010 ± 5.859	6.158 ± 3.543	0.003
Sensorimotor	Postcentral gyrus	R	BC	234.044 ± 154.870	138.132 ± 78.231	0.004

Group comparisons: permutation tests (100 000 permutations); reported results are significant for $P < 0.009$ based on false positive correction for multiple testing; group comparisons were controlled for age, gender and total grey matter volume. Nodal network scores are reported for cost sub-range 0.05-0.14 as mean and SD. MDD = major depressive disorder; R = right; L = left; BC = nodal betweenness-centrality; Deg = nodal degree; E_{nodal} = nodal efficiency.

Table 4 Nodal network topology: partial correlation with depressive symptoms (HAM-D) and major depression course (number of depressive episodes), respectively

Lobe	Node / Region of interest	Side	Mode	r-Value	*P*-value
Association between nodal network topology and depressive symptoms					
Frontal	Inferior frontal gyrus, pars triangularis	R	Deg	−0.614	0.005
Parietal	Supramarginal gyrus, posterior division	R	BC	0.688	0.001
Association between nodal network topology and number of depressive episodes					
Subcortical	Putamen	R	E_{nodal}	0.588	0.008
	Accumbens	R	Deg	0.586	0.008

Partial correlation analyses were corrected for age, gender, total grey matter volume, disease duration, and medication effects; reported results are significant for $P < 0.009$ based on false positive correction for multiple comparison. Regional network scores are based on cost sub-range 0.05–0.14. R = right; L = left; Deg = nodal degree; E_{nodal} = nodal efficiency; BC = nodal betweenness-centrality.

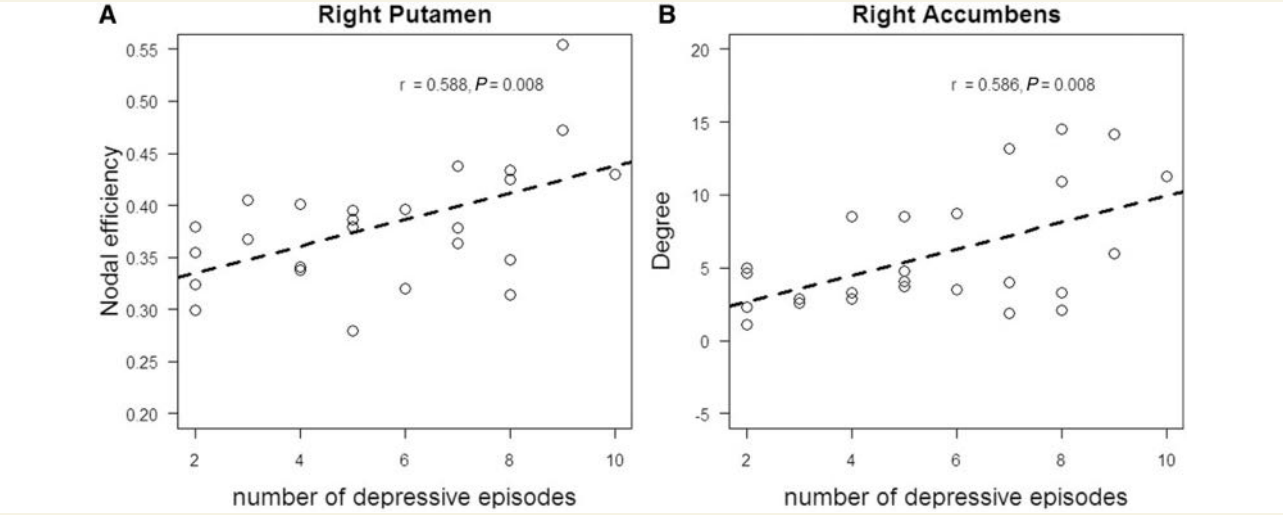

Figure 3 Association between striatal connectivity topology and number of depressive episodes in patients with recurrent major depression, independently of current symptoms and disease duration. Partial correlation analysis of nodal topological scores and number of depressive episodes, including additional covariates of current symptoms, age, gender, grey matter brain volume, medication effects and disease duration, $P < 0.009$ based on false positive correction for multiple testing. Scatter plots reflect significant correlations between different striatal network scores and the number of depressive episodes in patients with recurrent major depression.

support for this argument below). However, we cannot exclude the potential influence of methodological differences between the previous and our study [e.g. Zhang *et al*. (2011) applied a brain atlas different from that of our study; such atlas-based parcellation change may shift the network topology result; Wang *et al.* (2009)]. Future studies, which should be designed to study explicitly data of both first and recurrent episode major depression, are necessary to compare directly network topology changes within one methodological framework.

Two lines of research highlight the importance of the striatum (particularly of the right putamen) for major depression: (i) Impaired emotion processing in major depression: a recent meta-analysis in major depression, which integrated PET-based metabolic resting-state findings with functional MRI data of emotional stimulation, found that patients' aberrant striatal activity might prevent critically the regulatory impact of the prefrontal cortex on increased emotional processing in limbic-insular areas (Hamilton *et al.*, 2012). The authors suggest that changes of striatal connectivity (particularly of the dorsal striatum) may contribute to this regulatory deficit, potentially because of lowered striatal dopamine levels (Hamilton *et al.*, 2012). Our result is consistent with this idea, highlighting explicitly the important role of increasingly changed topology of striatal connectivity for the course of major depression; and (ii) Impaired emotional learning in major depression: furthermore, dopamine-dependent striatal activity is essential for reinforcement learning (Liljeholm and O'Doherty, 2012). This type of learning is impaired in major depression (Eshel and Roiser, 2010). For example, during reversal learning, right putamen responses for unexpected reward were selectively reduced in patients with major depression (Robinson *et al.*, 2012). The authors suggest that a reward-related dysfunction of the right putamen within a striatum-centred prefrontal-limbic circuit may inhibit the learning of appreciating and enjoying positive life experience; such positive experience, in turn, is critical for depressive

recovery. Our result is consistent with this idea, specifying that right putamen's connectivity topology might be relevant for such adaptive processes in major depression. In summary, aberrant topology of striatal connectivity and its link with the course of depressive episodes are consistent with models of impaired emotion regulation and dopamine-dependent reward learning in major depression.

Aberrant topology of striatal connectivity and depressive relapse risk

Aberrant topology of striatal connectivity might be a potential mechanism to mediate the relapse risk in major depression. Depressive episodes are associated with both the change of network topology (Figs 1 and 2) and the increase of episode relapse risk (Hardeveld *et al.*, 2010). Here we found that the amount of episodes is specifically linked with aberrant topology of striatal connectivity (Fig. 3). This link suggests striatal topology as neural correlate for the course of episodes in major depression, and therefore of episode relapse. This argument makes topology of striatal connectivity a potential biomarker to evaluate depressive recurrence risk.

Aberrant nodal network topology in areas of the salience network is associated with current depressive symptoms

Beyond the striatum, aberrant nodal centrality and efficiency was found in the inferior frontal gyrus, the orbitofrontal cortex as well as in the occipital and somatosensory cortex (Fig. 2 and Table 3). This finding was not influenced by age, gender, medication status, or total grey matter reduction. With respect to affected regions, our result matches perfectly previous findings in first-episode major depression (Zhang *et al.*, 2011); as mentioned above for the caudate, the direction of changes was different for some regions (e.g. patients' lingual or calcarine centrality was reduced in the previous but increased in our study). Nodal degree and efficiency of inferior frontal gyrus' and posterior supramarginal gyrus' connectivity, respectively, was specifically associated with depressive symptoms measured by the HAM-D (Table 4). These areas are key regions of the salience and default mode network, which both are critically involved in depressive symptoms such as rumination or aberrant emotional reactivity (Greicius *et al.*, 2007; Sheline *et al.*, 2010; Hamilton *et al.*, 2011, 2013; Whitfield-Gabrieli and Ford, 2012). Aberrant network topology and the association of network topology with depressive symptom severity overlapped in the inferior frontal gyrus of the salience network (Tables 3 and 4). This result suggests that topological changes of the cortical salience network reflect major depression symptoms, whereas those of the subcortical striatum are associated with the course of major depression. This finding is in line with the more general idea about cortex-basal-ganglia (including striatum)-thalamus-cortex loops, where the cortex itself initially generates action/cognition/affective candidates, between which the basal ganglia then arbitrate (likely based on their learned reinforcement probabilities) to facilitate (gate) the 'best' one (for review see Maia and Frank, 2011).

Aberrant global network topology in recurrent major depression: impact on the backbone network

Concerning global topology of functional connectivity, we found selectively aberrant functional integration (decreased global efficiency and increased global betweenness-centrality) in patients, whereas other topological properties (small-worldness and clustering coefficient) were not significantly different across groups (Fig. 1 and Table 2). In general, global topological scores are derived from correspondent nodal scores by different forms of averaging. Because of the correspondence of decreased global efficiency/decreased caudate efficiency and increased global betweenness-centrality/increased putamen betweenness-centrality, selective reorganization of global functional integration seems to depend mainly on the reorganization of striatal connectivity in major depression, emphasizing the prominent role of striatal connectivity in recurrent major depression.

Furthermore, changes of global network topology are driven by low-cost networks i.e. by networks that include edges of particularly strong intrinsic functional connectivity. Across investigated cost-sub-ranges, significant group differences of network topology focus on the cost-sub-range of 0.05–0.14, which is related to sparse networks and strong connectivity (Fig. 1). This means that recurrent major depression is selectively associated with changes in widespread (whole brain) strong (top 14%) functional connections, which are supposed to constitute the backbone of the brain network. Previous studies found that backbone networks consist mainly of both network hubs and strong long-distance edges (Serrano *et al.*, 2009; van den Heuvel *et al.*, 2012; Markov *et al.*, 2013). Correspondingly, we found global and nodal centrality, which are both related to such hubness, to be altered in patients. Taken together, these data indicate that major depression is particularly associated with changes in the brain's backbone network.

Methodological issues and limitations

To evaluate results of the current study appropriately, some methodological issues have to be considered. Issues concerning patient sample and chosen graph approach are discussed below and, issues concerning study design and imaging data analysis are discussed in the Supplementary Discussion.

Medication

Patients in our study were treated by antidepressant medication. Although recent studies suggest that antidepressants normalize brain function (Anand *et al.*, 2005; Fu *et al.*, 2007; Heller *et al.*, 2013), the impact of antidepressants on intrinsic functional connectivity is so far incompletely understood (Bruhl *et al.*, 2010; Delaveau *et al.*, 2011). To control for potential impact of medication, we modelled medication effects and added corresponding covariates into statistical analyses. As no canonical way to account

for antidepressants effects is available, we tested two different models, which yielded almost identical results. Further, we found that medication status was associated with the degree of current symptoms but not with the number of episodes, suggesting that at least during a current episode the amount of applied antidepressants is independent of the previous disorder course but dependent on symptom severity. In summary, these findings and the coherence of our results with previous studies (Zhang *et al.*, 2011; Wang *et al.*, 2013), suggest that medication may not critically influence results of our study. Nevertheless, data should be interpreted carefully because of potential medication confounds. Future studies in non-medicated patients are necessary; however, such studies in drug-free patients of recurrent major depression might implicate strong practical and ethical problems.

Binary graph approach

In this study, instead of weighted graphs, the binary undirected graph-based framework was used to analyse the brain's intrinsic functional connectivity network. Binary undirected graphs are defined by edges of either 1 or 0 (i.e. they reflect the presence or absence of connections due to a given threshold), whereas weighted graphs reflect connection strengths by continuous edge scores (Rubinov and Sporns, 2010). The binary approach was chosen for the following reasons: (i) Backbone network and weaker connection analysis: in contrast to weighted graph approaches (Rubinov and Sporns, 2011), binary approaches enable a cost analysis (i.e. an edge density analysis) to evaluate separately the brain's backbone network (defined by strongest edges for all nodes) and the influence of weaker connections (i.e. edges of weaker connectivity strength) on network topology. In particular, we found that major depression is associated with changes in the backbone network; (ii) Comparability between binary and weighted graph approaches: cost integration within binary approaches (i.e. averaging of graph metrics across costs) provides results that are comparable with those derived from weighted graph approaches (Ginestet *et al.*, 2011); and (iii) Comparability with other studies: previous studies of brain network topology in major depression relied on binary undirected graphs (Jin *et al.*, 2011; Zhang *et al.*, 2011; Tao *et al.*, 2013). We used the same framework to enable comparisons among studies. Nevertheless, it should be noted that weighted approaches conserve more information about the whole distribution of edge weights than binary approaches do. Future complementary studies using weighted graphs might be helpful to understand more comprehensively brain organization changes in major depression.

Conclusion

In recurrent major depression aberrant topology of striatal connectivity is associated with the course of depressive episodes independently of current symptoms, medication status, accumulated stress, and disease duration. Therefore, the topology of striatum's intrinsic connectivity may have the potential to predict episode relapse risk in major depression.

Acknowledgements

We are grateful to the participants of the study and the staff of the Department of Psychiatry and Neuroradiology for their help in recruitment and data collection.

Funding

This work was supported by the Chinese Scholar Council (CSC), File No: 2010604026 (C.M.), the German Federal Ministry of Education and Research (BMBF 01EV0710 to A.M.W., BMBF 01ER0803 to C.S.) and the Kommission für Klinische Forschung, Technische Universität München (KKF 8765162 to C.S).

Supplementary material

Supplementary material is available at *Brain* online.

References

Aizenstein HJ, Andreescu C, Edelman KL, Cochran JL, Price J, Butters MA, et al. fMRI correlates of white matter hyperintensities in late-life depression. Am J Psychiatry 2011; 168: 1075–82.

Alexander-Bloch A, Lambiotte R, Roberts B, Giedd J, Gogtay N, Bullmore E. The discovery of population differences in network community structure: new methods and applications to brain functional networks in schizophrenia. Neuroimage 2012; 59: 3889–900.

American Psychiatric Association. Diagnostic and statistical manual of mental disorders. 4th edn, text revision. Washington, DC: American Psychiatric Association; 2000.

Anand A, Li Y, Wang Y, Wu J, Gao S, Bukhari L, et al. Activity and connectivity of brain mood regulating circuit in depression: a functional magnetic resonance study. Biol Psychiatry 2005; 57: 1079–88.

Bassett DS, Nelson BG, Mueller BA, Camchong J, Lim KO. Altered resting state complexity in schizophrenia. Neuroimage 2012; 59: 2196–207.

Bruhl AB, Kaffenberger T, Herwig U. Serotonergic and noradrenergic modulation of emotion processing by single dose antidepressants. Neuropsychopharmacology 2010; 35: 521–33.

Bullmore E, Sporns O. Complex brain networks: graph theoretical analysis of structural and functional systems. Nat Rev Neurosci 2009; 10: 186–98.

Bullmore E, Sporns O. The economy of brain network organization. Nat Rev Neurosci 2012; 13: 336–49.

Delaveau P, Jabourian M, Lemogne C, Guionnet S, Bergouignan L, Fossati P. Brain effects of antidepressants in major depression: a meta-analysis of emotional processing studies. J Affect Disord 2011; 130: 66–74.

Di Martino A, Scheres A, Margulies DS, Kelly AM, Uddin LQ, Shehzad Z, et al. Functional connectivity of human striatum: a resting state FMRI study. Cereb Cortex 2008; 18: 2735–47.

Erk S, Mikschl A, Stier S, Ciaramidaro A, Gapp V, Weber B, et al. Acute and sustained effects of cognitive emotion regulation in major depression. J Neurosci 2010; 30: 15726–34.

Eshel N, Roiser JP. Reward and punishment processing in depression. Biol Psychiatry 2010; 68: 118–24.

Farb NA, Anderson AK, Bloch RT, Segal ZV. Mood-linked responses in medial prefrontal cortex predict relapse in patients with recurrent unipolar depression. Biol Psychiatry 2011; 70: 366–72.

Fox MD, Raichle ME. Spontaneous fluctuations in brain activity observed with functional magnetic resonance imaging. Nat Rev Neurosci 2007; 8: 700–11.

Frodl T, Jager M, Born C, Ritter S, Kraft E, Zetzsche T, et al. Anterior cingulate cortex does not differ between patients with major depression and healthy controls, but relatively large anterior cingulate cortex predicts a good clinical course. Psychiatry Res 2008; 163: 76–83.

Fu CH, Williams SC, Brammer MJ, Suckling J, Kim J, Cleare AJ, et al. Neural responses to happy facial expressions in major depression following antidepressant treatment. Am J Psychiatry 2007; 164: 599–607.

Ginestet CE, Nichols TE, Bullmore ET, Simmons A. Brain network analysis: separating cost from topology using cost-integration. PloS One 2011; 6: e21570.

Greicius MD, Flores BH, Menon V, Glover GH, Solvason HB, Kenna H, et al. Resting-state functional connectivity in major depression: abnormally increased contributions from subgenual cingulate cortex and thalamus. Biol Psychiatry 2007; 62: 429–37.

Hamilton JP, Chen MC, Gotlib IH. Neural systems approaches to understanding major depressive disorder: an intrinsic functional organization perspective. Neurobiol Dis 2013; 52: 4–11.

Hamilton JP, Etkin A, Furman DJ, Lemus MG, Johnson RF, Gotlib IH. Functional neuroimaging of major depressive disorder: a meta-analysis and new integration of base line activation and neural response data. Am J Psychiatry 2012; 169: 693–703.

Hamilton JP, Furman DJ, Chang C, Thomason ME, Dennis E, Gotlib IH. Default-mode and task-positive network activity in major depressive disorder: implications for adaptive and maladaptive rumination. Biol Psychiatry 2011; 70: 327–33.

Hamilton M. A rating scale for depression. J Neurol Neurosurg Psychiatry 1960; 23: 56–62.

Hardeveld F, Spijker J, De Graaf R, Nolen WA, Beekman AT. Prevalence and predictors of recurrence of major depressive disorder in the adult population. Acta Psychiatrica Scandinavica 2010; 122: 184–91.

Heller AS, Johnstone T, Light SN, Peterson MJ, Kolden GG, Kalin NH, et al. Relationships between changes in sustained fronto-striatal connectivity and positive affect in major depression resulting from antidepressant treatment. Am J Psychiatry 2013; 170: 197–206.

Hennings JM, Owashi T, Binder EB, Horstmann S, Menke A, Kloiber S, et al. Clinical characteristics and treatment outcome in a representative sample of depressed inpatients - findings from the Munich Antidepressant Response Signature (MARS) project. J Psychiatric Res 2009; 43: 215–29.

Humphries MD, Gurney K, Prescott TJ. The brainstem reticular formation is a small-world, not scale-free, network. Proc Biol Sci 2006; 273: 503–11.

Jin C, Gao C, Chen C, Ma S, Netra R, Wang Y, et al. A preliminary study of the dysregulation of the resting networks in first-episode medication-naive adolescent depression. Neurosci Lett 2011; 503: 105–9.

Kendler KS, Thornton LM, Gardner CO. Genetic risk, number of previous depressive episodes, and stressful life events in predicting onset of major depression. Am J Psychiatry 2001; 158: 582–6.

Kessler RC, Berglund P, Demler O, Jin R, Koretz D, Merikangas KR, et al. The epidemiology of major depressive disorder: results from the National Comorbidity Survey Replication (NCS-R). JAMA 2003; 289: 3095–105.

Kronmuller KT, Schroder J, Kohler S, Gotz B, Victor D, Unger J, et al. Hippocampal volume in first episode and recurrent depression. Psychiatry Res 2009; 174: 62–6.

Lewis CM, Ng MY, Butler AW, Cohen-Woods S, Uher R, Pirlo K, et al. Genome-wide association study of major recurrent depression in the U.K. population. Am J Psychiatry 2010; 167: 949–57.

Li B, Liu L, Friston KJ, Shen H, Wang L, Zeng LL, et al. A treatment-resistant default mode subnetwork in major depression. Biol Psychiatry 2012; 74: 48–54.

Liljeholm M, O'Doherty JP. Contributions of the striatum to learning, motivation, and performance: an associative account. Trends Cogn Sci 2012; 16: 467–75.

Lu J, Liu H, Zhang M, Wang D, Cao Y, Ma Q, et al. Focal pontine lesions provide evidence that intrinsic functional connectivity reflects polysynaptic anatomical pathways. J Neurosc 2011; 31: 15065–71.

Lui S, Wu Q, Qiu L, Yang X, Kuang W, Chan RC, et al. Resting-state functional connectivity in treatment-resistant depression. Am J Psychiatry 2011; 168: 642–8.

Lynall ME, Bassett DS, Kerwin R, McKenna PJ, Kitzbichler M, Muller U, et al. Functional connectivity and brain networks in schizophrenia. J Neurosci 2010; 30: 9477–87.

MacQueen GM, Campbell S, McEwen BS, Macdonald K, Amano S, Joffe RT, et al. Course of illness, hippocampal function, and hippocampal volume in major depression. Proc Natl Acad Sci USA 2003; 100: 1387–92.

Maia TV, Frank MJ. From reinforcement learning models to psychiatric and neurological disorders. Nat Neurosci 2011; 14: 154–62.

Markov NT, Ercsey-Ravasz M, Lamy C, Ribeiro Gomes AR, Magrou L, Misery P, et al. The role of long-range connections on the specificity of the macaque interareal cortical network. Proc Natl Acad Sci USA 2013; 110: 5187–92.

Moylan S, Maes M, Wray NR, Berk M. The neuroprogressive nature of major depressive disorder: pathways to disease evolution and resistance, and therapeutic implications. Mol Psychiatry 2013; 18: 595–606.

Murphy K, Bodurka J, Bandettini PA. How long to scan? The relationship between fMRI temporal signal to noise ratio and necessary scan duration. Neuroimage 2007; 34: 565–74.

Mwangi B, Ebmeier KP, Matthews K, Steele JD. Multi-centre diagnostic classification of individual structural neuroimaging scans from patients with major depressive disorder. Brain 2012; 135 (Pt 5): 1508–21.

Percival D, Walden A. Wavelet methods for time series analysis. Cambridge, UK: Cambridge University Press; 2000.

Raichle ME. Two views of brain function. Trends Cogn Sci 2010; 14: 180–90.

Robinson OJ, Cools R, Carlisi CO, Sahakian BJ, Drevets WC. Ventral striatum response during reward and punishment reversal learning in unmedicated major depressive disorder. Am J Psychiatry 2012; 169: 152–9.

Robinson OJ, Sahakian BJ. Recurrence in major depressive disorder: a neurocognitive perspective. Psychol Med 2008; 38: 315–8.

Rubinov M, Sporns O. Complex network measures of brain connectivity: uses and interpretations. Neuroimage 2010; 52: 1059–69.

Rubinov M, Sporns O. Weight-conserving characterization of complex functional brain networks. Neuroimage 2011; 56: 2068–79.

Savitz J, Drevets WC. Bipolar and major depressive disorder: neuroimaging the developmental-degenerative divide. Neurosci Biobehav Rev 2009; 33: 699–771.

Seeley WW, Menon V, Schatzberg AF, Keller J, Glover GH, Kenna H, et al. Dissociable intrinsic connectivity networks for salience processing and executive control. J Neurosci 2007; 27: 2349–56.

Serrano MA, Boguna M, Vespignani A. Extracting the multiscale backbone of complex weighted networks. Proc Natl Acad Sci USA 2009; 106: 6483–8.

Sheline YI, Price JL, Yan Z, Mintun MA. Resting-state functional MRI in depression unmasks increased connectivity between networks via the dorsal nexus. Proc Natl Acad Sci USA 2010; 107: 11020–5.

Sheline YI, Sanghavi M, Mintun MA, Gado MH. Depression duration but not age predicts hippocampal volume loss in medically healthy women with recurrent major depression. J Neurosci 1999; 19: 5034–43.

Spitzer RL, Williams JB, Gibbon M, First MB. The Structured Clinical Interview for DSM-III-R (SCID). I: history, rationale, and description. Arch Gen Psychiatry 1992; 49: 624–9.

Tao H, Guo S, Ge T, Kendrick KM, Xue Z, Liu Z, et al. Depression uncouples brain hate circuit. Mol Psychiatry 2013; 18: 101–11.

Valente TW, Coronges K, Lakon C, Costenbader E. How correlated are network centrality measures? Connect (Tor) 2008; 28: 16–26.

van den Heuvel MP, Kahn RS, Goni J, Sporns O. High-cost, high-capacity backbone for global brain communication. Proc Natl Acad Sci USA 2012; 109: 11372–7.

Van Dijk KR, Sabuncu MR, Buckner RL. The influence of head motion on intrinsic functional connectivity MRI. Neuroimage 2012; 59: 431–8.

Wang J, Wang L, Zang Y, Yang H, Tang H, Gong Q, et al. Parcellation-dependent small-world brain functional networks: a resting-state fMRI study. Hum Brain Mapp 2009; 30: 1511–23.

Wang L, Dai Z, Peng H, Tan L, Ding Y, He Z, et al. Overlapping and segregated resting-state functional connectivity in patients with major depressive disorder with and without childhood neglect. Hum Brain Mapp 2013, Advance Access published on February 13, 2013, doi: 10.1002/hbm.22241.

Whitfield-Gabrieli S, Ford JM. Default mode network activity and connectivity in psychopathology. Annu Rev Clin Psychol 2012; 8: 49–76.

Zeng LL, Shen H, Liu L, Wang L, Li B, Fang P, et al. Identifying major depression using whole-brain functional connectivity: a multivariate pattern analysis. Brain 2012; 135 (Pt 5): 1498–507.

Zhang J, Wang J, Wu Q, Kuang W, Huang X, He Y, et al. Disrupted brain connectivity networks in drug-naive, first-episode major depressive disorder. Biol Psychiatry 2011; 70: 334–42.

Zuo XN, Ehmke R, Mennes M, Imperati D, Castellanos FX, Sporns O, et al. Network centrality in the human functional connectome. Cereb Cortex 2012; 22: 1862–75.

Cerebral Cortex December 2015;25:4678–4688
doi:10.1093/cercor/bhu151
Advance Access publication July 4, 2014

Disrupted Intrinsic Networks Link Amyloid-β Pathology and Impaired Cognition in Prodromal Alzheimer's Disease

Kathrin Koch[1,5,†], Nicholas E. Myers[1,5,6,†], Jens Göttler[1,5,†], Lorenzo Pasquini[1,5], Timo Grimmer[2], Stefan Förster[3,5], Andrei Manoliu[1,2,5], Julia Neitzel[1,5,7], Alexander Kurz[2], Hans Förstl[2], Valentin Riedl[1,3,5], Afra M. Wohlschläger[1,4,5], Alexander Drzezga[8,†] and Christian Sorg[1,2,3,5,†]

[1]Department of Neuroradiology, [2]Department of Psychiatry, [3]Department of Nuclear Medicine, [4]Department of Neurology, [5]TUM-Neuroimaging Center of Klinikum rechts der Isar, Technische Universität München (TUM), 81675 Munich, Germany, [6]Department of Experimental Psychology, Oxford University, Oxford OX1 3UD, UK, [7]Graduate School of Systemic Neurosciences (GSN), Ludwig-Maximilians-Universität, Biocenter, 82152 Munich, Germany and [8]Klinik und Poliklinik für Nuklearmedizin, 50937 Cologne, Germany

Address correspondence to Kathrin Koch, Department of Neuroradiology, Technische Universität München, Ismaninger Strasse 22, 81675 Munich, Germany. Email: kathrin.koch@tum.de
[†]Kathrin Koch, Nicholas E. Myers, Jens Göttler, Alexander Drzezga, and Christian Sorg equally contributed to the study.

Amyloid-β pathology (Aβ) and impaired cognition characterize Alzheimer's disease (AD); however, neural mechanisms that link Aβ-pathology with impaired cognition are incompletely understood. Large-scale intrinsic connectivity networks (ICNs) are potential candidates for this link: Aβ-pathology affects specific networks in early AD, these networks show disrupted connectivity, and they process specific cognitive functions impaired in AD, like memory or attention. We hypothesized that, in AD, regional changes of ICNs, which persist across rest- and cognitive task-states, might link Aβ-pathology with impaired cognition via impaired intrinsic connectivity. Pittsburgh compound B (PiB)-positron emission tomography reflecting in vivo Aβ-pathology, resting-state fMRI, task-fMRI, and cognitive testing were used in patients with prodromal AD and healthy controls. In patients, default mode network's (DMN) functional connectivity (FC) was reduced in the medial parietal cortex during rest relative to healthy controls, relatively increased in the same region during an attention-demanding task, and associated with patients' cognitive impairment. Local PiB-uptake correlated negatively with DMN connectivity. Importantly, corresponding results were found for the right lateral parietal region of an attentional network. Finally, structural equation modeling confirmed a direct influence of DMN resting-state FC on the association between Aβ-pathology and cognitive impairment. Data provide evidence that disrupted intrinsic network connectivity links Aβ-pathology with cognitive impairment in early AD.

Keywords: amyloid plaques, impaired cognition, intrinsic connectivity networks, PiB-PET, prodromal Alzheimer's disease, resting-state fMRI, task-fMRI

Introduction

Alzheimer's disease (AD) is the most common cause of dementia, accounting for about 60% of cases (Ferri et al. 2005). AD is characterized by progressive cell loss and deposition of neurofibrillary tangles and amyloid-β (Aβ) plaques (AP; Braak et al. 1993; Hansson et al. 2006). The Aβ hypothesis of AD suggests that abnormal cleavage of Aβ-precursor protein results in the imbalanced production and clearance of Aβ-peptides, including peptide accumulation and AP formation. Aβ-pathology, in turn, triggers neural dysfunction and degeneration (i.e., tangle formation and cell loss), finally resulting in patients' cognitive impairment (Selkoe 2002). This model raises the question of which neural mechanisms are involved in the translation of Aβ-pathology into cognitive impairments.

Intrinsic connectivity networks (ICNs) are characterized by synchronous ongoing brain activity at infra-slow frequency of about 0.1 Hz (Fox and Raichle 2007). They are functional networks, that is, the same regions, whose ongoing activity is coherent in non-task-states, largely co-activate during task-states, suggesting that intrinsic networks implement specific aspects of cognition and behavior (Smith et al. 2009; Laird et al. 2011). One explanation for this functional aspect of intrinsic networks is that functional connectivity (FC) at rest reflects the history of correlated activity changes during goal-directed behavior (Lewis et al. 2009; Berkes et al. 2011; Riedl et al. 2011).

ICNs are selectively disrupted in AD and in mild cognitive impairment (MCI), a high-risk state for AD (Gauthier et al. 2006), with the earliest disruptions occurring in default mode and attention networks (DMN and ATN; Greicius et al. 2004; Sorg et al. 2007, 2009; Agosta et al. 2012). While the DMN, which covers medial fronto-parietal areas, activates when attention is not focused on the outside world and deactivates during world-focused attention (Buckner et al. 2008), ATNs, which cover lateral fronto-parietal areas, are more active during world-focused attention and goal-directed behavior (Corbetta and Shulman 2002). We use the term ATN in line with Allen et al. (2011) referring to a couple of networks such as the dorsal or ventral ATN or lateralized central executive networks, all being located in frontal and parietal lobes (Allen et al. 2011). Aberrant resting-state FC of both DMN and ATNs overlaps and is related with Aβ-pathology in older persons with and without cognitive symptoms, suggesting a significant relationship between Aβ-pathology and network impairments (Hedden et al. 2009; Sheline et al. 2010; Drzezga et al. 2011; Mormino et al. 2011; Myers et al. 2014). Given both the cognitive relevance of intrinsic networks and the correspondence between aberrant intrinsic connectivity and Aβ-pathology, there is reason to assume that aberrant ICN FC might be a relevant mechanism linking Aβ-pathology with impaired cognition in AD.

Initial evidence for this assumption has been found for the DMN in patients and asymptomatic older adults, showing an association of increased Aβ with higher DMN activity during a memory task (Sperling et al. 2009). However, it is still unclear whether ICNs beyond the DMN show a similar correspondence between Aβ-pathology, aberrant intrinsic FC, impaired task-related activity, and impaired behavior in a task that recruits that

network. Considering that the DMN and ATNs cover regions with aberrant task-evoked activation and FC in AD dementia and MCI for a huge range of attention-demanding tasks (e.g., Dannhauser et al. 2005; Rombouts et al. 2005; Celone et al. 2006; Petrella et al. 2007; Sperling et al. 2010; Neufang et al. 2011; Mandal 2012), we hypothesized, first, spatially consistent changes in FC across both attention-demanding task- and rest-states in DMN and ATNs in AD. Regions showing such across task and rest consistent changes should be regions that are most strongly affected by the disease, and therefore potential candidates for proposed linking mechanisms via aberrant intrinsic FC. Therefore, we suggested, secondly, that these regions would link impaired network FC, Aβ-pathology, and impaired cognition in AD.

Materials and Methods

Overview

To address the study's hypotheses, we assessed patients with prodromal AD (pAD; i.e., with MCI and biological signs of AD) and healthy older adults by resting-state functional MRI (rs-fMRI) to identify ICNs, task-fMRI (i.e., an attention-demanding task with different difficulty levels) to reveal ICN changes regionally consistent for attention-relevant task- and rest-states, positron emission tomography (PET) imaging using the tracer [11C]-Pittsburgh compound B (PiB-PET) to estimate Aβ-pathology in vivo via PiB-uptake, and neuropsychological assessment to estimate general cognitive performance. Independent component analysis (ICA) of fMRI data was used to quantify the networks' FC pattern during rest and task as a surrogate measure of ICN connectivity. ICA decomposes fMRI data into statistically independent components with each component consisting of both a spatial z-map, which represents network's FC pattern across space, and a time course, which represents network's activity across time. Z-maps of rest- and task-states were the main outcome measures of the study representing FC, and were related to each other, to regional PiB-uptake, and to cognitive performance scores via pairwise correlation and structural equation modeling (SEM). The study's hypotheses were specified as follows: (i) Aberrant FC is spatially consistent across states of rest and the cognitive task in DMN and ATNs. (ii) Resting-state FC of such overlapping regions relates with both PiB-uptake and impaired cognition. Specifically, we expected resting-state FC to mediate the association between PiB-uptake and cognition.

Participants

Assessment

Twenty-four patients (10 females, age range 50–83 years) diagnosed with pAD and 16 healthy controls (9 females, age range 57–75 years) participated in the study (Table 1). All participants provided informed consent in accordance with the Human Research Committee guidelines of the Klinikum Rechts der Isar, Technische Universität, München. Patients were recruited from the Memory Clinic of the Department of Psychiatry, controls by word-of-mouth advertising. Examination of every participant included medical history, neurological examination, informant interview (Clinical Dementia Rating, CDR; Morris 1993), neuropsychological assessment (Consortium to establish a registry for AD, CERAD battery; Morris et al. 1989), structural MRI, and PiB-PET.

Table 1
Demographic and clinical–neuropsychological data

	Groups	
	Patients	Controls
N	24	16
Age	68.2 (8.4)	64.8 (5.4)
Gender (F/M)	10/14	9/7
CDR	0.5 (0)	0 (0)*
CDR-SB	1.6 (0.5)	0 (0)*
CERAD-total	66.3 (10.8)	88.1 (6.8)*

CDR: Clinical Dementia Rating; CDR-SB: CDR sum-of-the-box; CERAD: battery of the Consortium to Establish a Registry for AD; CERAD-total: summary of CERAD subtests; group comparisons: χ^2 (gender), two-sample *t*-test (age, CDR, CDR-SB, and CERAD-total).
*Significant group difference at $P < 0.05$.

Definition of pAD

pAD has been defined by the coincidence of both MCI and the presence of at least 1 of 5 supportive biological signs for AD such as medial temporal lobe atrophy or significant PiB-load (Dubois et al. 2007). Following this definition, we focused on the presence of MCI and significant PiB-uptake. MCI criteria include reported and neuropsychologically assessed cognitive impairments, largely intact activities of daily living, and excluded dementia (Gauthier et al. 2006). For significant PiB-uptake, we used a cut-off for "high" or "low" standardized uptake value (SUV) ratios of 1.15, consistent with cut-off values used in previous PiB-PET studies (Drzezga et al. 2011). Patients with high PiB binding (i.e., SUV ratio ≥1.15) were classified as PiB-positive and those with SUV ratio <1.15 were classified as PiB-negative (i.e., PiB-uptake SUV <1.15 was an inclusion criterion for healthy controls). Standardized SUV is measured for a pre-established large cortical volume of interest including lateral prefrontal, parietal, and temporal areas and the retrosplenial cortex, which are described in more detail below (see PET methods) and in Supplementary Material (Supplementary Fig. 1) (Hedden et al. 2009; Drzezga et al. 2011). One should note that our definition of pAD goes along with recent recommendations of a workgroup charged by the National Institute on Aging and the Alzheimer's Association (Albert et al. 2011), which suggested to differentiate between MCI (i.e., the presence of core clinical criteria for MCI, based on the characteristics of the clinical syndrome, and an examination of potential etiologic causes for the cognitive decline), MCI due to AD with an intermediate likelihood (i.e., the presence of core clinical criteria for MCI, either a positive biomarker reflecting Aβ deposition with an untested biomarker of neuronal injury, or a positive biomarker reflecting neuronal injury with an untested biomarker of Aβ), MCI due to AD with a high likelihood (i.e., the presence of core clinical criteria for MCI, positive biomarkers for both Aβ and neuronal injury), and MCI unlikely due to AD (i.e., negative biomarkers for both Aβ and neuronal injury).

In- and Exclusion Criteria

Patients of our study met criteria for MCI and demonstrated significant cortical PiB-uptake (PiB-positive). Healthy controls met criteria of being both without cognitive symptoms (i.e., CDR 0 and all CERAD subscores within 1 SD of age- and gender-matched performance) and PiB-negative. Exclusion criteria for entry into the study were other neurological, psychiatric, or systemic diseases (e.g., stroke, depression, and alcoholism) or clinically remarkable structural MRI (e.g., stroke lesions) potentially related to cognitive impairment. Fifteen patients/8 healthy controls were treated for hypertension (beta-blockers, ACE inhibitors, and calcium channel blockers), and 7/5 for hypercholesterolemia (statins). Two patients had diabetes mellitus, 4 received antidepressant medication (Mirtazapine and Citalopram), and no patient received cholinesterase inhibitors.

Multimodal Imaging Assessment

All participants underwent both MRI and PiB-PET imaging sessions. MRI session included structural MRI, rs-fMRI, and task-fMRI. PET and MRI sessions were conducted within 3.7 (±2.5) months for patients, and within 8 (±3.1) months for healthy controls.

Functional MRI Analysis

Resting-State Paradigm

During rs-fMRI (10 min), participants were instructed to keep their eyes closed and not to fall asleep. We verified that participants stayed awake by interrogating via intercom immediately after scanning.

Behavioral Paradigm

During task-fMRI, participants underwent an attention-demanding task with different difficulty levels (and therefore varying attention demands). We employed a visuo-motor dual-task paradigm with the aim of taxing central executive processing via orthogonal task demands (for detailed task description, please refer to Supplementary Material). By using a full factorial design with independently varying levels of difficulty in the visual and motor domains, we aimed to parametrically modulate task difficulty in a design that was still straightforward enough for patients to follow and perform at above-chance levels, even in the most difficult condition (in contrast, a more conventional task, such as typical working memory task with increasing load, could easily have brought patients to chance performance in the difficult conditions). We analyzed accuracy (ACCR) and reaction time (RT) data using a two-way mixed-effects ANOVA, with factors group (2 levels) and task difficulty (4 levels). The current analysis aims at the relationship between networks' FC during both being at rest and at an attention-demanding task state.

Data Acquisition

fMRI data were collected using a gradient-echo planar imaging sequence (echo time = 35 ms, repetition time = 2000 ms, flip angle = 82°, field of view = 220 × 220 mm², matrix = 80 × 80, 32 slices, slice thickness = 4 mm, and 0 mm interslice gap).

Data Preprocessing

For each participant, the first 3 functional scans of each fMRI session were discarded due to tissue magnetization effects. SPM5 (Wellcome Department of Cognitive Neurology, London, UK) was used for motion correction, spatial normalization into the Montreal Neurological Institute (MNI) space, and spatial smoothing with an 8 × 8 × 8 mm Gaussian kernel. To ensure data quality, particularly concerning motion-induced artifacts, point-to-point head motion was estimated for each subject (Power et al. 2012; Van Dijk et al. 2012). Excessive head motion (cumulative translation or rotation >3 mm or 3° and mean point-to-point translation or rotation >0.15 mm or 0.1°) was applied as an exclusion criterion. For rs-fMRI, none of the participants had to be excluded. For task-fMRI, 1 healthy control and 7 patients had to be removed from the analysis due to excessive movement ($n = 5$) or technical problems ($n = 3$), respectively. For both rs- and task-fMRI data, two-sample *t*-tests between groups yielded no significant results regarding translational and rotational movements of any direction ($P > 0.05$).

ICA and Measuring FC

Preprocessed data were decomposed into spatially independent components reflecting ICNs in a group-ICA framework (Calhoun et al. 2001), which is implemented in the GIFT software (http://icatb.sourceforge.net). Dimensionality estimation was performed for each individual dataset using minimum description length, resulting in a mean estimate of 35 (rs-fMRI)/59 (task-fMRI) components. For rs- and task-fMRI, data of controls and patients were concatenated and reduced by two-step principal component analysis, followed by independent component estimation with the infomax algorithm. This resulted in 2 sets of average group components for both fMRI runs, which were subsequently back-reconstructed into single-subject space. For each subject and fMRI run, each component included both a spatial map, which reflected that component's z-scored FC pattern across space, and a time course, which reflected the component's activity across time. Only spatial maps were analyzed further.

According to previous findings of aberrant medial and lateral fronto-parietal ICNs in early stages of AD (Sorg et al. 2007, 2009; Neufang et al. 2011; Agosta et al. 2012), the DMN and attentional ICNs were of interest (Allen et al. 2011). To automatically select ICNs-of-interest, we applied multiple spatial regression analyses of the 35 (rs-fMRI)/59 (task-fMRI) independent components on masks derived from a previous study (Allen et al. 2011): The anterior and posterior DMN (aDMN IC 25 and pDMN IC 53 of Allen et al. 2011), ATNs (r(ight) ATN IC 60, l (eft) ATN IC 34, and d(orsal) ATN IC 72), salience network (IC 55 of Allen et al. 2011), and the primary auditory network (IC 17 of Allen et al. 2011) as a control for the specificity of effects. Masks were generated with the WFU-Pickatlas (http://www.fmri.wfubmc.edu/). In order to evaluate consistency of selected ICNs across rest and task conditions, we created templates from identified resting-state networks in a whole group approach [$P < 0.05$, family-wise error (FWE) cluster-corrected], related these masks spatially with the 59 components of the task ICA analysis again by spatial regression as implemented in the gift toolbox, and—to foreshadow results—found consistent ICNs with respect to the above-mentioned procedure (i.e., the IC selection procedure based on templates of Allen et al. identified consistent ICNs across rest and task; for correlation coefficients see Supplementary Table 4).

Across-Subject Statistical Analysis

To statistically evaluate spatial maps of selected components, we calculated voxel-wise one-sample *t*-tests on participants' spatial z-maps for each condition and group, using SPM5 ($P < 0.05$, FWE cluster-corrected). To analyze group differences, corresponding spatial maps were entered into two-sample *t*-tests ($P < 0.05$, FWE cluster-corrected, with network volumes as covariates of no interest; for details of network volume definition see below and Supplementary material "voxel-based morphometry of structural MRI"); these two-sample *t*-tests were restricted to appropriate one-sample *t*-test masks across all participants ($P < 0.01$, uncorrected). For volumes and networks defined by overlapping group different FC for rest- and task-states (i.e., in the pDMN and rATN, see Supplementary Table 1 and Fig. 2), z-maps were averaged for each subject and condition, and compared across conditions via paired *t*-tests for each group ($P < 0.05$; restricted to subjects with both rest- and task-fMRI data).

Control Analysis for Atrophy

To control for the influence of potential atrophy on FC of networks, structural changes were estimated by the use of voxel-based morphometry (VBM) of structural MRI data, which are described in detail in Supplemental Material and elsewhere (Myers et al. 2014). In brief, by the use of VBM, images were bias-corrected, tissue classified, linearly (i.e., 12-parameter affine registration) and non-linearly (i.e., warping regularization) registered, and smoothed with a Gaussian kernel of 8 mm full-width at half maximum. Voxel-wise gray matter differences between patients and controls were examined using two-sample *t*-tests ($P < 0.05$, FWE cluster-corrected), and related with spatial patterns of aberrant FC via visual inspection. Moreover, gray matter values were extracted from those networks showing FC group differences consistent across rest and task conditions, and entered as covariates into resting-state FC group comparisons.

PiB-PET Data Analysis

To evaluate the relationship between resting-state FC and PiB-uptake, regional PiB-uptake was estimated from PiB-PET data, following previous protocols (Mosconi et al. 2008) and described in detail in Supplemental Material. In brief, after image reconstruction, correction of dead time, scatter and attenuation, SPM5 was used for image realignment, transformation into the standard stereotactic MNI space, smoothing, and statistical analysis (two-sample *t*-test, $P < 0.001$, cluster extent $k = 100$).

Relationship among Intrinsic Networks, PiB-Uptake, and Cognition

Regression Analyses

As we found spatially consistent group differences during rest and task for the pDMN and rATN in the medial and lateral posterior parietal cortex (PPC), respectively (Supplementary Table 1 and Fig. 2), the following analyses focused on these regions. Since spatial overlap of altered rest- and task-FC was small at a conservative threshold (i.e., $P < 0.05$, FWE cluster-corrected; Supplementary Table 1) but enlarged strongly at a more liberal threshold ($P < 0.05$; Fig. 2), data suggested that consistently changed FC might be underestimated (for example, ICA of across groups merged fMRI data may underestimate group differences in the FC of networks). Therefore, we decided, first, to use more liberal thresholds for unimodal group comparisons with the effect of an enlarged volume of interest of potential candidates to link Aβ-pathology with impaired cognition via intrinsic FC and, then, to combine such

enlarged volume with a complementary voxel-wise multiple regression approach to relate resting-state FC with impaired cognition/PiB-uptake in patients. The combination of volume-of-interest enlargement by liberal "entrance" thresholds and subsequent voxel-wise regression analysis is complementary, since voxel-wise approaches are sensitive for intraregional variability within enlarged volumes of interest without loss of statistical rigor. In a nutshell, our procedure increased the number of potential candidates, whose resting-state FC may relate with both Aβ-pathology and impaired cognition.

More specifically, to define an overlap region that includes all potential voxels of aberrant rest- and task-FC at high probability, we chose a liberal threshold of $P < 0.2$ for unimodal comparisons by minimizing the amount of Type II error, and defined the overlap volume by the use of MARSBAR (Brett et al. 2002). Based on this volume, voxel-wise regression analyses linking patients' rest-FC with local PiB-uptake/cognitive scores were performed. For voxel-wise regression analysis, we followed Mormino et al. (2011), who used such an approach to relate FC and PiB-uptake. For regression analyses, we used a threshold of $P < 0.05$ uncorrected with a cluster extent threshold of $k = 40$. This liberal significance threshold was chosen due to 3 reasons: (1) We tested a regionally specific hypothesis (i.e., for consistently changed FC, patients' reduced resting-state FC is related with both increased PiB-uptake and reduced cognitive performance) instead of exploratory whole-brain analysis. (2) For PiB-uptake in posterior parietal areas of pAD, liberal thresholds have to be applied as patients may show strong ceiling effects in the PiB analyses (i.e., PiB-uptake values were very high with a small intersubject variance; Engler et al. 2006; Grimmer et al. 2009). (3) The chosen threshold is similar to that of Mormino et al. (2011).

To analyze the relationship between pDMN/rATN FC at rest and local PiB-uptake, PiB-uptake scores were averaged for each overlap-region of interest (ROI). Subsequently, patients' averaged PiB-uptake scores were treated as a continuous variable and regressed voxel-wise against pDMN/rATN FC maps in SPM.

To analyze the relationship between pDMN/rATN FC and cognitive performance, we performed analogous regression analyses of pDMN/rATN spatial maps (as just described), but with regressors reflecting cognitive performance instead of PiB-uptake. To ensure consistent results, we used 2 different scores of cognitive performance. First, we used the accuracy results of the task-fMRI paradigm. More specifically, we used the error rate difference between the easiest and the most difficult conditions (ACCR 4 − ACCR 1) as a regressor to account for variance predictive of success in our particular task. Secondly, we used CERAD total scores as a regressor, reflecting general cognitive impairment (Karrasch et al. 2005).

To control for the network specificity of the reported effects, analogous analyses as described above were performed for the auditory network. To create a control-ROI correspondent to the overlap-ROI, we defined the control-ROI center by the peak of the auditory network's group difference for the resting-state condition; as a ROI radius, we defined the minimal length that enabled the spherical control ROI volume to cover given overlap-ROI volumes.

SEM Analysis

Finally, beyond pairwise voxel-wise regression analyses linking between levels of Aβ-pathology, FC, and cognition, we also investigated within one integrated analytic approach whether aberrant ICN connectivity mediates or moderates the effects of Aβ-pathology on cognition in AD. Therefore, we performed ROI-based SEM for regional PiB-uptake, intrinsic network z-maps, and cognitive scores. We extracted PiB-uptake and resting-state FC values from those regions within rATN/pDMN overlap-ROIs that showed an altered connectivity in patients compared with healthy participants (as described in Supplementary Table 1 based on two-sample *t*-tests at significance threshold $P < 0.05$, FWE cluster-corrected).

We specified 2 path models, a moderator and a mediator model. A mediator model typically consists of one (or more) independent (or exogenous) variable(s), a mediator variable, and a dependent variable. Both the independent and the mediator variables are assumed to influence the dependent variable. The independent variable influences the dependent variable both directly and indirectly, that is, through its effect on the mediating variable. Accordingly, in the present study, Aβ-pathology (i.e., PiB-uptake) constitutes the independent variable, cognitive performance (i.e., ACCR4 − ACCR1 and CERAD) the dependent variable, and FC the mediating variable. Thus, we would assume that the association between PiB-uptake and cognitive performance is mediated through the effect of PiB-uptake on FC (i.e., indirect effect).

A moderator model typically consists of one (or more) independent variable(s), a moderator variable, and a dependent variable. The major difference to the mediator model is that the moderator variable is assumed to directly influence the association between the independent and the dependent variable. Again, in the context of the present study, Aβ-pathology (i.e., PiB-uptake) constitutes the independent variable and cognitive performance (i.e., ACCR4 − ACCR1 and CERAD) the dependent variable. Assuming that FC moderates the association between Aβ-pathology and cognitive performance, we generated the moderator variable by calculating the element-wise product of PiB-uptake and FC (Baron and Kenny 1986; Schlösser et al. 2007).

SEM was performed using the program Amos 22.0.0 (http://amosdevelopment.com), applying a maximum-likelihood algorithm for estimating path coefficients. We used bootstrapping procedures which make no a priori assumptions about the distribution of the paths. The null hypothesis was tested by determining whether zero was within the 95% bias-corrected confidence intervals (CIs). The goodness-of-fit index (GFI) was used to assess the goodness-of-fit of the models.

Results

Impaired Cognition and Increased PiB-Uptake in Patients

Patients had significantly reduced CERAD total scores compared with healthy older adults (two-sample *t*-test, $P < 0.001$; Table 1). Furthermore, for the attention-demanding task of increasing difficulty during task-fMRI, two-way repeated-measures ANOVAs of accuracy ACCR and RT, with factors group (2 levels) and task difficulty (4 levels), revealed significant effects of group (ACCR $F_{1,30} = 25.4$, $P < 0.001$; RT $F_{1,30} = 16.2$, $P < 0.001$), of task difficulty (ACCR $F_{3,90} = 30.7$, $P < 0.001$; RT $F_{3,90} = 93.7$, $P < 0.001$), and a significant interaction (ACCR $F_{3,90} = 23.3$, $P < 0.001$; RT $F_{3,90} = 10.7$, $P < 0.001$). Post hoc *t*-tests revealed selective impairments of patients for the more difficult conditions, both in terms of accuracy (independent samples *t*-tests, $t_{30} = 5.51$, $P < 0.001$; $t_{30} = 0.86$, $P = 0.39$, for ACCR in the most difficult and the easiest conditions, respectively) and RTs ($t_{30} = -3.99$, $P < 0.001$; $t_{30} = -1.91$, $P = 0.07$, for RT in the most difficult and the easiest conditions, respectively; Supplementary Results and Supplementary Fig. 3 for mean accuracies and reaction times).

Patients had increased cortical PiB-uptake within the frontal, parietal, and temporal lobes compared with healthy older adults (two-sample *t*-test, $P < 0.001$ uncorrected and $k = 100$; Fig. 1*A*). The pattern of distribution corresponded well to typical findings previously described in AD (e.g., Drzezga et al. 2011).

Patients had decreased gray matter volume mainly in the temporal lobe, the anterior cingulate, and the left hippocampus (two-sample *t*-test, $P < 0.05$, FWE cluster-corrected, Supplementary Table 2 and Supplementary Fig. 4).

Posterior DMN and Right ATN FC During Rest and Task Is Consistently Disrupted in the Medial and Lateral Posterior Parietal Cortex

ICA of rest- and task-fMRI data revealed for each group spatio-temporal patterns of FC that were correspondent with the

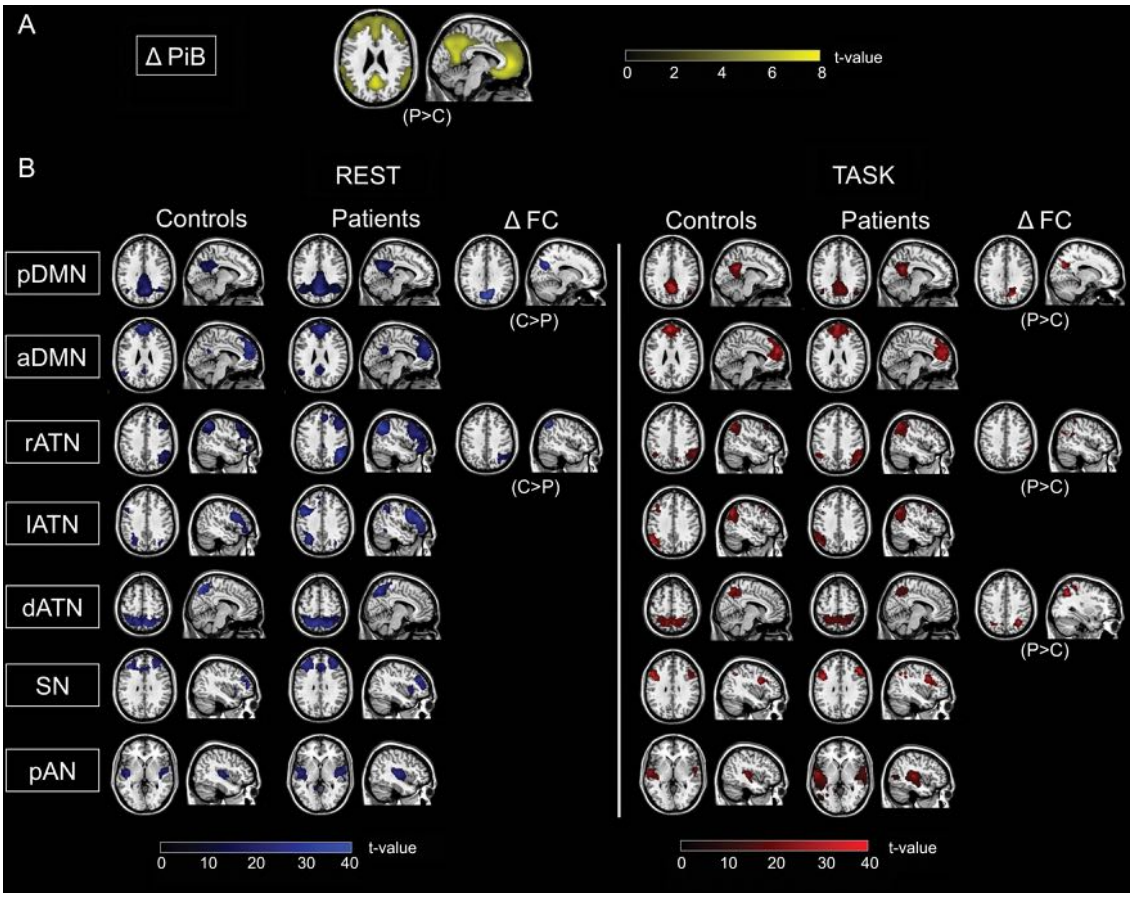

Figure 1. Multimodal imaging of patients with pAD and controls. (*A*) PiB-PET: Group difference in PiB-PET (ΔPiB) between healthy controls and patients is shown by statistical parametric map (SPM) of a two-sample *t*-test, $P < 0.001$ uncorrected, cluster extent $k = 100$; ΔPiB-uptake pattern superimposed on a single-subject high-resolution T_1 image. (*B*) Resting-state and task-fMRI: Participants' resting-state and task-fMRI data, respectively, were decomposed by ICA resulting in individual spatial maps that reflect the spatial patterns of ICNs. Columns 1–4 and 7–10: Spatial connectivity patterns of ICNs during both rest and task for patients and controls (SPMs of one-sample *t*-tests for each ICN of controls and patients; $P < 0.05$ FWE corrected at cluster level). Columns 5, 6, 11, and 12: SPMs demonstrating increased and decreased FC in patients (two-sided two-sample *t*-tests; $P < 0.05$, FWE cluster level, for visual demonstration $P < 0.05$, $k = 10$). All SPMs are projected onto a single-subject anatomical T_1-weighted image. C: healthy controls; P: patients; FC: functional connectivity; DMN: default mode network; p: posterior; a: anterior; ATN: attention network; r: right; l: left; d: dorsal; SN: salience network; pAN: primary auditory network.

posterior and anterior DMN, right, left, and dorsal ATN, salience network, and primary auditory network (Fig. 1*B*; Supplementary Table 3; one-sample *t*-test, $P < 0.05$, FWE cluster-corrected). ICNs were spatially consistent across groups (Fig. 1*B*), across tasks (Supplementary Table 4), and matched previous results (Damoiseaux et al. 2006; Sorg et al. 2007; Smith et al. 2009; Allen et al. 2011).

For the rest condition, patients had lower FC in the precuneus of the pDMN and in the inferior parietal lobule of the rATN (Fig. 1*B*; Supplementary Table 3; two-sample *t*-test, $P < 0.05$, FWE cluster-corrected). For the task condition, patients had increased FC in the precuneus of the pDMN, in the inferior parietal lobule of the rATN, and in the superior parietal cortex of the dorsal ATN (Fig. 1*B*; Supplementary Table 3; two-sample *t*-test, $P < 0.05$, FWE cluster-corrected). After correcting group differences for brain atrophy (i.e., gray matter volume), the effects in the pDMN remained significant both for the rest ($x = 6$, $y = -66$, $z = 34$, $k = 121$, $T = 4.67$, $P < 0.05$, FWE cluster-corrected) and the task condition ($x = 12$, $y = -66$, $z = 28$, $k = 83$, $T = 4.42$, $P < 0.05$, FWE cluster-corrected), while the effects in the rATN were no longer significant.

Critically, when comparing group differences for rest and task, we found overlap (i.e., aberrant FC common to both conditions) for the DMN in the precuneus (Fig. 2*A* and Supplementary Table 1) and for the rATN in the inferior parietal lobule (Fig. 2*B* and Supplementary Table 1). For such overlapping group different rest- and task-FC of the pDMN and rATN, we found lower averaged connectivity in patients and controls during rest than during task in the rATN ($P < 0.05$, Fig. 2*B*), and only for controls increased connectivity during rest than during task in the pDMN ($P < 0.05$, Fig. 2*A*).

Lower pDMN/rATN FC at Rest Correlates with Cognitive Impairment

Voxel-wise regression analyses demonstrated for the medial and lateral PPC that patients' lower pDMN/rATN FC at rest is positively correlated with patients' reduced accuracy (ACCR 4 − ACCR 1) of task performance (Fig. 3*A*,*B*; Supplementary Table 5; $P < 0.05$, uncorrected, $k = 40$). Analogous regression analyses demonstrated for the same regions that patients' decreased pDMN/rATN FC at rest is positively correlated with

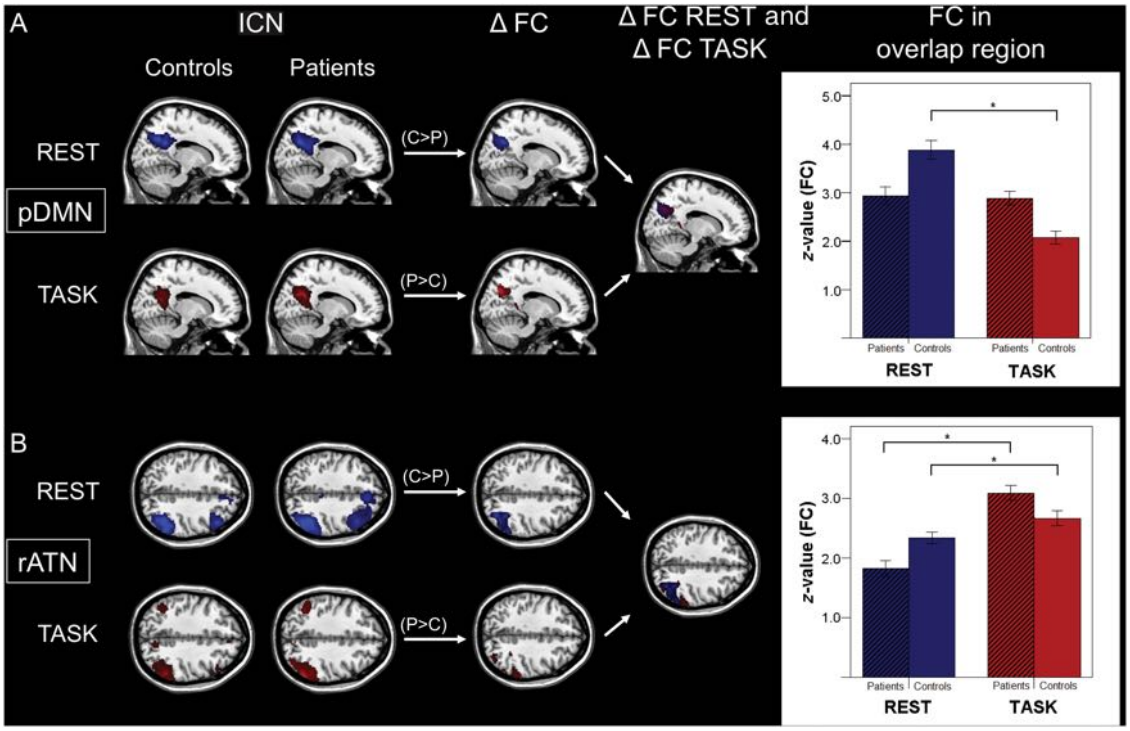

Figure 2. Spatially consistent FC changes of pDMN and rATN across rest and task in patients. Columns 1 and 2: ICNs characterized by spatial patterns of FC during rest (lines 1 and 3) and task (lines 2 and 4) concerning the pDMN (*A*) and rATN (*B*) (SPMs as in Fig. 1). Columns 3 and 4: Results of the ICN group comparisons for FC maps between patients and controls (ΔFC) for rest and task condition as well as corresponding spatial overlaps of group differences (ΔFC Rest and ΔFC Task) [SPMs with increased (P > C) and decreased (P < C) FC in patients as in Figure 1]. Right side: Bar plots representing averaged FC values for overlapping group differences for each group, condition, and ICN. Paired *t*-tests revealed FC differences across conditions ($P < 0.05$, * significant result, pDMN $T = 0.9$ (patients)/7.7 (controls); rATN $T = -7.8/-2.1$).

patients' general cognitive impairment reflected by CERAD total scores (Fig. 3*A*,*B*; Supplementary Table 5). Analogous analyses of the auditory network did not show any significant result.

Increased Local PiB-Uptake Correlates Negatively with pDMN/rATN FC at Rest

Increased PiB-uptake of patients overlapped with maps of lower FC at rest for the pDMN and rATN in the medial and lateral PPC (Fig. 4*A*,*B*). Voxel-wise regression analyses demonstrated for the medial and lateral PPC that patients' local PiB-uptake is negatively correlated with pDMN/rATN FC at rest (Fig. 4*A*,*B*; Supplementary Table 5; $P < 0.05$, uncorrected, $k = 40$). An analogous analysis of the auditory network did not show a significant result.

pDMN FC Moderates the Effects of Aβ-Pathology on Cognition

SEM revealed no significant mediating effects for pDMN and rATN with respect to Aβ-pathology and cognition. Results of the moderator analysis showed a significant negative association between pDMN PiB-uptake and cognitive (i.e., ACCR4 − ACCR1) performance ($\beta = -0.86$, $P < 0.001$) and a trend significance in terms of a positive association between pDMN FC and cognitive performance ($\beta = 0.28$, $P < 0.09$). The moderating effect of pDMN FC on the association between pDMN PiB-uptake and cognitive (i.e., ACCR4 − ACCR1) performance was significant ($\beta = -0.59$, $P < 0.001$) (Supplementary Fig. 5). The GFI of the moderator model was 0.9, indicating a good model fit. Moderating effects for the rATN and for CERAD scores were not significant.

Discussion

To address the hypothesis that, in early AD, FC of intrinsic networks is consistently changed across attention-demanding task- and rest-states, and that for such regions, aberrant intrinsic connectivity links with local Aβ-pathology and impaired cognition, patients with pAD and healthy older adults were assessed by a multimodal imaging approach including rs-fMRI and task-fMRI, PiB-PET, and neuropsychological examination. In 2 networks covering the medial and lateral PPC (namely the DMN and rATN), areas with consistently aberrant connectivity during rest and during an attention-demanding task were observed; patients' at-rest-FC of these areas was associated with both PiB-binding levels and the degree of cognitive impairment. Post hoc SEM confirmed a direct influence of DMN intrinsic connectivity on the association between PiB-uptake and cognitive impairment. Beyond the DMN, our study provides first evidence for an intrinsic network-based mechanism linking Aβ-pathology with impaired cognition in early AD.

Patients' pDMN and rATN: Consistent FC Changes During Rest and Task

Regionally Overlapping Aberrant Rest- and Task-FC

Corresponding to our first hypothesis, we observed regionally consistent abnormalities in the FC of the pDMN and rATN in patients with pAD during rest and task conditions (Figs 1

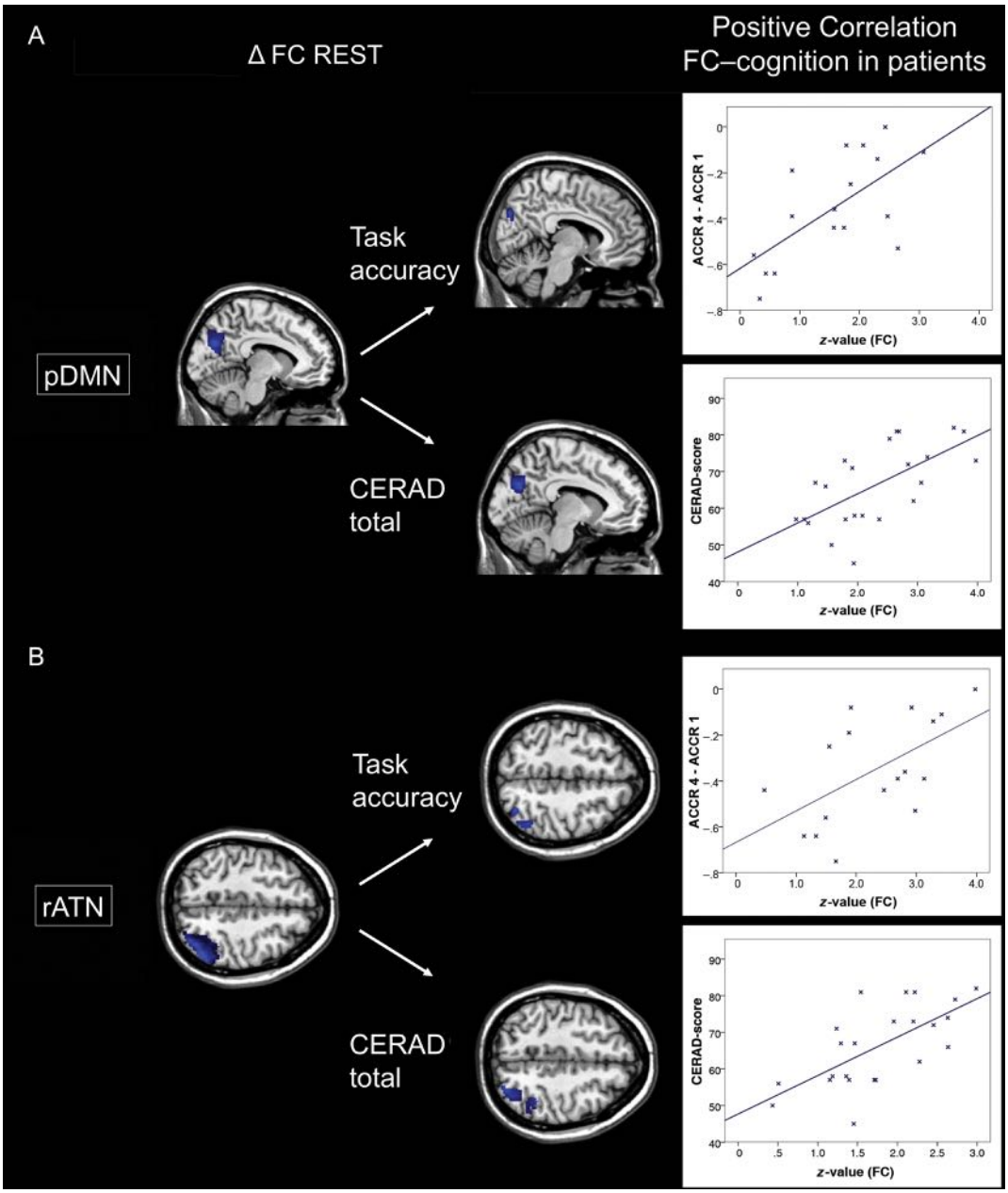

Figure 3. Patients' decreased FC of the pDMN and rATN is associated with impaired cognition. Column 1: Results of ICN group comparisons for FC maps between patients and controls (ΔFC) for the resting-state condition concerning pDMN (*A*) and rATN (*B*) (SPMs as in Fig. 1). Column 2: Patients' performance scores for cognitive accuracy (ACCR 4 – ACCR 1, assessed during task-fMRI) and CERAD total (neuropsychological assessment outside the scanner) were treated as continuous variables and regressed voxel-wise against pDMN/rATN FC maps, resulting in SPMs ($P < 0.05$ uncorrected and $k = 40$). Right side: For visualization, the relationship between cognitive performance and FC was assessed by Pearson correlation between averaged FC and cognitive performance scores across patients ($P < 0.05$; ACCR/CERAD total for pDMN $r = 0.65/0.64$, for rATN $r = 0.66/0.62$).

and 2; Supplementary Tables 1 and 3). While FC was lower during rest, it was increased during the attention-demanding task. The spatial consistency of FC group differences across rest and task suggests that pDMN/rATN intrinsic brain activity is robustly impaired in pAD (Fig. 2*A*,*B*). In the pDMN of patients, FC in the right precuneus was significantly less reduced during the task than that of healthy controls (Fig. 2*A*). This result corresponds with several previous observations of reduced DMN/medial PPC deactivation in MCI/AD during various cognitive tasks (Lustig and Buckner 2004; Rombouts et al. 2005; Petrella et al. 2007). In contrast to these studies, here we showed a reduced decrease in "connectivity" rather than in evoked activation (in line with Celone et al. 2006). In addition, increased task-FC in the right and dorsal ATN was found in the inferior and superior PPC in patients compared with controls (Figs 1*B* and 2*B*; Supplementary Table 3). Several previous studies have demonstrated increased parietal task-FC or activation, especially in MCI patients with very mild impairments (Dickerson et al. 2004; Celone et al. 2006).

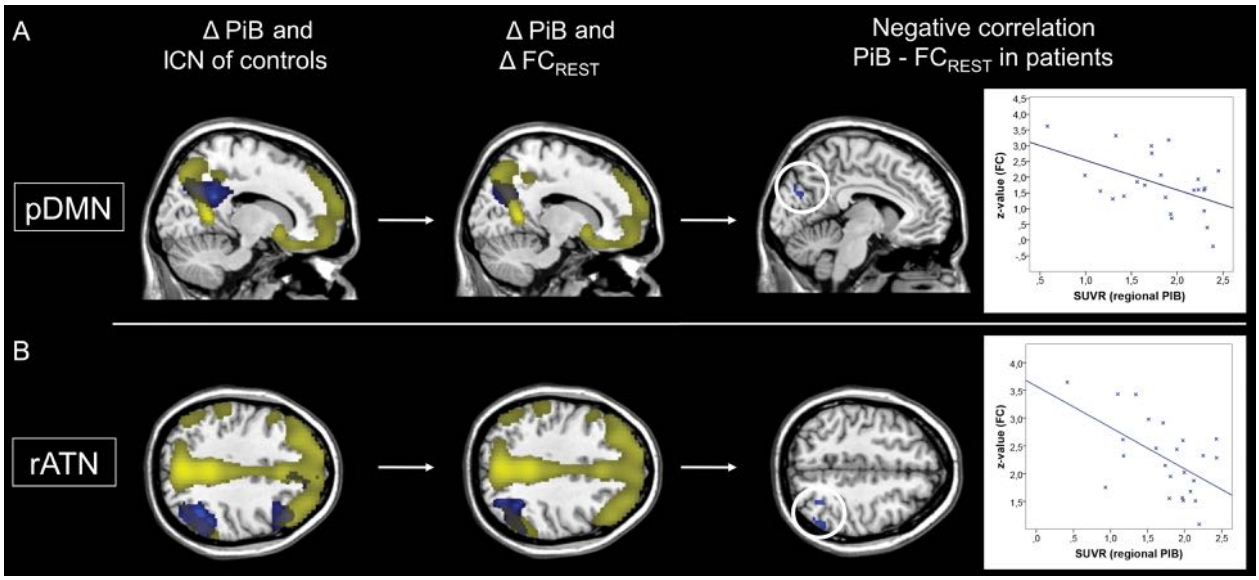

Figure 4. Patients' decreased FC of the pDMN and rATN is associated with increased local PiB-uptake. Columns 1 and 2: For the pDMN (*A*) and rATN (*B*), resting-state FC maps of controls (FC) and of group comparisons between patients and controls (ΔFC) are overlapped with the group difference map of increased PiB-uptake in patients (SPMs as in Fig. 1). Column 3: Patients' local PiB-uptake scores of overlapping rest- and task group differences were treated as continuous variables and regressed voxel-wise against pDMN and rATN FC maps, resulting in corresponding SPMs ($P < 0.05$ uncorrected and $k = 40$). Right side: For visualization, the relationship between FC and PiB-uptake was assessed by Pearson correlation between average FC and regional PiB-uptake across patients ($P < 0.05$; for pDMN $r = -0.50$, for rATN $r = -0.56$).

Directions of FC Changes

Even though the group differences in DMN and ATN connectivity were spatially consistent across rest- and task-states, the 2 networks showed dissimilar responses to the applied attention-demanding task (with the DMN barely changing in patients, while the right ATN showed an abnormal FC increase; Fig. 2). Since we have no a priori reason to believe that Aβ-pathology should affect (at least cortical) connectivity differently in different ICNs (if they are burdened with similar amounts of pathology), other factors must explain this divergence in their task response. It is well known that the amount of task-evoked FC increase in an ICN depends on the functional specialization of the ICN in question (Calhoun et al. 2001, 2008; Eichele et al. 2008; Smith et al. 2009; Laird et al. 2011; Raichle 2011). The right ATN, spanning regions known to be involved in the top-down control of attention (e.g., Nobre et al. 1997), should be functionally involved in our cognitive task including increasing top-down attention, and should therefore show a group difference that reflects the group difference in task performance. Thus, the data indicate that impaired cognitive performance goes along with an increased demand of concerted activity within task-relevant regions or networks. The abnormal connectivity increase might therefore reflect a compensatory mechanism in the presence of reduced cognitive capacities going along with pAD. On the other hand, a regular DMN decrease of FC during attention is impaired in patients.

Reduced Rest-FC and Atrophy

Concerning resting-state FC, we observed lower FC within the posterior DMN and the right ATN in the medial and lateral PPC, respectively, in patients (Fig. 1*B* and Supplementary Table 3). This result replicates a previous independent finding of our group, observed in MCI patients when compared with controls (Sorg et al. 2007). Even though atrophy was only marginally present (Supplementary Fig. 4 and Supplementary Table 2), lower FC in the DMN and rATN may have been related to reductions in gray matter volume (as previously reported, see Agosta et al. 2012). Accordingly, FC decreases in the rATN were no longer significant when adding network gray matter volumes as a covariate into the group comparisons. This indicates that findings of altered rATN connectivity in pAD are closely linked to decreases in gray matter volume. Medial and lateral components of the temporal lobes were most strongly affected by gray matter decreases (Supplementary Fig. 4 and Supplementary Table 2), but parts of the frontal lobe (predominantly orbital frontal) also showed significant gray matter decreases in patients compared with healthy controls. This finding illustrates that changes in gray matter volume should be taken into consideration when investigating alterations in FC within ATNs in patients with pAD. Of note, the strength of FC decrease in the pDMN was only reduced but remained significant after adding network gray matter volumes as a covariate into the group comparisons. While disrupted FC within the DMN is a very consistent and robust finding in MCI, AD dementia, and even in prodromal stages of the disease (Sorg et al. 2007; Hedden et al. 2009; Mormino et al. 2011; Agosta et al. 2012), disrupted FC within ATNs is less consistently reported (for example, for the dorsal ATN, see Li et al. 2011 or Sorg et al. 2007 and for lateralized ATNs, see Agosta et al. 2012 or Li et al. 2011). The obviously stronger influence of gray matter atrophy on ATN FC may explain this to some degree.

Linking PiB-Uptake, Reduced Resting-State FC, and Impaired Cognition

Patients' pDMN and rATN: Disrupted Intrinsic Connectivity Is Associated with Impaired Cognition

In patients, disrupted resting-state FC of pDMN and rATN in the medial/lateral PPC was positively related with impaired cognition (Fig. 3*A*,*B*; Supplementary Table 5). Such relationship was found for both cognitive task performance and

CERAD total scores reflecting general cognitive performance. The result is specific to the pDMN and rATN, as in the auditory network correspondent results were not found. The observed consistency across different cognitive scores suggests a general impact of disrupted pDMN/rATN connectivity in the PPC on cognitive performance. This general impact on cognitive performance might be explained by both the hub character of the medial and lateral PPC and the correspondent PPC involvement in a wide range of cognitive tasks (Gitelman et al. 1999; Corbetta and Shulman 2002; Dosenbach et al. 2008; Buckner et al. 2009; Smith et al. 2009).

Patients' pDMN and rATN: Disrupted Intrinsic Connectivity Is Associated with Local PiB-Uptake

We found that, in the medial and lateral PPC, increased local PiB uptake was overlapping and negatively correlated with patients' resting-state FC of the pDMN and rATN, respectively (Fig. 4 and Supplementary Table 5). This negative association between PiB-uptake and intrinsic FC was exactly in those areas that were characterized by both aberrant task- and at-rest-FC. This finding was specific to the pDMN and rATN, since in the auditory control network corresponding results were not found. A negative association between PiB-binding levels and resting-state FC has been reported in previous studies for the DMN (Hedden et al. 2009; Mormino et al. 2011) and the ATN (Myers et al. 2014) for persons with and without cognitive symptoms. Particularly, Drzezga et al. (2011) found that cortical regions such as precuneus or inferior parietal lobule, which are characterized by extensive FC with other parts of the cortex, are related to neuronal dysfunction (measured by FDG-PET), reduced resting-state FC, and increased PiB-uptake in patients with MCI. Taken together with results from animal studies demonstrating significant effects of local Aβ-pathology on ongoing activity (e.g., Busche et al. 2008; for a review see Palop and Mucke 2010), our data suggest that, in patients, the significant association between higher PiB-binding levels and lower intrinsic FC may reflect an adverse effect of Aβ-pathology on intrinsic FC in DMN and ATN.

No Simple Mediating Role of Aberrant Intrinsic Networks Between Amyloid Pathology and Impaired Cognition

Based on significant pairwise relations between impaired at-rest-FC and PiB-uptake/impaired cognitive performance, we expected aberrant FC to mediate between Aβ-pathology and cognition. However, instead of such a mediating effect, we found a moderating effect for only the pDMN on the relation between PiB-uptake and impaired cognitive performance for the precuneus (Supplementary Fig. 5). The higher the at-rest-FC in the precuneus, the less the effect of PiB-uptake on performance. In other words, precuneus FC works as a modulatory context factor to translate pathology effects into impaired cognition, instead of directly mediating Aβ-pathology effects. This finding suggests a complex, non-linear relationship between Aβ-pathology as defined by PiB-uptake, intrinsic FC, and cognitive performance, likely including further modulatory factors (Myers et al. 2014). We speculate that factors such as cognitive reserve (Barulli and Stern 2013) or individual baseline relationship between network connectivity and Aβ-pathology (Myers et al. 2014) might play a role. Future studies that explicitly analyze such factors are necessary.

In this context, it is important to emphasize the special role of the precuneus with respect to its PiB-uptake signal. While we found—in line with others (e.g., Hedden et al. 2009; Mormino et al. 2011)—correspondent precuneus PiB-uptake and FC reduction, suggesting a link between local plaque load and connectivity, recent neuropathological studies have challenged whether increased PiB-uptake in the precuneus really reflects increased plaque load. For example, Nelson et al. (2009) found that in patients with AD–dementia, significant precuneus plaque load was only detectable in the minority of cases. Similar findings were reported by Perez et al. (2014). Furthermore, precuneus synapse integrity seems to be largely preserved at least in early AD (Scheff et al. 2013), while cholinergic activity is specifically reduced (Ikonomovic et al. 2011). Based on these findings and on our result of linked PiB-uptake and at-rest-FC, precuneus Aβ-pathology as defined by PiB-uptake may be more strongly related to disrupted connectivity than to plaque load or aberrant synapses. Further studies are certainly necessary to better understand the specific neural underpinnings of altered PiB-uptake and Blood-oxygen-level dependent-FC measures particularly in the precuneus.

Conclusion

In pAD, we observed regionally overlapping abnormalities in FC during resting-state and cognitive task conditions in the precuneus of the posterior DMN and inferior parietal lobule of the ATN. Furthermore, patients' disrupted resting-state FC was related with both increased local PiB-uptake and impaired cognitive performance. Finally, instead of a simple linear mediation, we found disrupted DMN connectivity to have a complex moderating effect on the influence of Aβ-pathology on impaired cognition in AD.

Supplementary Material

Supplementary material can be found at: http://www.cercor.oxfordjournals.org/.

Funding

This work was supported by the Wellcome Trust (N.E.M.), Alzheimer Foundation Initiative (C.S.), German Federal Ministry of Education and Research (BMBF 01EV0710 to A.M.W. and BMBF 01ER0803 to C.S.), and the Kommission für Klinische Forschung, Technische Universität München (KKF 8765162 to C.S).

Notes

We are grateful to the participants of the study and the staff of the Department of Psychiatry and Neuroradiology for their help in recruitment and data collection. *Conflict of Interest*: All authors report no biomedical financial interests or potential conflicts of interest.

References

Agosta F, Pievani M, Geroldi C, Copetti M, Frisoni GB, Filippi M. 2012. Resting state fMRI in Alzheimer's disease: beyond the default mode network. Neurobiol Aging. 33:1564–1578.

Albert MS, DeKosky ST, Dickson D, Dubois B, Feldman HH, Fox NC, Gamst A, Holtzman DM, Jagust WJ, Petersen RC et al. 2011. The diagnosis of mild cognitive impairment due to Alzheimer's disease: recommendations from the National Institute on Aging-Alzheimer's Association workgroups on diagnostic guidelines for Alzheimer's disease. Alzheimers Dement. 7:270–279.

Allen EA, Erhardt EB, Damaraju E, Gruner W, Segall JM, Silva RF, Havlicek M, Rachakonda S, Fries J, Kalyanam R et al. 2011. A baseline for the multivariate comparison of resting-state networks. Front Syst Neurosci. 5:2.
Baron RM, Kenny DA. 1986. The moderator-mediator variable distinction in social psychological research: conceptual, strategic, and statistical considerations. J Pers Soc Psychol. 51:1173–1182.
Barulli D, Stern Y. 2013. Efficiency, capacity, compensation, maintenance, plasticity: emerging concepts in cognitive reserve. Trends Cogn Sci. 17:502–509.
Berkes P, Orbán G, Lengyel M, Fiser J. 2011. Spontaneous cortical activity reveals hallmarks of an optimal internal model of the environment. Science. 331:83–87.
Braak H, Braak E, Bohl J. 1993. Staging of Alzheimer-related cortical destruction. Eur Neurol. 33:403–408.
Brett M, Anton J-L, Valabregue R, Poline J-B. 2002. Region of interest analysis using an SPM toolbox [abstract]. Presented at the 8th International Conference on Functional Mapping of the Human Brain, 2–6 June 2002, Sendai, Japan. Available on CD-ROM in NeuroImage. 16(2).
Buckner RL, Andrews-Hanna JR, Schacter DL. 2008. The brain's default network: anatomy, function, and relevance to disease. Ann N Y Acad Sci. 1124:1–38.
Buckner RL, Sepulcre J, Talukdar T, Krienen FM, Liu H, Hedden T, Andrews-Hanna JR, Sperling RA, Johnson KA. 2009. Cortical hubs revealed by intrinsic functional connectivity: mapping, assessment of stability, and relation to Alzheimer's disease. J Neurosci. 29:1860–1873.
Busche MA, Eichhoff G, Adelsberger H, Abramowski D, Wiederhold KH, Haass C, Staufenbiel M, Konnerth A, Garaschuk O. 2008. Clusters of hyperactive neurons near amyloid plaques in a mouse model of Alzheimer's disease. Science. 321:1686–1689.
Calhoun VD, Adalı T, Pearlson GD, Pekar JJ. 2001. Spatial and temporal independent component analysis of functional MRI data containing a pair of task-related waveforms. Hum Brain Mapp. 13:43–53.
Calhoun VD, Kiehl KA, Pearlson GD. 2008. Modulation of temporally coherent brain networks estimated using ICA at rest and during cognitive tasks. Hum Brain Mapp. 29:828–838.
Celone KA, Calhoun VD, Dickerson BC, Atri A, Chua EF, Miller SL, DePeau K, Rentz DM, Selkoe DJ, Blacker D et al. 2006. Alterations in memory networks in mild cognitive impairment and Alzheimer's disease: an independent component analysis. J Neurosci. 2640:10222–10231.
Corbetta M, Shulman GL. 2002. Control of goal-directed and stimulus-driven attention in the brain. Nat Rev Neurosci. 3:215–229.
Damoiseaux JS, Rombouts SARB, Barkhof F, Scheltens P, Stam CJ, Smith SM, Beckmann CF. 2006. Consistent resting-state networks across healthy subjects. Proc Natl Acad Sci. 103:13848–13853.
Dannhauser TM, Walker Z, Stevens T, Lee L, Seal M. 2005. The functional anatomy of divided attention in amnestic mild cognitive impairment. Brain. 128:1418–1427.
Dickerson BC, Salat DH, Bates JF, Atiya M, Killiany RJ, Greve DN, Dale AM, Stern CE, Blacker D, Albert MS et al. 2004. Medial temporal lobe function and structure in mild cognitive impairment. Ann Neurol. 56:27–35.
Dosenbach NUF, Fair DA, Cohen AL, Schlaggar BL, Petersen SE. 2008. A dual-networks architecture of top-down control. Trends Cogn Sci. 12:99–105.
Drzezga A, Becker JA, Van Dijk KR, Sreenivasan A, Talukdar T, Sullivan C, Schultz AP, Sepulcre J, Putcha D, Greve D et al. 2011. Neuronal dysfunction and disconnection of cortical hubs in non-demented subjects with elevated amyloid burden. Brain. 134: 1635–1646.
Dubois B, Feldman HH, Jacova C, DeKosky ST, Barberger-Gateau P, Cummings J, Delacourte A, Galasko D, Gauthier S, Jicha G et al. 2007. Research criteria for the diagnosis of Alzheimer's disease: revising the NINCDS–ADRDA criteria. Lancet Neurol. 6:734–746.
Eichele T, Debener S, Calhoun VD, Specht K, Engel AK, Hugdahl K, von Cramon DY, Ullsperger M. 2008. Prediction of human errors by maladaptive changes in event-related brain networks. Proc Natl Acad Sci. 105:6173–6178.
Engler H, Forsberg A, Almkvist O, Blomquist G, Larsson E, Savitcheva I, Wall A, Ringheim A, Långström B, Nordberg A. 2006. Two-year follow-up of amyloid deposition in patients with Alzheimer's disease. Brain. 129:2856–2866.
Ferri CP, Prince M, Brayne C, Brodaty H, Fratiglioni L, Ganguli M, Hall K, Hasegawa K, Hendrie H, Huang Y et al. 2005. Global prevalence of dementia: a Delphi consensus study. Lancet. 366:2112–2117.
Fox MD, Raichle ME. 2007. Spontaneous fluctuations in brain activity observed with functional magnetic resonance imaging. Nat Rev Neurosci. 8:700–711.
Gauthier S, Reisberg B, Zaudig M, Petersen RC, Ritchie K, Broich K, Belleville S, Brodaty H, Bennett D, Chertkow H et al. 2006. Mild cognitive impairment. Lancet. 367:1262–1270.
Gitelman DR, Nobre AC, Parrish TB, LaBar KS, Kim Y-H, Meyer JR, Mesulam MM. 1999. A large-scale distributed network for covert spatial attention: further anatomical delineation based on stringent behavioural and cognitive controls. Brain. 122:1093–1106.
Greicius MD, Srivastava G, Reiss AL, Menon V. 2004. Default-mode network activity distinguishes Alzheimer's disease from healthy aging: evidence from functional MRI. Proc Natl Acad Sci. 101:4637–4642.
Grimmer T, Henriksen G, Wester HJ, Förstl H, Klunk WE, Mathis CA, Kurz A, Drzezga A. 2009. Clinical severity of Alzheimer's disease is associated with PIB uptake in PET. Neurobiol Aging. 30:1902–1909.
Hansson O, Zetterberg H, Buchhave P, Londos E, Blennow K, Minthon L. 2006. Association between CSF biomarkers and incipient Alzheimer's disease in patients with mild cognitive impairment: a follow-up study. Lancet Neurol. 5:228–234.
Hedden T, Van Dijk KRA, Becker JA, Mehta A, Sperling RA, Johnson KA, Buckner RL. 2009. Disruption of functional connectivity in clinically normal older adults harboring amyloid burden. J Neurosci. 29:12686–12694.
Ikonomovic MD, Klunk WE, Abrahamson EE, Wuu J, Mathis CA, Scheff SW, Mufson EJ, DeKosky ST. 2011. Precuneus amyloid burden is associated with reduced cholinergic activity in Alzheimer disease. Neurology. 77:39–47.
Karrasch M, Sinervä E, Grönholm P, Rinne J, Laine M. 2005. CERAD test performances in amnestic mild cognitive impairment and Alzheimer's disease. Acta Neurol Scand. 111:172–179.
Laird AR, Fox PM, Eickhoff SB, Turner JA, Ray KL, McKay DR, Glahn DC, Beckmann CF, Smith SM, Fox PT. 2011. Behavioral interpretations of intrinsic connectivity networks. J Cogn Neurosci. 23: 4022–4037.
Lewis CM, Baldassarre A, Committeri G, Romani GL, Corbetta M. 2009. Learning sculpts the spontaneous activity of the resting human brain. Proc Natl Acad Sci USA. 106:17558–17563.
Li R, Wu X, Fleisher AS, Reiman EM, Chen K, Yao L. 2011. Attention-related networks in Alzheimer's disease: a resting functional MRI study. Hum Brain Mapp. 33:1076–1088.
Lustig C, Buckner RL. 2004. Preserved neural correlates of priming in old age and dementia. Neuron. 42:865–875.
Mandal PK. 2012. Predictive biomarkers for Alzheimer's disease using state-of-the-art brain imaging techniques. J Alzheimer's Dis. 31: S1–S3.
Mormino EC, Smiljic A, Hayenga AO, Onami S, Greicius MD, Rabinovici GD, Janabi M, Baker SL, Yen IV, Madison CM et al. 2011. Relationships between beta-amyloid and functional connectivity in different components of the default mode network in aging. Cereb Cortex. 21:2399–2407.
Morris JC. 1993. The Clinical Dementia Rating (CDR): current version and scoring rules. Neurology. 43:2412–2414.
Morris JC, Heyman A, Mohs RC, Hughes JP. 1989. The consortium to establish a registry for Alzheimer's disease (CERAD): I. Clinical and neuropsychological assessment of Alzheimer's disease. Neurology. 39:1159–1165.
Mosconi L, Tsui WH, Herholz K, Pupi A, Drzezga A, Lucignani G, Reiman EM, Holthoff V, Kalbe E, Sorbi S et al. 2008. Multicenter standardized ^{18}F-FDG PET diagnosis of mild cognitive impairment, Alzheimer's disease, and other dementias. J Nucl Med. 49:390–398.
Myers N, Pasquini L, Göttler J, Grimmer T, Koch K, Ortner M, Neitzel J, Mühlau M, Förster S, Kurz A et al. 2014. Within-patient

correspondence of amyloid-β and intrinsic network connectivity in Alzheimer's disease. Brain. doi:10.1093/brain/awu103.
Nelson PT, Abner EL, Scheff SW, Schmitt FA, Kryscio RJ, Jicha GA, Smith CD, Patel E, Markesbery WR. 2009. Alzheimer's-type neuropathology in the precuneus is not increased relative to other areas of neocortex across a range of cognitive impairment. Neurosci Lett. 450:336–339.
Neufang S, Akhrif A, Riedl V, Förstl H, Kurz A. 2011. Disconnection of frontal and parietal areas contributes to impaired attention in very early Alzheimer's disease. J Alzheimer's Dis. 25:309–321.
Nobre AC, Sebestyen GN, Gitelman DR, Mesulam MM, Frackowiak RS, Frith CD. 1997. Functional localization of the system for visuospatial attention using positron emission tomography. Brain. 120:515–533.
Palop JJ, Mucke L. 2010. Amyloid-β-induced neuronal dysfunction in Alzheimer's disease: from synapses toward neural networks. Nat Neurosci. 13:812–818.
Perez SE, He B, Nadeem M, Wuu J, Scheff SW, Abrahamson EE, Ikonomovic MD, Mufson EJ. 2014. Resilience of precuneus neurotrophic signaling pathways despite amyloid pathology in prodromal Alzheimer's disease. Biol Psychiatry. doi:10.1016/j.biopsych.2013.12.016.
Petrella JR, Wang L, Krishnan S, Slavin MJ, Prince SE, Tran TTT, Doraiswamy PM. 2007. Cortical deactivation in mild cognitive impairment: high-field-strength functional MR imaging. Radiology. 245:224–235.
Power JD, Barnes KA, Snyder AZ, Schlaggar BL, Petersen SE. 2012. Spurious but systematic correlations in functional connectivity MRI networks arise from subject motion. NeuroImage. 59:2142–2154.
Raichle ME. 2011. The restless brain. Brain Connectivity. 1:3–12.
Riedl V, Valet M, Wöller A, Sorg C, Vogel D, Sprenger T, Boecker H, Wohlschläger AM, Tölle TR. 2011. Repeated pain induces adaptations of intrinsic brain activity to reflect past and predict future pain. NeuroImage. 57:206–213.
Rombouts SARB, Barkhof F, Goekoop R, Stam CJ, Scheltens P. 2005. Altered resting state networks in mild cognitive impairment and mild Alzheimer's disease: an fMRI study. Hum Brain Mapp. 26:231–239.
Scheff SW, Price DA, Schmitt FA, Roberts KN, Ikonomovic MD, Mufson EJ. 2013. Synapse stability in the precuneus early in the progression of Alzheimer's disease. J Alzheimers Dis. 35:599–609.
Schlösser RGM, Koch K, Wagner G. 2007. Assessing the state space of the brain with fMRI: an integrative view of current methods. Pharmacopsychiatry. 40:85–92.
Selkoe DJ. 2002. Alzheimer's disease is a synaptic failure. Science. 298:789–791.
Sheline YI, Raichle ME, Snyder AZ, Morrise JC, Head D, Wang S, Mintun MA. 2010. Amyloid plaques disrupt resting state default mode network connectivity in cognitively normal elderly. Biol Psychiatry. 67:584–587.
Smith SM, Fox PT, Miller KL, Glahn DC, Fox PM, Mackay CE, Filippini N, Watkins KE, Toro R, Laird AR et al. 2009. Correspondence of the brain's functional architecture during activation and rest. Proc Natl Acad Sci. 106:13040–13045.
Sorg C, Riedl V, Mühlau M, Calhoun VD, Eichele T, Laer L, Drzezga A, Förstl H, Kurz A, Zimmer C et al. 2007. Selective changes of resting-state networks in individuals at risk for Alzheimer's disease. Proc Natl Acad Sci. 104:18760–18765.
Sorg C, Riedl V, Perneczky R, Kurz A, Wohlschläger AM. 2009. Impact of Alzheimer's disease on the functional connectivity of spontaneous brain activity. Curr Alzheimer Res. 6:541–553.
Sperling RA, Dickerson BC, Pihlajamaki M, Vannini P, LaViolette PS, Vitolo OV, Hedden T, Becker JA, Rentz DM, Selkoe DJ et al. 2010. Functional alterations in memory networks in early Alzheimer's disease. NeuroMol Med. 12:27–43.
Sperling RA, LaViolette PS, O'Keefe K, O'Brien J, Rentz DM, Pihlajamaki M, Marshall G, Hyman BT, Selkoe DJ, Hedden T et al. 2009. Amyloid deposition is associated with impaired default network function in older persons without dementia. Neuron. 63:178–188.
Van Dijk KRA, Sabuncu MR, Buckner RL. 2012. The influence of head motion on intrinsic functional connectivity MRI. NeuroImage. 59:431–438.

Evaluation of Reproducibility of Diffusion Tensor Imaging in the Brachial Plexus at 3.0 T

Michael J. Ho, MD, Andrei Manoliu, MD, PhD,* Felix Pierre Kuhn, MD, MAS,* Bram Stieltjes, MD, PhD,† Markus Klarhöfer, PhD,‡ Thorsten Feiweier, PhD,‡ Magda Marcon, MD,* and Gustav Andreisek, MD, MBA, PhD**

Objective: The aim of this study was to evaluate the reproducibility of 3 T magnetic resonance imaging diffusion tensor imaging (DTI) of the brachial plexus in healthy subjects.

Methods: Ten healthy volunteers were included, and morphological and DTI sequences of the nerve roots of the brachial plexus from C5 to T1 of both sides were repeatedly acquired on a 3 T magnetic resonance system (MAGNETOM Skyra; Siemens Healthcare, Erlangen, Germany). A prototype diffusion-weighted single-shot echo-planar imaging sequence-enabling slice-specific shim adjustments was performed with b-values of 0 and 800 s/mm^2 in 30 gradient directions, resulting in an acquisition time of about 6 minutes each in axial orientation. Between scans, subjects were moved and repositioned in the scanner, coils were reinserted, and new localizers were acquired. Image analysis was performed using MITK Diffusion software toolkit. Two independent readers performed diffusion data postprocessing, and regions of interest (ROIs) were set on the proximal postganglionic trunk at each spinal level, bilaterally to obtain values for fractional anisotropy (FA) and mean diffusivity (MD). Interreader and intrareader agreement as well as test-retest reproducibility of DTI metrics were assessed.

Results: Intraclass correlation coefficients (ICCs) for interreader and intrareader agreement did not differ significantly between measurements for FA and MD. In particular, ICCs for interreader agreement of FA ranged from 0.741 to 0.961 and that of MD ranged from 0.802 to 0.998, and ICCs for intrareader agreement of FA ranged from 0.759 to 0.949 and that of MD ranged from 0.796 to 0.998. The test-retest reproducibility of DTI metrics showed an overall moderate to strong correlation ($r > 0.707$), with few minor exceptions, for both FA and MD values.

Conclusions: Diffusion tensor imaging metrics in the brachial plexus are reproducible. Future applications of DTI for a possible clinical use should be further investigated.

Key Words: MRN, DTI peripheral nerves, brachial plexus

(*Invest Radiol* 2017;52: 482–487)

The brachial plexus is composed of a complex network of nerves consisting on the ventral rami of the C5 to C8 and T1 nerve roots, and additional contributions may derive from the C4 and T2 nerve roots. A high number of abnormalities ranging from traumatic nerve injury to radiation neuropathy can affect the brachial plexus. Clinical differentiation of brachial plexopathy from other spine abnormalities manifesting with plexopathy-like symptoms (eg, shoulder and arm pain or weakness) might be challenging, and results from electromyographic or electroneurologic tests are often indeterminate. In this scenario, magnetic resonance imaging (MRI), particularly, magnetic resonance neurography (MRN), has been increasingly used in cases of suspected brachial plexopathy and peripheral neuropathy to confirm the diagnosis.[1–3]

In recent studies, diffusion-weighted imaging, as well as diffusion tensor imaging (DTI), has been applied for visualization of peripheral nerves.[4–7] Because of its capability to provide insights into neuronal microstructure, DTI in particular may depict abnormalities of the brachial plexus stemming from compression of nerve roots from cervical disc herniation or those resulting from neoplastic conditions even beyond conventional morphologic MRN.[4,7] In general, DTI derives estimates of water diffusion in a specific tissue using voxel-wise calculations of tissue fiber orientation on the basis of tensor as a 3-dimensional ellipsoid model. This model is characterized by its eigenvectors and eigenvalues (k_1, k_2, k_3) in all 3 directions. The quantitative degree of anisotropy of water diffusion can be described by the fractional anisotropy (FA) and is a scalar value ranging from 0 to 1, with 0 representing isotropic diffusion and with 1 representing complete anisotropic diffusion. This model of water diffusion can be transferred to the peripheral nerve, where bundles of axons run parallel in 1 principal direction and the nerve surrounding the myelin sheaths limits the diffusion of water molecules in perpendicular directions. Reduced FA values were observed in abnormal conditions with Wallerian degeneration, whereas increased FA values were noted in case of ongoing regeneration.[8] The mean diffusivity (MD) equals the apparent diffusion coefficient and corresponds to the averaged diffusivity of the 3 principle eigenvalues in a voxel, commonly published in $\times 10^{-3}$ s/mm^2 ($MD = (\lambda_1 + \lambda_2 + \lambda_3)/3$. An increase in MD values was stated in nerve injury with demyelination.[9,10] Although DTI is an established technique for the evaluation of nerve integrity in the central nervous system, its application in the peripheral nervous system with the plexus is more demanding. The relatively small size of peripheral nerves and the subsequent lower signal-to-noise ratios (SNRs) make DTI susceptible to partial volume effects, and the anatomical shape of the neck region gives rise to susceptibility-induced distortion artifacts. Still, the peripheral nerves and the plexus with their high directionality along the axons are suited for DTI measurements. Therefore, DTI has the potential to become a clinical biomarker for demyelination and fibrotic changes of the peripheral nerve structure in the brachial plexus.[11,12] Given the recently growing utilization of DTI-based clinical research of the brachial plexopathies, it was the aim of this study to investigate the reproducibility of DTI parameter measurements, in healthy volunteers, using a DTI sequences with isotropic voxels optimized for the brachial plexus and suited for clinical routine.

MATERIALS AND METHODS

Study Subjects

Institutional ethics board approval and written informed consent of all volunteers were obtained. Ten healthy volunteers (mean age, 30.6 ± 5.3 years; range, 23–41 years), 6 women (mean age, 28.6 ± 5.9 years;

Received for publication September 15, 2016; and accepted for publication, after revision, January 27, 2017.

From the *Institute of Diagnostic and Interventional Radiology, University Hospital Zurich, University of Zurich, Zurich; †Department of Radiology, University of Basel, Basel; and ‡Siemens Healthcare AG, Zurich, Switzerland.

Conflicts of interest and sources of funding: none declared.

Markus Klarhöfer is an employee of Siemens Healthcare GmbH, Erlangen, Germany.

Correspondence to: Michael J. Ho, MD, Institute of Diagnostic and Interventional Radiology, University Hospital Zurich, Raemistrasse 100, CH-8091 Zurich, Switzerland. E-mail: michael.ho@usz.ch.

ISSN: 0020-9996/17/5208–0482

DOI: 10.1097/RLI.0000000000000363

TABLE 1. Sequence Parameters

	DTI	SPACE STIR
b-value 1/2, s/mm^2	0/800	/
TR, ms	5600	3500
TE, ms	67	166
Matrix	100 × 88	256 × 256
FOV, mm^2	190 × 168	205 × 205
In-plane resolution, mm^2	1.9 × 1.9	0.8 × 0.8
No. slices	44	144
Slice thickness, mm	1.9	0.8
Pixel bandwidth, Hz/px	1666	454
Acquisition time, min:s	06:39	07:11

DTI indicates diffusion tensor imaging (used here: prototype diffusion-weighted ss-EPI sequence-enabling slice-specific shim adjustments); SPACE, sampling perfection with application of optimized contrasts using different flip angle evolution; STIR, short tau inversion recovery; TR, repetition time; TE, echo time; FOV, field of view.

range, 23–41 years) and 4 men (mean age, 33.3 ± 3.0 years; range, 28–37 years), were recruited. Exclusion criteria were general contraindications to magnetic resonance (ie, pacemaker, claustrophobia), age younger than 18 years, history of findings related to nerve abnormalities (ie, upper extremity pain, paresthesia, or hypesthesia), history of cervical spine abnormalities, or prior surgery of the cervical spine or the brachial plexus.

Magnetic Resonance Imaging

Morphological and DTI sequences of the brachial plexus of both sides were acquired on a 3.0 T magnetic resonance system (MAGNETOM Skyra; Siemens Healthcare, Erlangen, Germany) using a commercially available 64-channel head-neck coil and appropriate elements of both an 18-channel body array and a 32-channel spine array between May and October 2015. An isotropic T2-weighted sampling perfection with application of optimized contrasts using different flip angle evolution (SPACE) sequence with short tau inversion recovery (STIR) fat suppression in coronal orientation was applied for better anatomical orientation with the following sequence parameters: repetition time, 3500 milliseconds; echo time, 166 milliseconds; voxel size, 0.8 × 0.8 mm; slice thickness, 0.8 mm; number of slices, 144; field of view (FOV), 260 × 260 mm; receive bandwidth, 454 Hz/px. A prototype diffusion-weighted single-shot echo-planar imaging (ss-EPI) sequence-enabling slice-specific shim adjustments with b-values of 0 and 800 s/mm^2 in 30 gradient directions was applied, acquiring voxels with an isotropic dimension of 1.9 mm.[13,14] Total acquisition time corresponded to 21 minutes. Pulse sequence-specific DTI parameters are summarized in Table 1.

Slice-specific shim adjustments facilitate the acquisition of echo-planar images with decent image quality in the neck region. Because of its intrinsically low bandwidth along the phase-encoding direction, EPI quality suffers from the presence of residual fat signal as well as from local, subject-induced B0 field inhomogeneities. For multislice acquisitions, established shim procedures enable partial mitigation of these degradations only: this is due to the fact that a single, static setting of first- and, if applicable, higher-order shim fields that satisfies average optimization criteria gets applied throughout the measurement for the complete set of slices. The ss-EPI sequence prototype used in this study supports localized, slice-specific optimizations and dynamically switches assigned shim settings synchronously with the acquisition of each slice.[13,14]

After the initial scan, each subject underwent a second separate MRI examination on the same day in the same scanner. The second scanning session contained the identical DTI sequence of the initial session. Between the 2 scans, volunteers were moved and repositioned in the scanner, coils were replaced, and new localizers were acquired (Fig. 1).

Image Analysis

All 3-dimensional data sets were analyzed by 2 independent readers (reader 1, M.J.H., research fellow in musculoskeletal radiology with 2 years' training in neuroradiology; reader 2, A.M., clinical fellow in musculoskeletal radiology with a PhD in neuroimaging, both with experience in diffusion data postprocessing and peripheral nerve segmentation) according to the sequential scheme reported in Figure 1. The open-source software MITK Diffusion (release 2015.05; www.mitk.org) was used for postprocessing of raw data and to perform diffusion tensor maps for FA and MD estimation for each subject.[15] Fractional anisotropy and MD values were obtained as follows: at all levels from C5 to T1, nerves roots in both sides were identified on the SPACE STIR sequence and on the TRACE image obtained from postprocessing of DTI data. Subsequently, on the TRACE-weighted images, circular regions of interest (ROIs) with a fixed area of 11 mm^2 were set on the proximal postganglionic, supraclavicular trunks of both sides at all levels of the brachial plexus. Regions of interest were

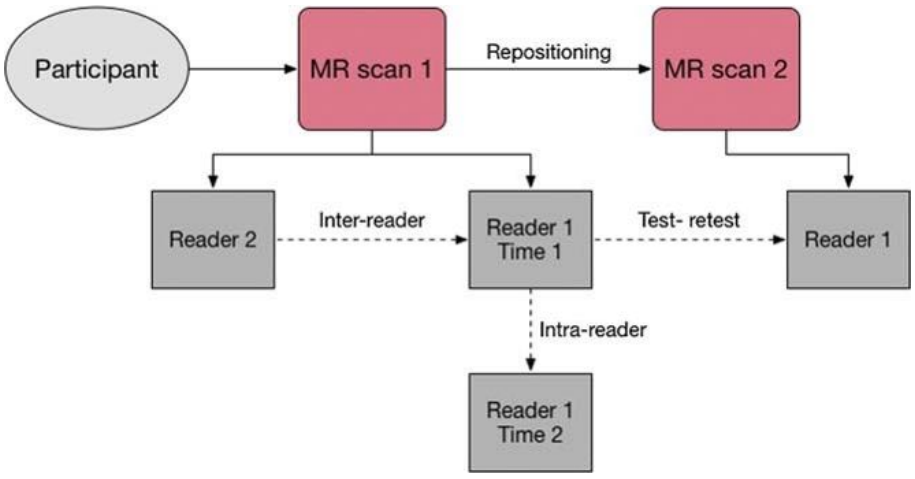

FIGURE 1. Flow chart of study procedures. Participants underwent 2 magnetic resonance scans with repositioning between scans. For reproducibility of measurements, independent readouts were performed by 2 readers after the first scan and 6 weeks later by 1 reader. For test-retest reproducibility, 1 reader performed an additional measurement of DTI metrics. Figure 1 can be viewed online in color at www.investigativeradiology.com.

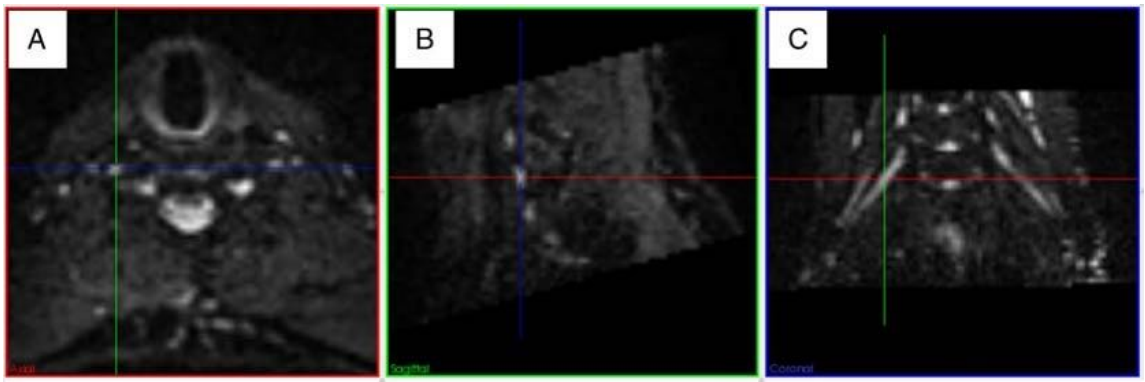

FIGURE 2. Measurement of diffusion metrics with MITK Diffusion toolkit at the level of C6 on the right supraclavicular brachial plexus in a 36-year-old man. Reference lines on axial (A) and sagittal (B) reconstructions and on coronal (C) TRACE images of the DTI magnetic resonance scan were used for ROI placement in the trunks of the supraclavicular brachial plexus of both sides. Figure 2 can be viewed online in color at www.investigativeradiology.com.

meticulously positioned within the brachial plexus at the level of the trunks to minimize partial volume effects (Fig. 2). Subsequently, the software automatically calculated corresponding FA and MD values. The same procedure was also performed to obtain FA and MD values of spinal cord at C7 level.

Statistical Analysis

All statistical analyses were performed using SPSS (release 22.0; SPSS Inc, Chicago, IL). Descriptive statistics was performed, and mean FA and MD values were obtained from the analysis of reader 1 after the first readout and from reader 2. For the assessment of interreader and intrareader agreement of measurements, intraclass correlation coefficients (ICCs) for mean FA and for mean MD values of each level of the brachial plexus from C5 to T1 for both sides and the spinal cord at the level of C7 were computed. To calculate ICCs between independent readers, 2-way random effects models were applied. Interreader and intrareader agreement was considered excellent for values greater than 0.75, values between 0.40 and 0.75 reported fair to good reliability, and values below 0.40 indicated poor agreement.[16] For reproducibility analysis, test-retest Pearson correlation coefficients were calculated for FA and MD and interpreted as follows: correlation was considered weak when r was less than 0.3, moderate when r was between 0.3 and 0.7, and strong when r was greater than 0.7. Results were referred to as statistically significant when P value is equal to 0.025. Statistical tests were Bonferroni corrected for multiple comparisons, where applicable.

RESULTS

Morphological and DTI images were successfully acquired in all healthy volunteers. In all T2 SPACE STIR images and in all TRACE images of all subjects, the supraclavicular brachial plexus was completely delineated and the course of nerve structure was depicted without discontinuity (Fig. 3). Mean FA and MD values and the detailed results from ICC analysis and Pearson correlation analyses are demonstrated in Table 2.

Interreader and Intrareader Agreement

An excellent interreader and intrareader agreement (ICC > 0.756 and ICC > 0.759, respectively) was observed for both FA and MD values at all levels, except for the FA value at C5 level on the left side (ICC = 0.741). The highest ICC for interreader agreement with 0.961 ($P < 0.001$) for FA was noted at the level of C6 on the left side, and that for intrareader agreement with 0.949 ($P < 0.001$) for FA was noted at the level of T1 left. The lowest interreader and intrareader agreement for FA was found at the level of C5 left with an ICC of 0.741 ($P = 0.025$) and at the level of C5 right with an ICC of 0.759 ($P = 0.023$), respectively. For MD, the highest ICC for interreader and intrareader was found at the level of C5 on the right side and was 0.998 ($P < 0.001$) for both. The lowest interreader correlation with an ICC of 0.796 ($P = 0.13$) and

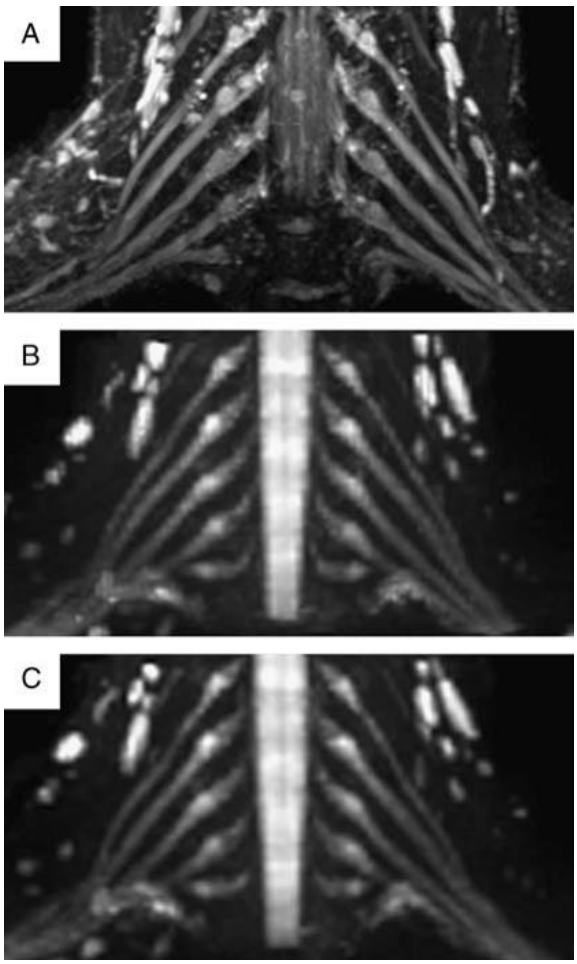

FIGURE 3. Morphological correlation and results for repeated DTI scans in a 27-year-old healthy female volunteer. Panel A, coronal SPACE STIR of the brachial plexus for anatomical orientation; panel B, coronal maximum intensity projection of the TRACE image of the DTI magnetic resonance from scan 1 (slab thickness, 37.0 mm); panel C, coronal maximum intensity projection of the TRACE image of the DTI magnetic resonance from scan 2 (slab thickness, 37.0 mm). Brachial plexus anatomy is repeatedly and clearly depicted in scan 1 (B) and scan 2 (C) in accordance with the SPACE STIR image (A) as reference image.

TABLE 2. Mean FA and MD Values for Scan 1, ICCs for Interreader and Intrareader Agreement and Pearson Correlation Coefficients for Test-Retest

Level	Mean Magnetic Resonance Scan 1	SD	ICC Interreader	ICC Intrareader	Test-Retest (Pearson *r*)
C5 Right					
FA	0.42	0.04	0.838 (0.347–0.960)*	0.759 (0.031–0.939)†	0.361
MD	1.62‡	0.27‡	0.998 (0.993–1.000)§	0.998 (0.990–0.999)§	0.986*
C5 left					
FA	0.41	0.03	0.741 (0.001–0.938)	0.892 (0.567–0.973)*	0.569
MD	1.53‡	0.25‡	0.983 (0,932–0.996)§	0.986 (0.944–0.997)§	0.952*
C6 right					
FA	0.44	0.04	0.929 (0.713–0.982)§	0.797 (0.184–0.950)†	0.762†
MD	1.49‡	0.28‡	0.979 (0.916–0.995)§	0,988 (0.953–0.997)§	0.965*
C6 left					
FA	0.43	0.05	0.961 (0.844–0.990)§	0.946 (0.783–0.987)§	0.954*
MD	1.53‡	0.25‡	0.992 (0.967–0.998)§	0.985 (0.939–0.996)§	0.982*
C7 right					
FA	0.42	0.03	0.846 (0.378–0.962)*	0.825 (0.295–0.957)*	0.836*
MD	1.52‡	0.26‡	0,980 (0.920–0.995)§	0.986 (0.946–0.997)§	0.950*
C7 left					
FA	0.44	0.04	0.888 (0.550–0.972)*	0.834 (0.333–0.959)*	0.731†
MD	1.49‡	0.23‡	0.966 (0.864–0.992)§	0.962 (0,846–0.990)§	0.907*
C8 right					
FA	0.43	0.04	0.931 (0.723–0.983)§	0.937 (0.747–0.984)§	0.864*
MD	1.55‡	0.25‡	0.985 (0.940–0.996)§	0.965 (0.858–0.991)§	0.909*
C8 left					
FA	0.43	0.03	0.887 (0.545–0.972)*	0.871 (0.482–0.968)*	0.661
MD	1.61‡	0.23‡	0.965 (0.861–0.991)§	0.955 (0.819–0.989)§	0.952*
T1 right					
FA	0.39	0.02	0.756 (0.017–0.939)†	0.840 (0.356–0.960)*	0.707†
MD	1.54‡	0.23‡	0.802 (0.203–0.951)†	0.796 (0.178–0.949)†	0.598
T1 left					
FA	0.41	0.04	0.889 (0.553–0.972)*	0.949 (0.797–0.987)§	0.218
MD	1.57‡	0.13‡	0.934 (0,734–0.984)§	0.939 (0,753–0.985)§	0.893*
C7 spinal cord					
FA	0.72	0.04	0.866 (0.461–0.967)*	0.880 (0.516–0.970)*	0.794*
MD	0.91‡	0.04‡	0.924 (0.693–0.981)§	0.914 (0.654–0.979)*	0.933*

ROI-based measurements were performed in the supraclavicular plexus at the level of the trunks and for the spinal cord at the level of C7. FA and MD values are given as mean ± standard deviation.

*Corrected P values < 0.01.

†Corrected P values < 0.025.

‡Values indicate $\times 10^3$ mm^2/s.

§Corrected P values < 0.001.

FA indicates fractional anisotropy; MD, mean diffusivity; ICC, intraclass correlation coefficient; ROI, region of interest.

the lowest intrareader with an ICC of 0.802 ($P = 0.12$) for MD were found at the level of T1 at the right side.

Reproducibility

In the analysis of test-retest reproducibility of brachial plexus DTI parameters, an overall strong correlation was found ($r > 0.707$). Indeed, FA values demonstrated to be reproducible without significant differences between the independent readouts and showed throughout positive correlation between measurements of test and retest at most of the levels. Fractional anisotropy values were linearly but not significantly correlated only at the levels C5 of both sides and at C8 left and T1 left. Similar results were found for MD, with a nonsignificant but still linear correlation, only at the level of T1 on the right side ($r = 0.598$). Otherwise, all test-retest showed moderate to excellent correlation with values ranging from 0.361 (C5 right side) to 0.954 (C6 left side). Mean diffusivity Pearson correlation coefficients ranged from moderate to strong correlation with 0.598 ($P = 0.09$) for T1 right and with 0.986 ($P < 0.001$) for C5 right.

Spinal Cord Measurements

Evaluation of spinal cord at C7 level resulted in excellent ICCs for interreader correlation with 0.866 ($P = 0.03$) and for intrareader correlation with 0.924 ($P < 0.001$) for FA, and, respectively, with 0.924 ($P < 0.001$) and with 0.914 ($P < 0.001$) for MD. Test and retest demonstrated a strong linear correlation for FA (Pearson $r = 0.794$; $P = 0.06$) and strong linear correlation for MD (Pearson $r = 0.933$; $P < 0.001$).

DISCUSSION

In the current study, the reproducibility of quantitative DTI of the brachial plexus was assessed with a dedicated pulse sequence at 3 T.

Nerve course in the brachial plexus was clearly depicted in all anatomic and diffusion sequences for subsequent measurements. Intrareader, interreader, and test-retest showed excellent reproducibility of FA and MD values in almost all levels of the trunks of the brachial plexus from C5 to T1 of both sides.

In comparison to prior studies, which aimed to assess feasibility and reproducibility of DTI measurements in the brachial plexus,[7,17] this study is the only one in which test-retest MRI scans were conducted, including separate and independent postprocessing procedures for each scan, to comprehensively assess reproducibility. In addition, a novel imaging approach consisting of a conventional single-shot diffusion-weighted EPI sequence in combination with slice-selective optimization of the magnetic field homogeneity was used to reduce geometric distortions and improve fat suppression. Other approaches to reduce geometrical distortions in diffusion-weighted MRI include reduced FOV[18] imaging and readout-segmented acquisitions.[19] Compared with reduced FOV imaging, the sequence used in this study resulted in higher SNR. While readout-segmented EPI allows high in-plane resolutions, resulting measurement times of this multishot approach prevent its use for clinical DTI examinations requiring many diffusion encoding directions.

The decisive operator-dependent step in this study was the placement of ROIs in cross-sectional images for subsequent ROI-based data analysis. A fixed ROI diameter smaller than the nerve cross-sectional diameter restricted the contamination of DTI metrics from surrounding tissue with different diffusion characteristics. Provided that all ROIs were set within the nerve and taking into account the small nerve caliber, ROI data analysis for a test magnetic resonance scan was based only on a choice of few voxels—if not even identical voxels. Apart from an optimized setting in the trial with a dedicated design of the diffusion imaging protocol, state-to-the-art software and hardware, this might be an important factor for the overall good results for interreader, intrareader, and test-retest according to ICCs and Pearson correlation coefficients. For an assessment of relatively novel DTI of the brachial plexus, better established DTI of the spinal cord was conducted additionally at level of C7. A greater diameter of the spinal cord with a high directionality of nerve fibers is expected to result in a signal of nerve tissue not lower than the one to be yielded in the brachial plexus. In the central nervous system, it has been suggested that axonal diameter, density, and myelination have an influence on the measurement of diffusion parameters.[20,21] Beside this, DTI measurements in the spinal cord previously have been shown of high reproducibility.[22,23] In comparison to DTI measurements of the spinal cord, ICCs for interreader and intrareader DTI data of the brachial plexus at C7 for both sides showed only slightly lower ICCs for MD, but even better ICCs for FA values. Test and retest results were highly correlated for the spinal cord as well as for the brachial plexus. Still, DTI of the brachial plexus has an inherent SNR dilemma: on one hand, relatively small caliber of the nerves only allows voxel designs with smaller in-plane resolution than the cross-sectional diameter of the nerve itself to avoid partial volume effects from surrounding structures. Small voxel size, on the other hand, limits the signal that can be derived, resulting in unfavorable SNR. In this study, we used small isotropic voxel for a better adaption to nerve anatomy because some trunks leave the spinal cord in a rather steep angle to change direction again when passing behind the clavicle. When investigating only parts of the brachial plexus (other than in the brain, where crossing of nerve fibers can influence the precision of measurement of DTI metrics), anisotropic voxels, which allow for higher total voxel volume, might be an alternative to increase nerve signal.[24,25]

Limitations

Certain limitations in the study design have to be acknowledged. With 10 healthy volunteers, the number of subjects was small. Nevertheless, all data revealed consistency with low standard deviations. Furthermore, no symptomatic participants were included in this study. However, the aim of this study was to address the issue of reproducibility of measurement of DTI metrics before proceeding to promising clinical applications. In addition, the impact of vendor-specific differences in equipment on reproducibility on DTI parameter measurement was not assessed in this study. Previously, an investigation on the influence of different hardware in DTI measurement of peripheral nerves has revealed significant differences in absolute values of derived DTI parameters between vendors. However, due to consistently small standard deviations of absolute DTI values, no impact on larger clinical group studies with substantial DTI changes was expected.[26] Regarding interreader and interreader agreement between software packages, no substantial contribution to variance of software in DTI measurements was assumed.[27]

CONCLUSIONS

This study demonstrates that DTI metrics, FA, and MD in the brachial plexus are highly reproducible. Promising applications of DTI for a possible, future clinical use comprise a wide range of plexopathies from neurodegenerative diseases, tumor-like conditions, inflammation, and compression syndromes to trauma. Further studies are to be conducted to test if DTI of the brachial plexus can be of additional diagnostic value beyond traditional MRN.

REFERENCES

1. Chhabra A, Thawait GK, Soldatos T, et al. High-resolution 3 T MR neurography of the brachial plexus and its branches, with emphasis on 3D imaging. *AJNR Am J Neuroradiol*. 2013;34:486–497.
2. Du R, Auguste KI, Chin CT, et al. Magnetic resonance neurography for the evaluation of peripheral nerve, brachial plexus, and nerve root disorders. *J Neurosurg*. 2010;112:362–371.
3. Tagliafico A, Succio G, Emanuele Neumaier C, et al. MR imaging of the brachial plexus: comparison between 1.5-T and 3-T MR imaging: preliminary experience. *Skeletal Radiol*. 2011;40:717–724.
4. Chen YY, Lin XF, Zhang F, et al. Diffusion tensor imaging of symptomatic nerve roots in patients with cervical disc herniation. *Acad Radiol*. 2014;21:338–344.
5. Yuh EL, Jain Palrecha S, Lagemann GM, et al. Diffusivity measurements differentiate benign from malignant lesions in patients with peripheral neuropathy or plexopathy. *AJNR Am J Neuroradiol*. 2015;36:202–209.
6. Manoliu A, Ho M, Nanz D, et al. Diffusion tensor imaging of Lumbar nerve roots: comparison between fast readout-segmented and selective-excitation acquisitions. *Invest Radiol*. 2016;51:499–504.
7. Vargas MI, Viallon M, Nguyen D, et al. Diffusion tensor imaging (DTI) and tractography of the brachial plexus: feasibility and initial experience in neoplastic conditions. *Neuroradiology*. 2010;52:237–245.
8. Yamasaki T, Fujiwara H, Oda R, et al. In vivo evaluation of rabbit sciatic nerve regeneration with diffusion tensor imaging (DTI): correlations with histology and behavior. *Magn Reson Imaging*. 2015;33:95–101.
9. Kabakci N, Gürses B, Firat Z, et al. Diffusion tensor imaging and tractography of median nerve: normative diffusion values. *AJR Am J Roentgenol*. 2007;189:923–927.
10. Mac Donald CL, Dikranian K, Bayly P, et al. Diffusion tensor imaging reliably detects experimental traumatic axonal injury and indicates approximate time of injury. *J Neurosci*. 2007;27:11869–11876.
11. Pham M, Baeumer T, Bendszus M. Peripheral nerves and plexus: imaging by MR-neurography and high-resolution ultrasound. *Curr Opin Neurol*. 2014;27:370–379.
12. Chhabra A, Andreisek G, Soldatos T, et al. MR neurography: past, present, and future. *AJR Am J Roentgenol*. 2011;197:583–591.
13. Blamire AM, Rothman DL, Nixon T. Dynamic shim updating: a new approach towards optimized whole brain shimming. *Magn Reson Med*. 1996;36:159–165.
14. Feiweier T, Fischer D, Jeschke H, et al. Method for operating an MRI system, while also controlling gradient and shim sub-systems. US patent 8 633 690 B2. 2014.
15. Fritzsche KH, Neher PF, Reicht I, et al. MITK diffusion imaging. *Methods Inf Med*. 2012;51:441–448.
16. Borich MR, Kp Wadden, Boyd LA. Establishing the reproducibility of two approaches to quantify white matter tract integrity in stroke. *Neuroimage*. 2012;59:2393–2400.

17. Tagliafico A, Calabrese M, Puntoni M, et al. Brachial plexus MR imaging: accuracy and reproducibility of DTI-derived measurements and fibre tractography at 3.0-T. *Eur Radiol*. 2011;21:1764–1771.
18. Wheeler-Kingshott CA, Hickman SJ, Parker GJ, et al. Investigating cervical spinal cord structure using axial diffusion tensor imaging. *Neuroimage*. 2002;16:93–102.
19. Porter DA, Heidemann RM. High resolution diffusion-weighted imaging using readout-segmented echo-planar imaging, parallel imaging and a two-dimensional navigator-based reacquisition. *Magn Reson Med*. 2002;62:468–475.
20. Beaulieu C. The basis of anisotropic water diffusion in the nervous system - a technical review. *NMR Biomed*. 2002;15:435–455.
21. Sen PN, Basser PJ. A model for diffusion in white matter in the brain. *Biophys J*. 2005;89:2927–2938.
22. Barakat N, Shah P, Faro SH, et al. Inter- and intra-rater reliability of diffusion tensor imaging parameters in the normal pediatric spinal cord. *World J Radiol*. 2015; 7:279–285.
23. Brander A, Koskinen E, Luoto TM, et al. Diffusion tensor imaging of the cervical spinal cord in healthy adult population: normative values and measurement reproducibility at 3 T MRI. *Acta Radiol*. 2014;55:478–485.
24. Oouchi H, Yamada K, Sakai K, et al. Diffusion anisotropy measurement of brain white matter is affected by voxel size: underestimation occurs in areas with crossing fibers. *AJNR Am J Neuroradiol*. 2007;28:1102–1106.
25. Santarelli X, Garbin G, Ukmar M, et al. Dependence of the fractional anisotropy in cervical spine from the number of diffusion gradients, repeated acquisition and voxel size. *Magn Reson Imaging*. 2010;28:70–76.
26. Guggenberger R, Nanz D, Bussmann L, et al. Diffusion tensor imaging of the median nerve at 3.0 T using different MR scanners: agreement of FA and ADC measurements. *Eur J Radiol*. 2013;82:e590–e596.
27. Guggenberger R, Nanz D, Puippe G, et al. Diffusion tensor imaging of the median nerve: intra-, inter-reader agreement, and agreement between two software packages. *Skeletal Radiol*. 2012;41:971–980.

MR Neurographic Orthopantomogram: Ultrashort Echo-Time Imaging of Mandibular Bone and Teeth Complemented With High-Resolution Morphological and Functional MR Neurography

Andrei Manoliu, MD, PhD,[1] Michael Ho, MD,[1] Daniel Nanz, PhD,[1] Evelyn Dappa, MD,[1] Andreas Boss, MD, PhD,[1] David M. Grodzki, PhD,[2] Wei Liu, PhD,[3] Avneesh Chhabra, MD,[4] Gustav Andreisek, MD, MBA,[1] and Felix P. Kuhn, MD, MAS[1]*

Purpose: Panoramical radiographs or cone-beam computed tomography (CT) are the standard-of-care in dental imaging to assess teeth, mandible, and mandibular canal pathologies, but do not allow assessment of the inferior alveolar nerve itself nor of its branches. We propose a new technique for "MR neurographic orthopantomograms" exploiting ultrashort echo-time (UTE) imaging of bone and teeth complemented with high-resolution morphological and functional MR neurography.
Materials and Methods: The Institutional Review Board approved the study in 10 healthy volunteers. Imaging of the subjects mandibles at 3.0T (Magnetom Skyra, Siemens-Healthcare) using a 64-channel head coil with isotropic spatial resolution for subsequent multiplanar reformatting, was performed. Bone images were acquired using a 3D PETRA sequence (TE, 0.07 msec). Morphological nerve imaging was performed using a dedicated 3D PSIF and 3D SPACE STIR sequence. Functional MR neurography was accomplished using a new accelerated diffusion-tensor-imaging (DTI) prototype sequence (2D SMS-accelerated RESOLVE). Qualitative and quantitative image analysis was performed and descriptive statistics are provided.
Results: Image acquisition and subsequent postprocessing into the MR neurographic orthopantomogram by overlay of morphological and functional images were feasible in all 10 volunteers without artifacts. All mandibular bones and mandibular nerves were assessable and considered normal. Fiber tractography with quantitative evaluation of physiological diffusion properties of mandibular nerves yielded the following mean $\pm$ SD values: fractional anisotropy, 0.43 ± 0.07; mean diffusivity (mm^2/s), 0.0014 ± 0.0002; axial diffusivity, 0.0020 ± 0.0002, and radial diffusivity, 0.0011 ± 0.0001.
Conclusion: The proposed technique of MR neurographic orthopantomogram exploiting UTE imaging complemented with high-resolution morphological and functional MR neurography was feasible and allowed comprehensive assessment of osseous texture and neural microarchitecture in a single examination.

J. MAGN. RESON. IMAGING 2016;44:393–400.

The mandibular nerve and particularly its main branch, the inferior alveolar nerve (IAN), are susceptible to traumatic or iatrogenic injuries and might be affected by dental root pathologies apart from orthognathic surgery,[1] such as removal of molar teeth,[2] root canal treatment,[3] dental implants,[4] or block anesthesia.[5] Consequently, axonal injuries

View this article online at wileyonlinelibrary.com. DOI: 10.1002/jmri.25178

Received Dec 23, 2015, Accepted for publication Jan 20, 2016.

*Address reprint requests to: F.P.K., MAS Medical Physics ETH, Institute of Diagnostic and Interventional Radiology, University Hospital Zurich, CH-8091 Zurich, Switzerland. E-mail: Felix.Kuhn@usz.ch

From the [1]Institute of Diagnostic and Interventional Radiology, University Hospital Zurich, University of Zurich, Zurich, Switzerland; [2]Siemens Healthcare, Erlangen, Germany; [3]Siemens Shenzhen Magnetic Resonance Ltd, Shenzhen, China; and [4]Department of Radiology, Southwestern Medical Center, Dallas, Texas, USA

can result in neuroma formation with neuronal hyperexcitability.[6] As microsurgical repair of such injuries in a timely fashion often improves or restores sensation and relieves painful dysesthesia, prompt investigation of accordant pathologies is mandatory.[4]

Panoramical radiographs or cone-beam computed tomography (CBCT) are commonly used for preoperative planning in implantology and orthodontics as well as for endodontic and peridontic procedures.[7,8] Although these X-ray-based technologies are useful for the assessment of various osseous pathologies of the jaw, they do not allow assessment of the IAN proper or its branches.

In contrast, magnetic resonance imaging (MRI) with its inherently high soft-tissue contrast is particularly suited for qualitative and quantitative assessment of neuronal integrity,[9,10] but faces important challenges in the visualization of cortical bone. Cortical bone with its inherent low water content and very short transverse relaxation time yields almost no signal with standard MR sequences such as fast spin echo (FSE) or gradient-recalled echo (GRE) imaging.[11] Nonetheless, ultrashort echo-time (TE) image acquisition (<100 μs) has been shown to generate detectable signals from osseous structures.[12] Recent studies have shown the feasibility of qualitative and quantitative cortical bone imaging in correlation with micro-CT[13] and biomechanical properties.[14]

Further important challenges in MRI are susceptibility artifacts due to field inhomogeneity, especially in the oral cavity. The commonly used echo planar imaging (EPI) pulse sequence for diffusion-tensor-based functional neurography encompassing whole *k*-space sampling following a single excitation results in long echo-times. Consequently, the generated images are particularly sensitive to susceptibility artifacts due to spin dephasing. On the contrary, a readout segmented EPI (rsEPI) sequence using multiple excitations with segmented acquisition of *k*-space in readout direction allows shortening the echo-spacing and echo-time that consequently reduce susceptibility artifacts and T_2^* blurring.[15] Long acquisition times, however, prevented this technique from being applied in high-resolution isotropic diffusion tensor imaging (DTI) imaging of larger volumes. The currently available simultaneous multislice (SMS) acceleration technique[16] allows data acquisition in a scan time adequate for routine clinical practice.

For the assessment of morphologic neurography of small and thin peripheral nerves, the commonly used T_2-weighted (T_2w) fat-suppressed images do not allow for confident distinction between nerves and accompanying small blood vessels.[17] Recently, it has been shown that using a 3D reversed fast imaging with steady-state free-precession (PSIF) sequence with additional low-diffusion moment suppresses the signal from the vessels[18,19] and thus nerve-selective images are generated. Nevertheless, due to potential magic-angle artifacts inherent in short-TE imaging, T_2w images remain essential for the characterization of neuronal structures.[20]

We hypothesized that with recent advances it would be feasible to combine bone imaging with morphological and functional high-resolution MR neurography to gather comprehensive information about the mandible, teeth, and regional nerves in a single examination within scan times suitable for routine clinical practice.

Materials and Methods

This was an Ethical Board-approved prospective feasibility study of 10 healthy volunteers (seven women and three men; age range 20–50 years, mean $\pm$ SD, 27.9 ± 7.7 years). All participants provided written informed consent. Inclusion criteria consisted of age 18 years or older and good physical health. Exclusion criteria were contraindication to MR, regional surgery or recent trauma, and acute or chronic sensory disorders or painful dysesthesias.

Image Acquisition

Study participants were positioned in supine position, head first, and the lower jaw was imaged at 3.0T (Magnetom Skyra, Siemens Healthcare, Erlangen, Germany) between March and May 2015. Two transmit channels enabled independent transmission (TimTX TrueShape, Siemens Healthcare), and a 64-channel phased array coil sampled the signal. All sequences for morphological imaging were acquired with submillimeter spatial resolution for subsequent isotropic multiplanar reformatting. Slab-selective excitation was used for all 3D MR pulse sequences.

For cortical and cancellous bone imaging, a 3D PETRA (Pointwise Encoding Time reduction with Radial Acquisition) single-echo sequence (Quiet-Suite, Siemens Healthcare) was applied.[21] The minimal TE attainable was 0.07 msec. A 3D diffusion-weighted reversed fast imaging with steady-state precession (3D-PSIF) pulse sequence with inherent vascular signal suppression was used for selective nerve imaging. A diffusion moment value (b-value) of 85 s/mm^2 was chosen for optimized peripheral nerve-to-background contrast and signal-to-noise ratio (SNR).[18] A 3D T_2w SPACE (Sampling Perfection with Application optimized Contrasts using different flip angle Evolution) sequence with STIR (short tau inversion recovery) fat suppression was acquired primarily for neural tissue characterization.

Functional MR neurography was accomplished using a prototype sequence based on SMS accelerated rsEPI, in which a blipped-CAIPIRINHA approach[22] was used to reduce voxel blurring and enable higher acceleration. In preliminary studies,[23] SMS accelerated rsEPI provided sufficient SNRs for reliable fiber tracing of neuronal structures. Spatial resolution of the functional tensor images was isotropic as well, with a voxel size of $1.5 \times 1.5 \times 1.5$ mm^3. Pertinent parameters of the mentioned MR pulse sequences are summarized in Table 1.

Image Analysis

Image postprocessing was performed on a syngo-via platform (v. VB10A, Siemens Healthcare). Image analysis was executed by two independent readers (reader 1, A.M.: research fellow in musculoskeletal radiology with a PhD in neuroimaging; reader 2, F.P.K.:

TABLE 1. MR Neurographic Orthopantomogram Pulse Sequence Parameters for PETRA, T2w SPACE STIR, PSIF, and SMS rsEPI

Pulse sequence	PETRA	T2w SPACE STIR	PSIF	SMS rsEPI
Dimension	3D	3D	3D	2D
Slabs/slices	1/320	1/104	1/112	-/56
TR [msec]	3.61	4500	11.31	4470
TE [msec]	0.07	231[a]	3.76	71/110
Flip angle [degree]	6	Var.	30	90
Bandwidth [Hz/Px]	359	454	230	919
Fat suppression	—	STIR (TI 230 msec)	Water excit. normal	Fat sat.
b-value [s mm^{-2}]	—	—	85	0/1000[b]
FoV read [mm]	300	240	240	240
FoV phase [%]	100	70.3	100	100
Phase encoding dir.	[c]	R > > L	R > > L	A > > P
Matrix size	320 × 320	256 × 180	256 × 256	160 × 160
Slice thickness [mm]	0.9	0.9	0.9	1.5
Effective resolution [mm^3]	0.9 × 0.9 × 0.9	0.9 × 0.9 × 0.9	0.9 × 0.9 × 0.9	1.5 × 1.5 × 1.5
Averages	1	1.7	1	1[d]
Partial Fourier	—	6/8 (slice)	—	7/8 (readout)
GRAPPA accl. factor	—	2	—	2
SMS factor	—	—	—	2
Time of acquisition	4:56 min.	9:23 min.	4:16 min.	9:34 min.

[a]Echo spacing, 4.43 msec; echo train duration, 549 msec.
[b]Diffusion scheme, monopolar.
[c]Radial acquisition with 80,000 directions.
[d]Read out segments, 5; directions, 12.

clinical fellow in musculoskeletal radiology with 2 years training in neuroradiology).

Curved multiplanar reconstruction (MPR) was used to generate orthopantomogram like images from the 3D PETRA, T_2w SPACE-STIR, and PSIF datasets. Subsequently, the images were assessed in overlay mode in order to analyze the relationship of the IAN to the mandibular canal.

QUALITATIVE ANALYSIS. Qualitative assessment of image quality was performed independently by two readers using semiquantitative 4-point Likert scales. Grading of artifacts due to image distortion and artifacts due to motion and ghosting: 1, none; 2, low; 3, moderate; 4, high. Grading of the anatomical delineation of the mandibular canal and the dental roots and the IAN, respectively: 1, >90%; 2, 75–90%; 3, 50–75%; 4, <50%. Areas of poor anatomical delineation were attributed to the following segments of the mandible: 1) incisor, 2) canine, 3) premolar, 4) molar. Finally, the subjective overall image quality was addressed: 1, high; 2, moderate; 3, poor; 4, nondiagnostic.

QUANTITATIVE ANALYSIS. The syngo.via Neuro 3D tool (Siemens Healthcare) was used for quantitative assessment of the functional DTI data. Tractography was performed by two readers in consensus with the following tracking parameters: minimal tract length, 40 mm; angle threshold, 30°; fractional anisotropy (FA) threshold, 0.2. One region of interest (ROI) was placed on each side covering the mandibular canal at the level of the retromandibular triangle. Quantitatively assessed were the number of generated fiber tracts as well as FA values, mean diffusivity, axial diffusivity, and radial diffusivity of the IAN on both sides. Mean diffusivity = (Dx + Dy + Dz)/3; axial diffusivity = Dx; radial diffusivity = (Dy + Dz)/2.

Statistical Analysis

All statistical tests were performed by using the SPSS Statistics software (SPSS v. 22, IBM, Armonk, NY). Descriptive statistics were used for artifacts due to distortions, artifacts due to motion and ghosting, overall image quality, as well as FA, mean diffusivity, axial diffusivity, radial diffusivity, and the number of generated tracts for the IAN on both sides. The Cohen κ statistic was used to evaluate interobserver agreement. According to Landis and Koch,[24] kappa values of 0.41–0.60 were considered moderate agreement, values of 0.61–0.80 were considered substantial

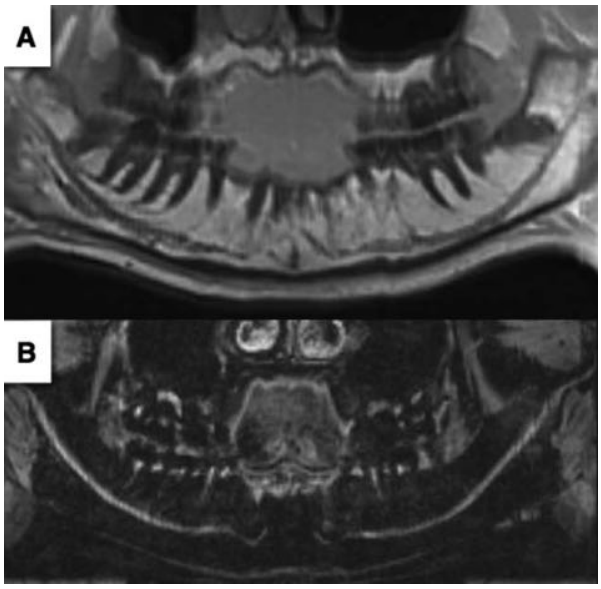

FIGURE 1: MR neurographic orthopantomogram. Curved planes reconstructed from 3D-PETRA (A) and 3D-PSIF (B) following the anatomical orientation of mandibular canal/nerve.

agreement, values of 0.81–0.99 were considered almost perfect agreement, and values of 1.00 were considered perfect agreement. Statistical significance was assumed for $P < 0.05$.

Results

Image acquisition was feasible within a total scan time of 28:08 minutes per subject. Image postprocessing into "MR neurographic orthopantomograms" by MPR (Fig. 1) and subsequent overlay of morphological and neurographic images was achieved without major coregistration mismatches in all 10 volunteers (Fig. 2).

Qualitative Analysis

Interrater agreement ranged from "substantial agreement" to "almost perfect agreement" (Cohen's kappa, 0.602–0.815) for the qualitative evaluation of all acquired MR sequences with respect to artifacts, delineation of the mandibular canal/nerve, as well as the overall image quality (Table 2).

In general, the overall image quality was excellent for all sequences and both readers (see Table 2 for a detailed presentation of the qualitative analysis). Furthermore, all sequences yielded no to low artifacts due to image distortions (Table 2). However, the 3D PETRA and 3D PSIF yielded low to moderate artifacts due to ghosting and/or motion (Table 2). All sequences yielded an excellent performance regarding the anatomical delineation of the mandibular canal and the IAN. In particular, the 3D PETRA yielded a complete depiction of the mandibular canal for all volunteers (Fig. 3), the 3D PSIF yielded a complete depiction of the IAN for 9 out of 10 volunteers (one volunteer with no visible delineation of the dental root in the area of the incisors), the 3D T_2w SPACE yielded a complete depiction of the IAN for 8 out of 10 volunteers (two volunteers without visible delineation of the dental root in the area of the incisors), and the SMS accelerated rsEPI yielded a complete depiction of the IAN in 8 out of 10 volunteers (one volunteer without visible delineation of the dental roots in the area of the incisors and one volunteer without visualization of the dental roots in the area of the incisors and canines).

Quantitative Analysis

Fiber tractography (Fig. 4) with quantitative evaluation of physiological diffusion properties of mandibular nerves was feasible in all volunteers. The number of generated fiber tracts (mean ± SD) was 52.73 ± 43.60 (right IAN, 51.44 ± 40.58; left IAN, 53.90 ± 46.12). Quantitative analysis of the obtained fiber tracts yielded the following mean ± SD values: FA, 0.43 ± 0.07 (right IAN, 0.43 ± 0.08; left IAN, 0.42 ± 0.06); mean diffusivity (mm^2/s), 0.0014 ± 0.0002

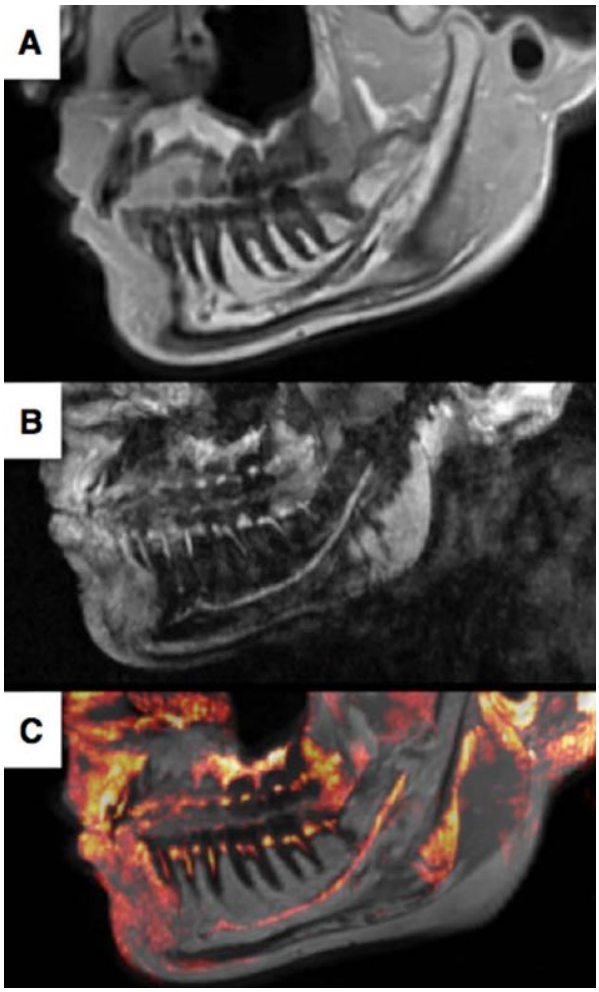

FIGURE 2: A: The mandibular canal acquired with PETRA. B: The mandibular nerve acquired with PSIF. C: An overlay of PETRA (gray scale) and PSIF (hot-metal scale).

TABLE 2. Qualitative Analysis for PETRA, T2 SPACE STIR, PSIF, and SMS rsEPI

	Reader 1		Reader 2		Kappa	*P*-value
	Mean	SD	Mean	SD		
PETRA						
Artifacts (distortions)	1.40	0.52	1.40	0.70	0.602	0.016
Artifacts (motion / ghosting)	2.50	0.53	2.40	0.52	0.800	0.010
Delineation left mandibular canal	1.20	0.42	1.30	0.48	0.737	0.016
Delineation right mandibular canal	1.10	0.32	1.20	0.42	0.615	0.035
Overall image quality	1.20	0.42	1.30	0.67	0.706	0.003
T2w SPACE STIR						
Artifacts (distortions)	1.20	0.42	1.30	0.67	0.706	0.003
Artifacts (motion / ghosting)	1.60	0.52	1.70	0.67	0.815	0.003
Delineation left IAN	1.20	0.42	1.10	0.32	0.615	0.035
Delineation right IAN	1.30	0.48	1.20	0.42	0.737	0.060
Overall image quality	1.30	0.48	1.30	0.48	0.624	0.098
PSIF						
Artifacts (distortions)	1.30	0.48	1.40	0.70	0.778	0.003
Artifacts (motion / ghosting)	2.30	0.48	2.20	0.42	0.747	0.015
Delineation left IAN	1.20	0.42	1.30	0.67	0.706	0.003
Delineation right IAN	1.30	0.48	1.30	0.67	0.612	0.024
Overall image quality	1.20	0.42	1.30	0.48	0.737	0.016
SMS rsEPI						
Artifacts (distortions)	1.30	0.48	1.40	0.52	0.783	0.011
Artifacts (motion / ghosting)	1.80	0.42	1.90	0.57	0.665	0.022
Delineation left IAN	1.40	0.70	1.30	0.48	0.778	0.003
Delineation right IAN	1.40	0.70	1.30	0.48	0.778	0.003
Overall image quality	1.40	0.70	1.50	0.71	0.804	0.001

Qualitative assessment was performed independently by two fellowship-trained radiologists using a semiquantitative 4-point Likert scale ranging from 1 to 4: artifacts due to image distortion or motion/ghosting (1, none; 4, high), delineation of the mandibular canal and the dental roots and the IAN, respectively (1, $>90\%$; 4, $<50\%$), overall image quality (1, high; 4, nondiagnostic). For interreader agreement, kappa values and corresponding *P*-values are given.

(right IAN, 0.0014 ± 0.0002; left IAN, 0.0014 ± 0.0002); axial diffusivity, 0.0020 ± 0.0002 (right IAN, 0.0020 ± 0.0002; left IAN, 0.0020 ± 0.0003), and radial diffusivity, 0.0011 ± 0.0001 (right IAN, 0.0011 ± 0.0001; left IAN, 0.0011 ± 0.0002).

Discussion

Our results support the hypothesis that recent advances in high-field MR technology enable the acquisition of orthopantomogram-like MR images complemented with high-resolution morphological and functional MR-neurography in a routine clinical setting (total scan time 28 min). Certain advances are associated with the recently emerged SMS acceleration technique.[25,26] Other advances are due to multichannel phased-array MR coils capable of UTE image acquisition (TE <100 μs) in combination with fast and robust signal sampling strategies, ie, radial filling of the *k*-space, allowing for cancellous and cortical bone imaging. Finally, higher-field MRI with inherent higher SNRs facilitates high-resolution 3D imaging in a reasonable scan time for clinical routine.

The applied 3D PETRA pulse sequence generated robust images of the mandible and adjacent structures. In fact, due to fast radial signal sampling, susceptibility to motion is particularly low. Cortical bone and teeth with inherent very short transverse relaxation yielded detectable signals, even though they were rather low compared to the high signal of adjacent fatty bone marrow and subcutaneous

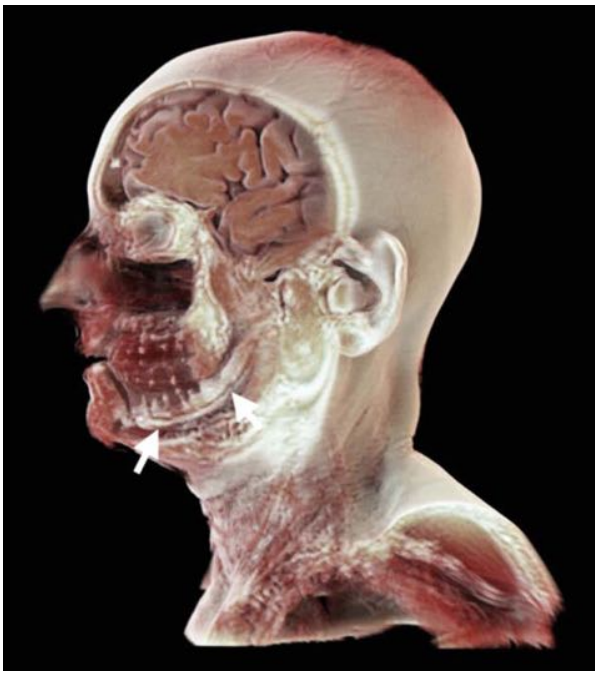

FIGURE 3: Volume rendered 3D data acquired using PETRA. The orientation was chosen to depict the left mandibular canal in full detail (see white arrows).

fat. The available UTE sequence did not permit acquiring a second echo with longer TE, thus image subtraction and subsequent contrast optimization of cortical bone was not possible. Nonetheless, anatomical delineation of the mandibular canal, dental roots, and the IAN was possible with a high diagnostic confidence and good interreader reliability.

T_2w images are important to evaluate normal nerve anatomy and to detect pathological alterations of the fascicular bundles.[20] Generally, the optimal image plane for peripheral nerve assessment is perpendicular to the long axis of the nerve, thus isotropic 3D data acquisition and subsequent multiplanar image reconstruction is favored. Uniform fat suppression was achieved with an inversion recovery preparation pulse (STIR). This is of major importance, as intraneural signal abnormalities can be subtle and surrounding fat may obscure these findings.[20] The additional 3D PSIF sequence with vascular signal suppression due to low-diffusion moment allowed for selective visualization of the IAN. Therefore, this sequence may facilitate detection of individual fascicle discontinuity, focal nerve size alterations, focal trace deviations, neuroma-in-continuity or end-bulb neuroma. Due to short echo times, however, this sequence showed more magic-angle artifacts compared to the T_2w image acquisition. A drawback of 3D acquisition schemes is its susceptibility to motion artifacts. Nevertheless, in the present study slight swallowing artifacts did not deteriorate image quality to a significant degree.

Regarding neurographic DTI data acquisition, the rsEPI sequence (RESOLVE) elicited no major distortion artifacts due to disruption of the local magnetic field in the oral cavity. Interestingly, even though the readout segmentation renders the sequence more prone to motion artifacts,

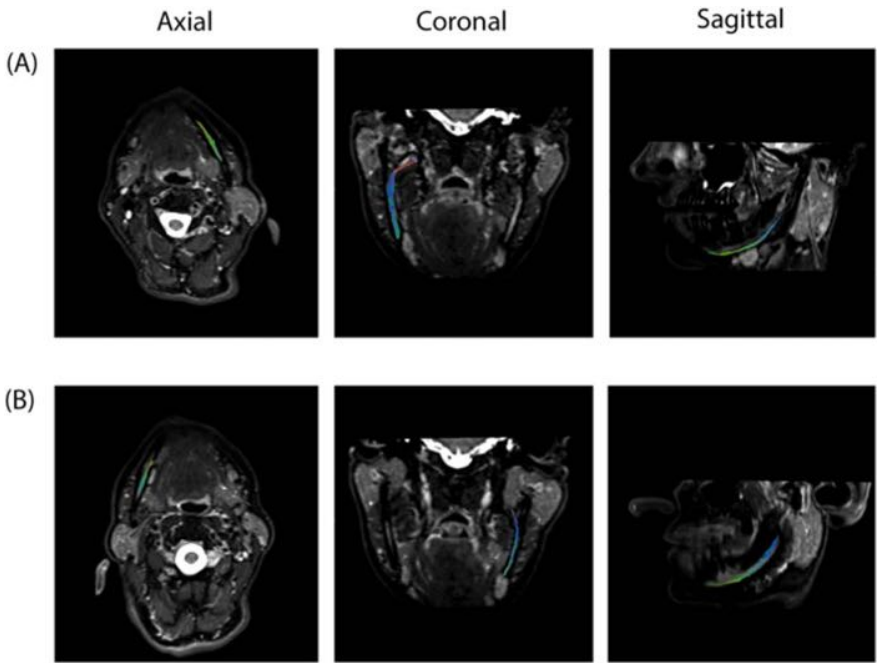

FIGURE 4: Functional MR neurography of the inferior alveolar nerve. A,B: The calculated fiber tracts of the right and left inferior alveolar nerves of a healthy volunteer in axial, coronal and sagittal orientation, respectively. All fiber tracts were fused with a T_2w SPACE STIR sequence to allow for better anatomical orientation.

no considerable impact on image quality was found. The robustness of the acquired data might be partly attributed to a markedly reduced image acquisition time thanks to the SMS acceleration technique and partly to motion navigators, which control and correct corrupted segments.

The advantage of DTI is its ability to provide insight into the neural microarchitecture and to quantify nerve pathologies. Particularly, a decrease in the FA, reflecting loss of the physiological anisotropy of water diffusion along the neuronal fascicles, and an increased MD, representing higher diffusivity, might help to characterize neuronal lesions. Furthermore, it has been suggested that increased axial diffusivity values imply axonal damage, whereas an increase in radial diffusivity rather reflects myelin degradation.[27] Our results revealed symmetrical IAN fiber-tracts and quantitative values within the expected range for peripheral nerves.[10]

Finally, the high and isotropic resolution of the morphological data allows for convenient image assessment in any orientation of the 3D space. In addition, postprocessing of the acquired data by curved MPR into orthopantomogram-like images visualizes panoramically the entire IAN along its course through the mandibular canal and facilitates the comparison of MR with conventional radiographical images. The subsequent overlay of MR-neurographic data to the morphological bone images permits simultaneous assessment of osseous and neural structures, particularly important for pathologies that affect both of these anatomical entities.

Certain limitations have to be acknowledged: The single-echo UTE sequence was acquired without fat suppression in order to detect potential bone marrow replacement by pathological processes. However, due to the high signal of fat when compared to the rather low signal of cortical bone and teeth, intrinsic contrast of the latter structures was rather poor. Although 3D T_2w SPACE with STIR obviates the need for an additional fat-suppressed sequence, one might use a fat saturation or water excitation technique to ameliorate the contrast within the structures with short transverse relaxation time and consecutively add a T_1w sequence for bone marrow replacement detection to the imaging protocol. A T_1w sequence will also be useful in the clinical setting for detection of perineural scarring and nerve entrapment from traumatic or iatrogenic injuries. The rather young volunteer population does not allow extrapolation of the quantitative reference values for functional MR-neurography to an older population. Thus, age-matched controls will have to be used for further patient studies and potential artifacts related to dental implants will have to be assessed separately.

In conclusion, the proposed technique of MR neurographic orthopantomogram exploiting UTE imaging complemented with high-resolution morphological and functional MR neurography was feasible and allowed comprehensive assessment of osseous texture and neural microarchitecture in a single examination and within scan times suitable for routine clinical practice.

Acknowledgment

The authors thank Markus Klarhöfer, PhD, Siemens Healthcare Switzerland, for his appreciated support.

Conflict of Interest

David Grodzki is an employee of Siemens Healthcare GmbH, Erlangen, Germany. Wei Liu is an employee of Siemens Shenzhen Magnetic Resonance Ltd., Shenzhen, China. All other authors declare no conflicts of interest.

References

1. Seo K, Tanaka Y, Terumitsu M, Someya G. Characterization of different paresthesias following orthognathic surgery of the mandible. J Oral Maxillofac Surg 2005;63:298–303.
2. Bataineh AB. Sensory nerve impairment following mandibular third molar surgery. J Oral Maxillofac Surg 2001;59:1012–1017; discussion 1017.
3. Pogrel MA. Damage to the inferior alveolar nerve as the result of root canal therapy. J Am Dent Assoc 2007;138:65–69.
4. Hegedus F, Diecidue RJ. Trigeminal nerve injuries after mandibular implant placement—practical knowledge for clinicians. Int J Oral Maxillofac Implants 2006;21:111–116.
5. Hillerup S, Jensen R. Nerve injury caused by mandibular block analgesia. Int J Oral Maxillofac Surg 2006;35:437–443.
6. Terumitsu M, Seo K, Matsuzawa H, Yamazaki M, Kwee IL, Nakada T. Morphologic evaluation of the inferior alveolar nerve in patients with sensory disorders by high-resolution 3D volume rendering magnetic resonance neurography on a 3.0-T system. Oral Surg Oral Med Oral Pathol Oral Radiol Endod 2011;111:95–102.
7. De Vos W, Casselman J, Swennen GR. Cone-beam computerized tomography (CBCT) imaging of the oral and maxillofacial region: a systematic review of the literature. Int J Oral Maxillofac Surg 2009;38:609–625.
8. Dreiseidler T, Mischkowski RA, Neugebauer J, Ritter L, Zoller JE. Comparison of cone-beam imaging with orthopantomography and computerized tomography for assessment in presurgical implant dentistry. Int J Oral Maxillofac Implants 2009;24:216–225.
9. Chhabra A, Zhao L, Carrino JA, et al. MR neurography: advances. Radiol Res Pract 2013;2013:809568.
10. Naraghi AM, Awdeh H, Wadhwa V, Andreisek G, Chhabra A. Diffusion tensor imaging of peripheral nerves. Semin Musculoskelet Radiol 2015;19:191–200.
11. Chang EY, Du J, Chung CB. UTE imaging in the musculoskeletal system. J Magn Reson Imaging 2015;41:870–883.
12. Du J, Bydder GM. Qualitative and quantitative ultrashort-TE MRI of cortical bone. NMR Biomed 2013;26:489–506.
13. Geiger D, Bae WC, Statum S, Du J, Chung CB. Quantitative 3D ultrashort time-to-echo (UTE) MRI and micro-CT (muCT) evaluation of the temporomandibular joint (TMJ) condylar morphology. Skeletal Radiol 2014;43:19–25.
14. Bae WC, Chen PC, Chung CB, Masuda K, D'Lima D, Du J. Quantitative ultrashort echo time (UTE) MRI of human cortical bone: correlation with porosity and biomechanical properties. J Bone Miner Res 2012;27:848–857.
15. Porter DA, Heidemann RM. High resolution diffusion-weighted imaging using readout-segmented echo-planar imaging, parallel imaging

and a two-dimensional navigator-based reacquisition. Magn Reson Med 2009;62:468–475.

16. Larkman DJ, Hajnal JV, Herlihy AH, Coutts GA, Young IR, Ehnholm G. Use of multicoil arrays for separation of signal from multiple slices simultaneously excited. J Magn Reson Imaging 2001;13:313–317.
17. Chhabra A, Flammang A, Padua A, Jr., Carrino JA, Andreisek G. Magnetic resonance neurography: technical considerations. Neuroimaging Clin N Am 2014;24:67–78.
18. Chhabra A, Subhawong TK, Bizzell C, Flammang A, Soldatos T. 3T MR neurography using three-dimensional diffusion-weighted PSIF: technical issues and advantages. Skeletal Radiol 2011;40:1355–1360.
19. Chhabra A, Soldatos T, Subhawong TK, et al. The application of three-dimensional diffusion-weighted PSIF technique in peripheral nerve imaging of the distal extremities. J Magn Reson Imaging 2011; 34:962–967.
20. Andreisek G, Chhabra A. MR neurography: pitfalls in imaging and interpretation. Semin Musculoskelet Radiol 2015;19:94–102.
21. Grodzki DM, Jakob PM, Heismann B. Ultrashort echo time imaging using pointwise encoding time reduction with radial acquisition (PETRA). Magn Reson Med 2012;67:510–518.
22. Setsompop K, Gagoski BA, Polimeni JR, Witzel T, Wedeen VJ, Wald LL. Blipped-controlled aliasing in parallel imaging for simultaneous multislice echo planar imaging with reduced g-factor penalty. Magn Reson Med 2012;67:1210–1224.
23. Frost R, Jezzard P, Douaud G, Clare S, Porter DA, Miller KL. Scan time reduction for readout-segmented EPI using simultaneous multislice acceleration: Diffusion-weighted imaging at 3 and 7 Tesla. Magn Reson Med 2014 [Epub ahead of print].
24. Landis JR, Koch GG. The measurement of observer agreement for categorical data. Biometrics 1977;33:159–174.
25. Katscher U, Bornert P. Parallel RF transmission in MRI. NMR Biomed 2006;19:393–400.
26. Wu X, Schmitter S, Auerbach EJ, Moeller S, Ugurbil K, Van de Moortele PF. Simultaneous multislice multiband parallel radiofrequency excitation with independent slice-specific transmit B1 homogenization. Magn Reson Med 2013;70:630–638.
27. Sun SW, Liang HF, Le TQ, Armstrong RC, Cross AH, Song SK. Differential sensitivity of in vivo and ex vivo diffusion tensor imaging to evolving optic nerve injury in mice with retinal ischemia. Neuroimage 2006;32:1195–1204.

Simultaneous Multislice Readout-Segmented Echo Planar Imaging for Accelerated Diffusion Tensor Imaging of the Mandibular Nerve: A Feasibility Study

Andrei Manoliu, MD, PhD,[1,2]* Michael Ho, MD,[1] Marco Piccirelli, PhD,[3] Daniel Nanz, PhD,[1] Lukas Filli, MD,[1] Evelyn Dappa, MD,[1] Wei Liu, PhD,[4] Dominik A. Ettlin, MD, DMD,[5] Andreas Boss, MD, PhD,[1] Gustav Andreisek, MD, MBA,[1] and Felix P. Kuhn, MD, MAS[1]

Purpose: To assess the feasibility of diffusion tensor imaging (DTI) using simultaneous multislice (SMS) acquisition with blipped controlled aliasing in parallel imaging (CAIPI) for accelerated readout-segmented echo planar imaging (rs-EPI) of the mandibular nerves. DTI of the mandibular nerves using EPI is challenging due to susceptibility artifacts. Rs-EPI is less prone to artifacts but associated with longer scan durations.

Materials and Methods: Eight asymptomatic volunteers were imaged at 3T using a 64-channel head/neck coil. Conventional, 2-fold (2xSMS) and 3-fold (3xSMS) slice-accelerated rs-EPI sequences were acquired. Tractography of the mandibular nerves was performed. Signal-to-noise ratio (SNR), fractional anisotropy (FA), mean diffusivity (MD), and number of tracts were calculated. Artifacts were evaluated qualitatively on Likert scales. Parameters were compared statistically. Clinical feasibility of 2xSMS rs-EPI was tested in four patients.

Results: SNR was similar for conventional (mean $\pm$ SD; 8.55 ± 3.90) and 2xSMS rs-EPI (7.83 ± 3.15) but lower for 3xSMS rs-EPI (5.42 ± 2.93; analysis of variance, $P = 0.004$). FA was similar for all sequences (rs-EPI, 0.42 ± 0.08; 2xSMS rs-EPI, 0.43 ± 0.08; 3xSMS rs-EPI, 0.44 ± 0.06), while 3xSMS rs-EPI showed lower MD (rs-EPI, 0.0015 ± 0.0003; 2xSMS rs-EPI, 0.0014 ± 0.0001; 3xSMS rs-EPI, 0.0013 ± 0.0003) and lower number of tracts (rs-EPI, 66.56 ± 51.31; 2xSMS rs-EPI, 65.75 ± 55.40; 3xSMS rs-EPI, 37.93 ± 52.42) compared to rs-EPI and 2xSMS rs-EPI. Additionally, 2xSMS rs-EPI was feasible in four clinical patients and provided robust imaging results.

Conclusion: 2xSMS rs-EPI yielded similar SNR, FA, and MD values compared to conventional rs-EPI at reduced scan time and is feasible in clinical patients. These findings suggest the potential clinical applicability of rs-EPI for DTI of the mandibular nerve.

Level of Evidence: 2

J. MAGN. RESON. IMAGING 2017;00:000–000

The mandibular nerve is susceptible to traumatic[1] or iatrogenic injuries induced during block anesthesia,[2] root canal treatment,[3] removal of molar teeth,[4] and orthognathic surgery.[5] Traditionally, the evaluation of peripheral neural pathologies is mainly based on clinical and electrophysiological assessment.[7] However, due to methodological advances magnetic resonance imaging (MRI) has emerged as the method of choice to evaluate peripheral nerves (MR neurography, MRN)[8] as well as cranial nerves[9] over the last decades. In particular, MRN yields an accurate depiction of the morphology of the peripheral nerves under physiological and pathological conditions,[10–12] enhancing the diagnostic

View this article online at wileyonlinelibrary.com. DOI: 10.1002/jmri.25603

Received May 22, 2016, Accepted for publication Dec 5, 2016.

*Address reprint requests to: A.M. (current address), Department of Psychiatry, Psychotherapy and Psychosomatics, Psychiatric University Hospital Zurich, University of Zurich, Lenggstrasse 31, 8032 Zurich, Switzerland. E-mail: andrei.manoliu@puk.zh.ch

From the [1]Institute for Diagnostic and Interventional Radiology, Department of Radiology, University Hospital Zurich, University of Zurich, Zurich, Switzerland; [2]Psychiatric University Hospital, Department of Psychiatry, Psychotherapy and Psychosomatics, University of Zurich, Zurich, Switzerland; [3]Department of Neuroradiology, University Hospital Zurich, University of Zurich, Zurich, Switzerland; [4]Siemens Shenzhen Magnetic Resonance Ltd, Shenzhen, China; and [5]Center of Dental Medicine, University of Zurich, Zurich, Switzerland

accuracy and contributing to an improved clinical management.[13] Recently, diffusion-weighted imaging (DWI) and diffusion-tensor imaging (DTI) have been evaluated for MRI of the peripheral nerve system.[14] Despite the first promising imaging results in peripheral nerves, such as the ulnar,[15] median,[16,17] or tibial nerves,[18] as well as successful preliminary clinical applications,[19] DWI of the cranial nerves, including the mandibular nerve, is still challenging and requires further optimization.

One major challenge still limiting the application of DWI/DTI for evaluating the mandibular nerve are susceptibility artifacts due to local field inhomogeneities, especially within and around the oral cavity.[20,21] Generally used single shot spin echo planar imaging (ss-EPI) pulse sequences for diffusion tensor based neurography are based on whole *k*-space sampling after a single spin excitation and are therefore particularly sensitive to susceptibility artifacts.[22] In contrast, newly developed readout segmented EPI sequences (rs-EPI),[22] which have been successfully applied for diffusion imaging of the brain,[23,24] are less prone to susceptibility artifacts. In particular, rs-EPI sequences divide the *k*-space trajectory into multiple segments in the readout direction, which allows for an encoding-time reduction by shorter echo spacing and shorter echo-train duration compared to ss-EPI sequences, yielding a greater robustness regarding susceptibility artifacts.[22,25]

However, every readout segment in *k*-space requires a separate radiofrequency pulse; therefore, the improvement in image quality is associated with an increased acquisition time.[22,26] Recently, simultaneous multislice (SMS) acquisition based on the blipped controlled aliasing in parallel imaging (blipped-CAIPI) technique has been successfully used to significantly reduce the necessary scan duration for rs-EPI.[27,28] This new approach is assumed to enable a robust acquisition of DWI data of the mandibular nerve while maintaining an adequate scan time for clinical routine. Furthermore, this method was recently validated for diffusion imaging of peripheral nerves.[29]

The aim of the current study was to assess the feasibility of 2-fold (2xSMS) and 3-fold (3xSMS) accelerated SMS-rs EPI for DWI/DTI of the mandibular nerve and to compare the obtained fractional anisotropy (FA) and mean diffusivity (MD) values with conventional rs-EPI without acceleration.

Materials and Methods

The local Ethics Board approved the current prospective MRI study in asymptomatic volunteers. Written informed consent was obtained from all participants. The study was registered in the official research database of the University of Zurich, Switzerland. No financial support was provided by industry. One of the authors was an employee of Siemens Shenzhen Magnetic Resonance (Shenzhen, China). However, the other authors had full control of the data.

MRI

IMAGING PROTOCOL. MRI was performed on a 3T system (MAGNETOM Skyra, Siemens Healthcare, Erlangen, Germany) using a 64-channel head/neck coil (Siemens Healthcare). For anatomical characterization of the mandibular nerve, a 3D T_2-weighted (T_2w) SPACE (sampling perfection with application optimized contrasts using different flip angle evolution) sequence with STIR (short tau inversion recovery) fat suppression was acquired using the following parameters: repetition time (TR) = 4500 msec; echo time (TE) = 231 msec; field of view (FoV) (read/phase) = 240 mm / 70.3%; phase-encoding direction, right to left; matrix size = 256 × 180; slice thickness = 0.9 mm; effective resolution = 0.9 × 0.9 × 0.9 mm, total acquisition time, 9 minutes 23 seconds. For DWI/DTI of the mandibular nerve, a prototype sequence based on diffusion-weighted and readout-segmented echo planar imaging with simultaneous multislice excitation (SMS rs-EPI) was applied. In particular, the blipped-controlled aliasing in parallel imaging for simultaneous multislice echo planar imaging (blipped-CAIPI) technique was integrated into the rs-EPI sequence resulting in a blipped-CAIPI-based rs-EPI pulse sequence (SMS rs-EPI). In addition to the conventional rs-EPI, SMS rs-EPI sequences were applied with 2xSMS rs-EPI and 3xSMS rs-EPI slice acceleration. All sequence parameters were kept identical for all diffusion sequences except for the slice acceleration and resulting adjustments of TR and number of slices (for detailed imaging parameters, see Table 1). In addition, identical diffusion scans were performed subsequent to the aforementioned diffusion sequences for all volunteers to measure the noise and allow for the calculation of SNR.

VOLUNTEER IMAGING. For all volunteers, all sequences were acquired successively. To avoid a potential bias due to scanner drift or increasing movement during the examination, the order of the acquired diffusion sequences was chosen randomly for all volunteers.

Data Analysis

SNR MEASUREMENTS. SNR analysis followed the procedure described in full detail by Reeder et al[31] and applied by Filli et al for SNR evaluation in peripheral nerves.[29] Briefly, each diffusion sequence was acquired twice and difference images between the two aforementioned images were calculated. The SNR was defined as follows:

$$SNR = \frac{|\rho|}{\sigma} \times \sqrt{2}$$

where ρ is the magnitude of the detected transverse magnetization, ie, the signal intensity as measured on the b = 0 image, σ is the standard deviation of the corresponding noise components as measured on the difference image, and $\sqrt{2}$ is a correction factor.[29,31–33] First, SNR was calculated on a voxel-wise basis. Image data and corresponding noise data were postprocessed individually, yielding voxel-based SNR maps. Subsequently, two readers (A.M. and M.J.H.) placed a region of interest (ROI) covering each mandibular nerve at the level of the retromandibular triangle and corresponding SNR values were extracted. This procedure resulted in

TABLE 1. Scan Parameters of the Readout-Segmented Echo-Planar Imaging Sequences With Different Slice Acceleration Factors

	Conventional rs-EPI	2xSMS rs-EPI	3xSMS rs-EPI
Number of slices	56	56	57
TR [msec]	8940	4470	3090
TE [msec]	71	71	71
Flip angle [degree]	180	180	180
Bandwidth [Hz/Px]	919	919	919
Fat suppression	Fat sat.	Fat sat.	Fat sat.
Number of diffusion directions	12	12	12
Number of readout segments	5	5	5
b-value [s mm-2]	0/1000	0/1000	0/1000
FoV read [mm]	240	240	240
FoV phase [%]	100	100	100
Phase encoding dir.	A > > P	A > > P	A > > P
Matrix size	160 × 160	160 × 160	160 × 160
Slice thickness [mm]	1,5	1,5	1,5
Effective resolution [mm]	1.5 × 1.5 × 1.5	1.5 × 1.5 × 1.5	1.5 × 1.5 × 1.5
Averages	1	1	1
Partial Fourier	7/8 (readout)	7/8 (readout)	7/8 (readout)
iPAT accel. factor	2	2	2
Slice acceleration factor	1	2	3
Total scan time	18:21 min	9:34 min	6:46 min

rs-EPI, readout-segmented echo planar imaging; SMS, simultaneous multislice acquisition; iPAT, integrated parallel acquisition technique; TR, repetition time; TE, echo time, FoV, field of view; TR, repetition time; TE, echo time.

one SNR value for each mandibular nerve and reader. Therefore, the statistical evaluation of potential differences in SNR between sequences was performed for each side and reader, individually (see below). For all following SNR correction steps, SNR values for both readers and sides were concatenated for each volunteer.

SNR CORRECTION DUE TO SEQUENCE-SPECIFIC DIFFERENCES IN ACQUISITION TIME. To determine the SNR efficiency of a particular acquisition scheme, the measured SNR was divided by the square root of the respective acquisition time:

$$SNR(TA) = \frac{SNR}{\sqrt{TA}}$$

where TA is the total acquisition duration (29).

QUANTITATIVE DIFFUSION ANALYSIS. Quantitative analysis of the acquired diffusion data was performed using the syngo.via Neuro 3D tool (v. 3.0, Siemens Healthcare). First, tractography of each mandibular nerve was performed by placing an ROI on each side covering the mandibular canal at the level of the retromandibular triangle. Tracts were generated using the following parameters: minimal tract length = 40 mm, angle threshold 30°, fractional anisotropy threshold 0.2.[29] Subsequently, the following measurements were extracted for each volunteer and side, respectively: 1) number of generated fiber tracts, 2) FA values, 3) MD values.

QUALITATIVE IMAGE EVALUATION. All acquired images were anonymized (subject's initials blinded) and saved in the hospitals picture archiving and communication system (PACS; Impax 6.0, Agfa Healthcare, Mortsel, Belgium). Subsequently, two blinded fellowship-trained radiologists assessed the images independently (A.M. and M.J.H.) with respect to artifacts and overall image quality. In particular, the following parameters were assessed: 1) artifacts due to image distortion, ghosting and motion using a 4-point Likert scale (0, none; 1, low; 2, moderate; 3, high); 2) Grading of the anatomical delineation of the mandibular nerve (0, <50%; 1, 50–75%; 2, 75–90%; 3, >90%); 3) overall image quality using a 5-point Likert scale ranging from 1 to 5 (1, excellent; 2, good; 3, moderate; 4, poor; 5, complete lack of diagnostic information).

Assessment of Feasibility in Clinical Subjects

In order to assess the feasibility of the simultaneous multislice excitation technique in a clinical context, we acquired DTI data with 2-fold (2xSMS) slice-accelerated rs-EPI sequences in four consecutive patients using the identical sequence parameters for 2xSMS rs-

EPI stated in Table 1. Additionally, the following sequences were performed to provide morphological MR-images according to[30]: 1) 3D UTE PETRA (pointwise encoding time reduction with radial acquisition) single echo sequence (Quiet-Suite, Siemens Healthcare) using the following parameters: TR = 3.61 msec, TE = 0.07 msec, flip angle = 6°, bandwidth = 359 Hz/Px, FoV read = 300 mm, FoV phase = 100%, matrix size = 320 × 320, slice thickness = 0.9 mm, effective resolution = 0.9 × 0.9 × 0.9 mm, averages = 1, acquisition time = 4:56 min; 2) 3D diffusion-weighted reversed fast imaging with steady state precession (3D-PSIF) with inherent vascular signal suppression using following parameters: TR = 11.31 msec, TE = 3.76 msec, flip angle = 30°, bandwidth = 230 Hz/Px, fat suppression = water excitation, b-value = 85 s*mm^{-2}, FoV read- = 240 msec, FoV phase = 100%, matrix size = 256 × 256, slice thickness = 0.9 mm, effective resolution = 0.9 × 0.9 × 0.9 mm, averages = 1, acquisition time = 4:16 min; 3) 3D T_2w SPACE sequence with STIR fat suppression using the following parameters: TR = 4500 msec, TE = 231 msec, flip angle = various; bandwidth = 454 Hz/Px, fat suppression = STIR (TI, 230 msec), FoV read = 240 mm, FoV phase = 70.3%, matrix size = 256 × 180, slice thickness = 0.9 mm, effective resolution = 0.9 × 0.9 × 0.9 mm, averages = 1.7, partial Fourier = 6/8 (slice), acceleration factor = 2, acquisition time = 9:23 minutes. Regarding subsequent analysis, the tractography parameters corresponded to tract lengths of 40–400 mm, two seed points per voxel length, a 30° angle threshold, and a 0.2 FA threshold. The applied ROIs included the inferior alveolar nerve (IAN) at the level of the mandibular angle and close to the mandibular foramen with an ROI size adapted to the nerve diameter on the overlaid T_2w images.

Statistical Analysis

All statistical analyses were performed using SPSS (release 22.0, Chicago, IL). Interreader agreement was assessed by calculating the intraclass correlation coefficients (ICCs) for SNR, FA, MD, and number of tracts and by calculating Cohen's kappa for the artifact scores, delineation of the mandibular nerve, and the overall image quality. Cohen's kappa values were interpreted according to Landis and Koch,[34] and ICC values according to Kundel and Polanski.[35] Normal distribution of SNR, FA, MD, and number of tracts was evaluated using the Shapiro–Wilk's test (significance level $\alpha = 0.05$). To assess potential between-group effects, analysis of variance (ANOVA) was performed for interval-scaled variables (SNR, FA, MD, number of tracts) and Friedman tests were performed for ordinal-scaled variables (artifacts scores, delineation of the mandibular nerve, overall image quality). To evaluate potential differences between conventional rs-EPI and 2xSMS rs-EPI, conventional SMS rs-EPI and 2xSMS rs-EPI as well as 2xSMS rs-EPI and 3xSMS rs-EPI, post-hoc two-sample *t*-tests were performed for interval-scaled variables (SNR, FA, MD, number of tracts) and post-hoc Wilcoxon signed-rank tests were performed for ordinal-scaled variables (artifacts scores, delineation of the mandibular nerve, overall image quality). All statistical tests were Bonferroni-corrected for multiple comparisons (significance level $\alpha = 0.05$).

Results

Eight healthy asymptomatic volunteers were included in the current study (five women, mean age 22.9 years, range, 20–50 years and three men, mean age 26.6 years, range 26–27 years). Participants' data were partially used in a previous study investigating the feasibility of ultrashort echo time sequences for obtaining an MR-based orthopantomogram of the jaw.[30] Inclusion criterion was willingness to participate in this study. Exclusion criteria were current or past systemic neurological disorder, acute or chronic sensory disorders, painful dysesthesias, pregnancy, claustrophobia, and metallic and dental implants, particularly retainers. Dental filling or tooth crown were not exclusion criteria. No contrast agent was administered in this study. All images were successfully acquired. Specific absorption rate (SAR) remained below individual limits in all sequences. None of the subjects reported having voluntarily or accidentally opened the mouth during the scans.

SNR Analysis

The interobserver reliability (ICC) was 0.078 for conventional rs-EPI, 0.898 for 2xSMS rs-EPI, and 0.972 for 3xSMS rs-EPI. SNR yielded normal distribution for both readers and all sequences (R1, $P \geq 0.257$; R2, $P \geq 0.087$). Measured SNR decreased with increasing acceleration for both readers (see Table 2 for detailed presentation of the SNR characteristics for both readers and all sequences and Fig. 1 for voxelwise SNR maps for all diffusion sequences). ANOVA revealed no statistically significant group effect between all sequences after correction for multiple comparisons for both readers. However, post-hoc analysis revealed significantly lower SNR for 3xSMS rs-EPI compared to conventional rs-EPI for both readers (R1, $P = 0.048$, R2, $P = 0.006$, Bonferroni-corrected for multiple comparisons) and reduced SNR compared to 2xSMS rs-EPI for reader 1 (R1, $P = 0.005$; R2, $P = 0.085$, Bonferroni-corrected for multiple comparisons) (Table 2). When concatenating all data across readers and sides, ANOVA yielded a statistically significant group effect ($P = 0.004$). Furthermore, post-hoc analysis yielded significantly lower SNR for 3xSMS rs-EPI compared to conventional rs-EPI ($P < 0.001$) and 2xSMS rs-EPI ($P = 0.001$). To account for sequence-specific differences in scan duration, correction factors were calculated for the acquisition time (see Table 3). Regarding SNR-values corrected for the acquisition time, 2xSMS rs-EPI yielded significantly higher SNR compared to conventional and 3xSMS rs-EPI (see Table 3).

Quantitative Diffusion Analysis

Tractography was feasible in all volunteers for all sequences except for one volunteer using 3xSMS rs-EPI (Fig. 2). After tractography was performed, FA and MD values were extracted. In addition, the number of generated tracts was counted for each mandibular nerve. Interobserver reliability (ICC) ranged from 0.751–0.929 for FA, 0.914–0.967 for MD, and 0.966–0.974 for the number of generated tracts

TABLE 2. Signal-to-Noise Ratio (SNR) Analysis

	rs-EPI	2x SMS rs-EPI	3x SMS rs-EPI	ANOVA		rs-EPI vs. 2x SMS rs-EPI		rs-EPI vs. 3x SMS rs-EPI		2 × SMS rs-EPI vs. 3x SMS rs-EPI	
	mean ± SD	mean ± SD	mean ± SD	*P* (uncorrected)	*P* (corrected)	*P* (uncorrected)	*P* (corrected)	*P* (uncorrected)	*P* (corrected)	*P* (uncorrected)	*P* (corrected)
Reader 1											
Left	8.588 ± 5.825	7.804 ± 3.570	5.521 ± 3.278	0.364	1.092	0.692	1.000	0.170	0.510	0.084	0.252
Right	8.325 ± 2.484	7.923 ± 2.316	5.338 ± 2.469	0.046	0.138	0.766	1.000	0.046	0.138	0.005	0.016*
Bilateral	8.456 ± 4.328	7.863 ± 2.908	5.429 ± 2.805	0.038	0.114	0.602	1.000	0.016	0.048*	0.002	0.005*
Reader 2											
Left	8.751 ± 4.601	7.775 ± 4.563	5.429 ± 3.712	0.306	0.917	0.577	1.000	0.062	0.185	0.249	0.746
Right	8.555 ± 2.457	7.838 ± 2.234	5.395 ± 2.752	0.047	0.142	0.354	1.000	0.014	0.042*	0.022	0.065
Bilateral	8.653 ± 3.565	7.806 ± 3.471	5.412 ± 3.157	0.027	0.082	0.351	1.000	0.002	0.006*	0.028	0.085

For each sequence and reader, SNR values are given as mean ± standard deviation. ANOVA and post-hoc paired-sample *t*-tests were performed to assess potential between-group differences. Corresponding *P*-values are given uncorrected as well as Bonferroni-corrected for multiple comparisons ($n = 3$). Asterisks indicate corrected *P*-values < 0.05. rs-EPI, readout-segmented echo planar imaging; SMS, simultaneous multislice acquisition.

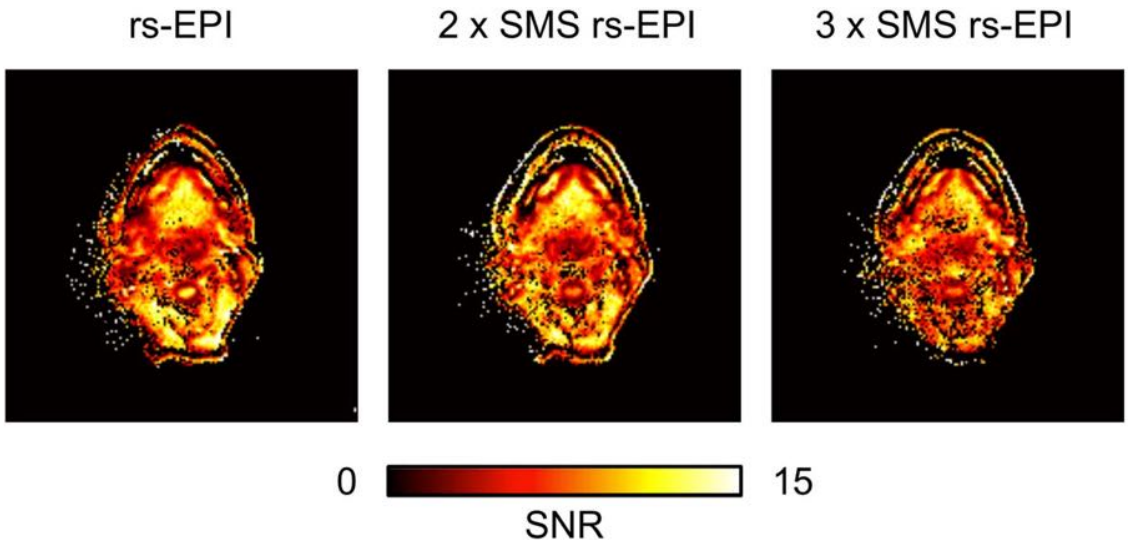

FIGURE 1: Voxelwise SNR maps for the readout-segmented echo-planar imaging sequences with different slice acceleration factors. SNR was calculated on a voxelwise basis. Image data and corresponding noise data were postprocessed individually, yielding voxel-based SNR maps. SNR maps for the same asymptomatic volunteer are demonstrated using conventional rs-EPI, 2xSMS rs-EPI, and 3xSMS rs-EPI, respectively. Compared to conventional rs-EPI, 2xSMS rs-EPI yielded similar SNR in the mandibular nerve, while 3xSMS rs-EPI yielded lower SNR. SNR values are color-coded from 0 (black) to 25 (yellow/white). rs-EPI, readout-segmented echo planar imaging; SMS, simultaneous multislice acquisition.

for all sequences. Normal distribution was given for all sequences and both readers regarding FA (R1, $P \geq 0.114$; R2, $P \geq 0.168$), MD (R1, $P \geq 0.264$; R2, $P \geq 0.264$), and the number of tracts (R1, $P \geq 0.069$; R2, $P \geq 0.068$). After Bonferroni-correction for multiple comparisons, ANOVA yielded a significant group effect for MD for reader 2 (R1, $P = 0.107$, R2, $P = 0.006$, Table 4). Post-hoc analysis yielded lower MD for 3xSMS rs-EPI compared to conventional rs-EPI for reader 2 (R1, $P = 0.057$; R2, $P = 0.006$) and 2xSMS rs-EPI (R1, $P = 1.192$; R2, $P = 0.036$, see Table 4). In addition, analysis yielded a trend towards lower number of tracts for 3xSMS rs-EPI compared to conventional and 2xSMS rs-EPI for both readers. however, the results lost significance after correction for multiple comparison (Table 4). No significant differences between groups were found for FA.

Qualitative Analysis

Interobserver reliability (Cohen's kappa) ranged from 0.60–0.758 for the artifact scores, 0.60–0.81 for the delineation of the mandibular nerve, and 0.71–0.81 for the overall image quality for all three sequences.

In general, artifact scores were rated higher with increased acceleration for both readers. In particular, Friedman test revealed a significant between-group effect for reader 1 ($P = 0.015$) and a trend towards significant between-group effect for reader 2 ($P = 0.059$; see Table 5 and Fig. 3). For reader 1, post-hoc analysis revealed significant higher artifact scores for 3xSMS rs-EPI compared to conventional rs-EPI for reader 1 (R1, $P = 0.034$; R2, $P = 0.059$) and 2xSMS rs-EPI (R1, $P = 0.046$; R2, $P = 0.063$). No significant differences were found between 2xSMS rs-EPI and conventional rs-EPI for either reader. Regarding the delineation of the left and right mandibular nerve, statistical analysis revealed a significant group effect for reader 2 (left side: R1, $P = 0.223$; R2, $P = 0.037$; right side: R1, $P = 0.368$; R2, $P = 0.050$). Post-hoc analysis yielded no significant difference between the different diffusion sequences (Table 5). Overall image quality showed a tendency towards decreasing with increased slice acceleration. Statistical analysis revealed a statistically significant between-group effect for reader 2 (R1, $P = 0.061$; R2, $P = 0.023$). However, post-hoc analysis did not yield a statistically significant difference between the different diffusion sequences (Table 5).

Clinical Application

Patient 1 (age 41 years; mean FA [right/left IAN] = 0.44/0.46; mean MD [right/left IAN] = 0.0013/0.0014) suffered from chronic intermittent pain in the left lower mandible. Morphological MRN was considered within normal limits (Fig. 4A). Patient 2 (age 33 years; mean FA [right/left IAN] = 0.45/0.43; mean MD [right/left IAN] = 0.0014/0.0016) had chronic pain on the left side after a fracture of the mandible. MRN showed a corresponding focal posttraumatic neuroma at the level of the left mandibular angle (Fig. 4B). Patient 3 (age 36 years; mean FA [right/left IAN] = 0.45/0.45; mean MD [right/left IAN] = 0.0014/0.0015) reported recurrent fulminant pain on the left side in relation to chewing. The acquired cone-beam computed tomography images elicited a focal osteolytic lesion below the root of tooth 36 with focal thinning of the adjacent

TABLE 3. Corrected Signal-to-Noise Ratio (SNR) Analysis

	rs-EPI	2 × SMS rs-EPI	3 × SMS rs-EPI
Correction for acquisition time			
Square root of acquisition time [s]	33.18	23.95	20.14
Correction factor	1	1.3854	1.6475

Statistical analysis

SNR values after correction for acquisition time				ANOVA		rs-EPI vs. 2 × SMS rs-EPI		rs-EPI vs. 3 × SMS rs-EPI		2 × SMS rs-EPI vs. 3 × SMS rs-EPI	
	Mean ± SD	Mean ± SD	Mean ± SD	*P* (uncorrected)	*P* (corrected)	*P* (uncorrected)	*P* (corrected)	*P* (uncorrected)	*P* (corrected)	*P* (uncorrected)	*P* (corrected)
SNR (measured)	8.555 ± 3.902	7.835 ± 3.150	5.421 ± 2.938	0.001	0.004*	0.31	1	0	0.000*	0	0.001*
SNR (corrected for acquisition time)	8.555 ± 3.902	10.854 ± 4.364	8.930 ± 4.840	0.085	0.34	0.008	0.032*	0.676	1	0.035	0.14

Measured SNR was concatenated for both sides and readers and corrected for the sequence-specific differences regarding the acquisition time. For each sequence, corrected SNR values are given as mean ± standard deviation. ANOVA and post-hoc paired-sample *t*-tests were performed to assess potential between-group differences. Corresponding *P*-values are given uncorrected as well as Bonferroni-corrected for multiple comparisons ($n = 4$). Asterisks indicate corrected *P*-values < 0.05. rs-EPI, readout-segmented echo planar imaging; SMS, simultaneous multislice acquisition.

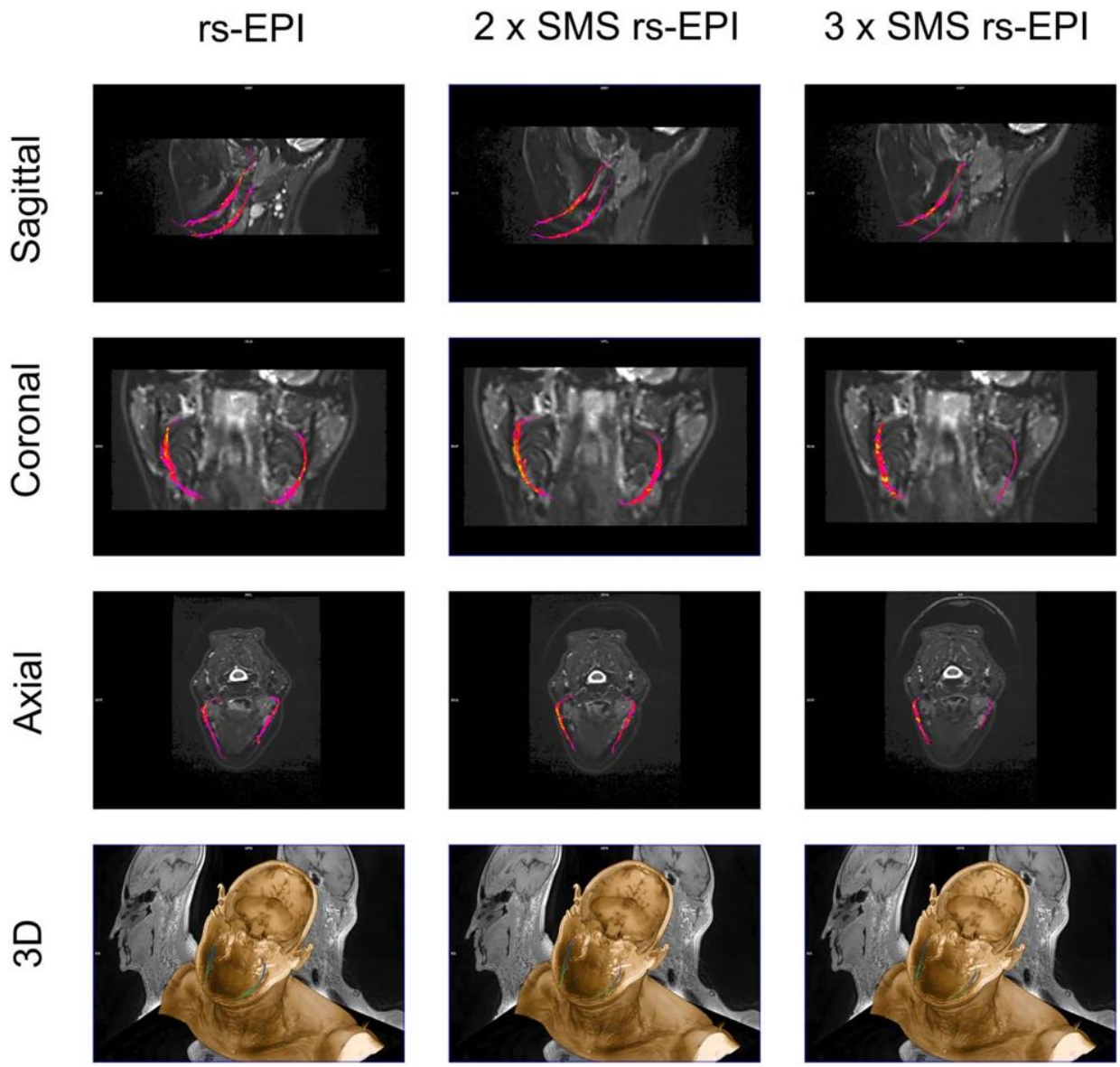

FIGURE 2: Tractography results for the readout-segmented echo-planar imaging sequences with different slice acceleration factors. Tractography was performed by placing an ROI on each side covering the mandibular canal at the level of the retromandibular triangle. Tractography results for the same asymptomatic volunteer are demonstrated using conventional rs-EPI, 2xSMS rs-EPI, and 3xSMS rs-EPI in sagittal, coronal, and axial orientations. Furthermore, a 3D reconstruction is shown for all accelerations. Compared to conventional rs-EPI, 2xSMS rs-EPI yielded similar number of tracts, while 3xSMS rs-EPI yielded lower number of tracts. It is noted that tractography was not feasible in one out of eight volunteers using 3xSMS rs-EPI. rs-EPI, readout-segmented echo planar imaging; SMS, simultaneous multislice acquisition.

cortical envelope of the mandibular canal. The morphologic MR images classified the tissue within the lesion as fat (Fig. 4C). Patient 4 (age 35 years; mean FA [right/left IAN] = 0.43/0.43; mean MD [right/left IAN] = 0.0011/0.0014) was referred for an incidental finding of a large intraosseous cyst in a previously acquired orthopantomogram. MRN revealed that the IAN was intact but displaced posteriorly and laterally (Fig. 4D). All acquired DTI datasets were qualitatively superimposable to the image quality found in the previously described healthy volunteers.

Discussion

To evaluate the feasibility of 2xSMS and 3xSMS rs-EPI for DWI/DTI of the mandibular nerve, we assessed quantitative data by means of FA, MD, number of tracts, and SNR for each mandibular nerve and qualitative data by means of axial DWI images in eight healthy volunteers. We found that 2xSMS rs-EPI yielded similar FA, MD, number of tracts, and SNR as well as similar artifact scores compared to conventional rs-EPI, while 3xSMS rs-EPI yielded lower SNR, lower number of tracts, and higher artifact scores compared

TABLE 4. Quantitative Diffusion Analysis

	rs-EPI	2x SMS rs-EPI	3x SMS rs-EPI	ANOVA		rs-EPI vs. 2x SMS rs-EPI		rs-EPI vs. 3x SMS rs-EPI		2 × SMS rs-EPI vs. 3x SMS rs-EPI	
	mean ± SD	mean ± SD	mean ± SD	*P* (uncorrected)	*P* (corrected)	*P* (uncorrected)	*P* (corrected)	*P* (uncorrected)	*P* (corrected)	*P* (uncorrected)	*P* (corrected)
Reader 1											
FA											
Left	0.403 ± 0.086	0.413 ± 0.065	0.438 ± 0.042	0.343	1.000	0.668	1.000	0.263	0.789	0.479	1.000
Right	0.429 ± 0.078	0.439 ± 0.093	0.437 ± 0.074	0.944	1.000	0.770	1.000	0.315	0.946	0.723	1.000
Bilateral	0.416 ± 0.080	0.426 ± 0.078	0.437 ± 0.057	0.746	1.000	0.613	1.000	0.136	0.408	0.536	1.000
MD											
Left	0.0015 ± 0.0030	0.0015 ± 0.0001	0.0012 ± 0.0003	0.072	0.216	0.565	1.000	0.145	0.436	0.147	0.441
Right	0.0015 ± 0.0003	0.0014 ± 0.0002	0.0013 ± 0.0001	0.426	1.000	0.286	0.859	0.026	0.079	0.151	0.454
Bilateral	0.0015 ± 0.0003	0.0014 ± 0.0001	0.0013 ± 0.0003	0.036	0.107	0.225	0.675	0.019	0.057	0.064	0.192
Number of tracts											
Left	70.75 ± 54.83	70.25 ± 64.85	34.29 ± 49.80	0.167	0.500	0.977	1.000	0.229	0.686	0.097	0.292
Right	62.38 ± 50.93	61.25 ± 48.22	41.57 ± 58.67	0.393	1.000	0.921	1.000	0.295	0.885	0.219	0.658
Bilateral	66.56 ± 51.31	65.75 ± 55.40	37.93 ± 52.42	0.263	0.790	0.935	1.000	0.090	0.270	0.030	0.089
Reader 2											
FA											
Left	0.404 ± 0.068	0.429 ± 0.057	0.442 ± 0.047	0.343	1.000	0.268	0.804	0.237	0.710	0.660	1.980
Right	0.437 ± 0.026	0.435 ± 0.068	0.437 ± 0.074	0.972	1.000	0.667	1.000	0.634	1.000	0.801	2.404
Bilateral	0.421 ± 0.053	0.432 ± 0.061	0.440 ± 0.058	0.662	1.000	0.468	1.000	0.253	0.759	0.912	2.736
MD											
Left	0.0015 ± 0.0003	0.0014 ± 0.0002	0.0010 ± 0.0006	0.074	0.222	0.210	0.630	0.049	0.147	0.100	0.300
Right	0.0015 ± 0.0003	0.0015 ± 0.0001	0.0010 ± 0.0005	0.031	0.093	0.815	1.000	0.036	0.108	0.083	0.249
Bilateral	0.0015 ± 0.0003	0.0014 ± 0.0001	0.0010 ± 0.0006	0.002	0.006*	0.225	0.675	0.002	0.006*	0.012	0.036*
Number of tracts											
Left	71.13 ± 46.50	69.13 ± 62.19	32.86 ± 41.00	0.114	0.343	0.727	1.000	0.369	1.000	0.151	0.452
Right	65.00 ± 46.02	63.38 ± 48.59	42.67 ± 49.10	0.346	1.000	0.891	1.000	0.127	0.381	0.057	0.170
Bilateral	68.06 ± 44.80	66.25 ± 53.99	37.38 ± 43.25	0.179	0.537	0.846	1.000	0.033	0.100	0.019	0.057

For each sequence and reader, FA, MD, and number of tracts are given as mean ± standard deviation. ANOVA and post-hoc paired-sample *t*-tests were performed to assess potential between-group differences. Corresponding *P*-values are given uncorrected as well as Bonferroni-corrected for multiple comparisons ($n = 3$). Asterisks indicate corrected *P*-values < 0.05. rs-EPI, readout-segmented echo planar imaging; SMS, simultaneous multislice acquisition; FA, fractional anisotropy; MD, mean diffusivity

TABLE 5. Qualitative Analysis

	rs-EPI	2x SMS rs-EPI	3x SMS rs-EPI	Friedman	rs-EPI vs. 2x SMS rs-EPI	rs-EPI vs. 3x SMS rs-EPI	2 × SMS rs-EPI vs. 3x SMS rs-EPI
	mean ± SD	mean ± SD	mean ± SD	*P*-values			
Reader 1							
Artifacts	1,63 ± 0,52	1,88 ± 0,35	2,38 ± 0,52	0,015*	0,157	0,034*	0,046*
Delineation left mandibular nerve	1,25 ± 0,46	1,50 ± 0,76	1,75 ± 0,89	0,223	0,317	0,157	0,317
Delineation right mandibular nerve	1,50 ± 0,76	1,50 ± 0,76	1,75 ± 0,89	0,368	1,000	0,317	0,317
Overall image quality	1,25 ± 0,46	1,38 ± 0,52	1,88 ± 0,83	0,061	0,317	0,102	0,102
Reader 2							
Artifacts	1,75 ± 0,46	1,75 ± 0,46	2,50 ± 0,76	0,059	1,000	0,059	0,063
Delineation left mandibular nerve	1,13 ± 0,35	1,38 ± 0,52	1,88 ± 0,83	0,037*	0,157	0,063	0,102
Delineation right mandibular nerve	1,38 ± 0,52	1,38 ± 0,52	1,88 ± 0,83	0,05*	1,000	0,102	0,102
Overall image quality	1,38 ± 0,52	1,25 ± 0,46	2,13 ± 0,83	0,023*	0,317	0,063	0,059

For each sequence and reader, scores for artifacts, delineation of the left/right mandibular nerve and overall image quality are given as mean ± standard deviation. Friedman tests and post-hoc Wilcoxon signed-rank tests were performed to assess potential between-group differences. Corresponding *P*-values are given. Asterisks indicate *P*-values < 0.05. rs-EPI, readout-segmented echo planar imaging; SMS, simultaneous multislice acquisition.

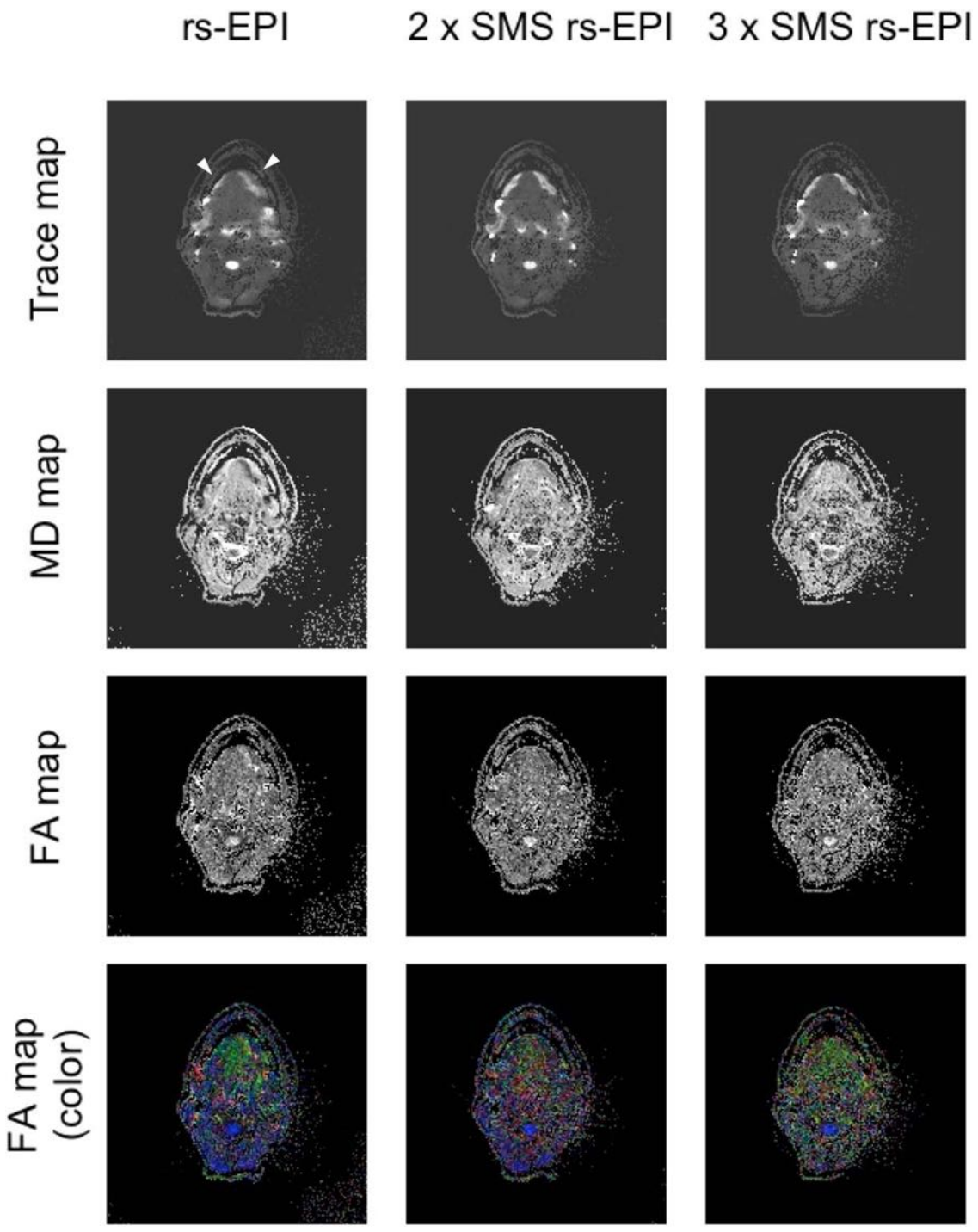

FIGURE 3: Diffusion maps for the readout-segmented echo-planar imaging sequences with different slice acceleration factors. Trace maps (depicting the sum of the three diffusion eigenvalues), MD (mean diffusivity) maps, and FA (fractional anisotropy) maps are shown for the same asymptomatic volunteer using conventional rs-EPI, 2xSMS rs-EPI, and 3xSMS rs-EPI. The left and right mandibular nerves can be depicted on all demonstrated maps and are indicated exemplarily in the upper-left trace map (white arrows).

to the conventional rs-EPI as well as 2xSMS rs-EPI. Therefore, the current results demonstrate that DWI/DTI imaging of the mandibular nerve using accelerated SMS rs-EPI is feasible and can be robustly performed with a 2-fold acceleration.

The SNR measured in the mandibular nerve was within the range of the current literature for peripheral nerves.[29,36] In general, measured SNR was decreasing with increased slice acceleration. In particular, 3-fold-accelerated rs-EPI yielded lower SNR compared to conventional and 2-fold-accelerated rs-EPI. This effect was observed for both readers.

SNR depends on a number of factors, including the spatial resolution and sequence-specific parameters, such as

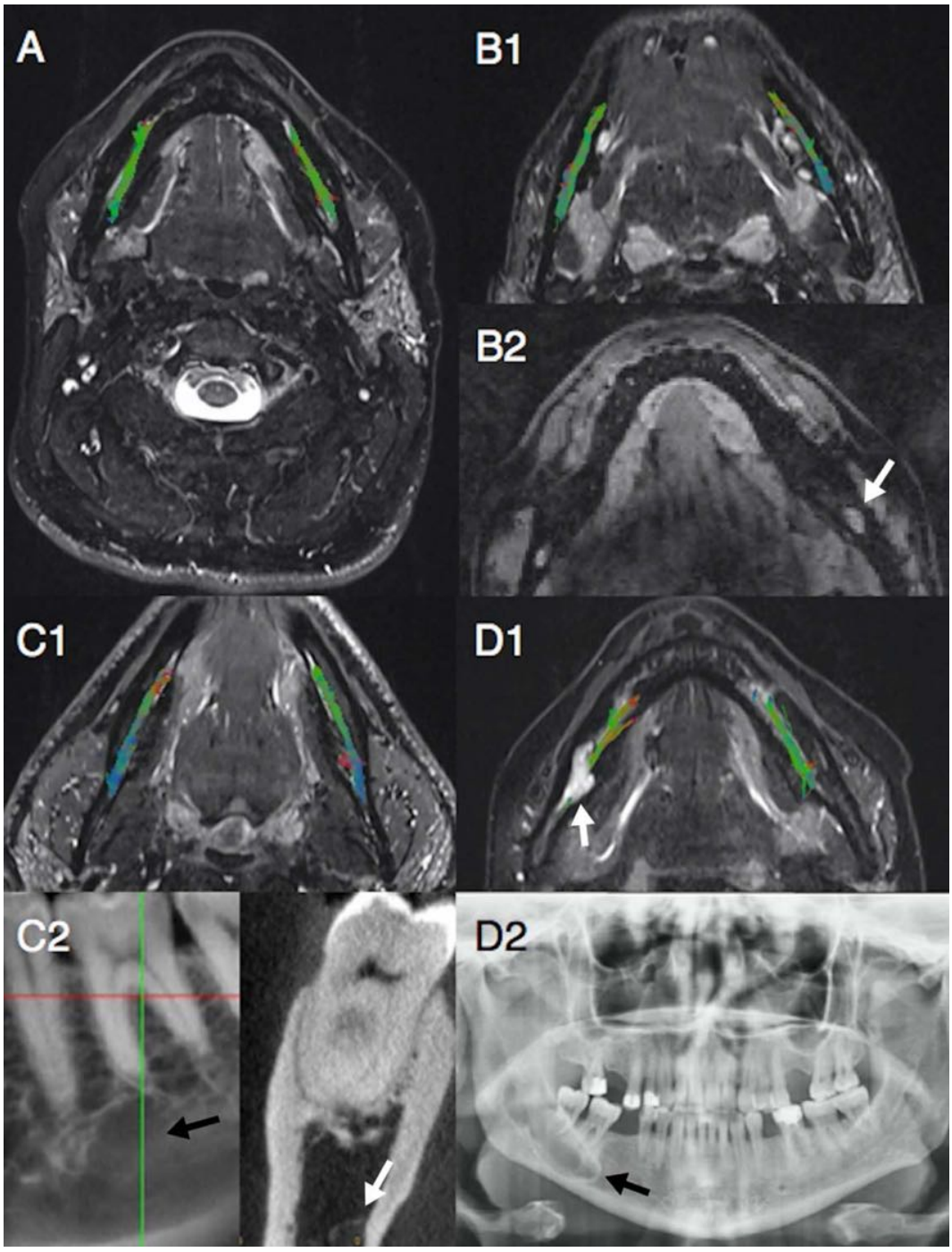

FIGURE 4: Clinical application and multimodal correlation of tractography in four patients. A: Tractography of the inferior alveolar nerve (IAN) in a patient with chronic pain in the left lower mandible. Morphological MRN was considered within normal limits (not shown). B1: Tractography of the IAN in a patient with chronic pain on the left side after a fracture of the mandible. B2: The 3D-PSIF pulse sequence (reversed fast imaging with steady state precession) used for MRN showed a focal neuroma at the level of the left mandibular angle (arrow). C1: Tractography of the IAN in a patient with pain on the left side during chewing. C2: The cone-beam computed tomography images elicited a focal osteolytic lesion below the root of tooth 36 (black arrow) with focal thinning of the adjacent cortical envelope of the mandibular canal (white arrow). The morphologic MR images classified the tissue within the lesion as fat (images not shown). D1: Tractography of the IAN in an asymptomatic patient with an incidental finding of a large intraosseous cysts (white arrow). D2: Orthopantomography showing this large cystic lesion on the right side (black arrow). The IAN is displaced posteriorly and laterally.

TE and TR. In particular, the SNR is positively correlated with the voxel size and the TR and negatively correlated with the TE. Therefore, reducing the TR is assumed to decrease the SNR.[32] In our current study, the SNR was compared between three diffusion sequences with different acceleration factors, and thus different acquisition times.

Noteworthy, TR was adjusted with respect to the acceleration, resulting in decreasing TR with increased acceleration. Given the identical spatial resolution, bandwidth, and TE for the different sequences, theoretical accounts suggest that increased acceleration will decrease the measured SNR, which is in line with the current results. Furthermore, the lower distance between excited slices might hamper their separation, additionally compromising the SNR.[29] When correcting for different acquisition times, 2xSMS rs-EPI yielded significantly higher SNR efficiency than conventional rs-EPI. This, of course, might be explained in part by a higher signal fluctuation due to the longer acquisition time and some more motion artifacts, compromising the SNR efficiency for conventional rs-EPI. However, 3xSMS rs-EPI yielded similar SNR efficiency compared to conventional rs-EPI and lower SNR efficiency compared to 2xSMS rs-EPI. In the current study, we used a 64-channel head-neck coil, which has not been optimized for high simultaneous multislice acceleration factors. In particular, a g-factor penalty (ie, noise amplification associated with the image reconstruction procedure due to lacking distinct spatial information in the receive coil sensitivity profiles[37] might have had a negative effect on the SNR efficiency at 3-fold acceleration. One approach to overcome this effect might be the design of close-fitting surface coils[38] consisting of at least three receive elements for each side of the mandible. However, further studies are needed to evaluate whether multielement surface coils indeed might provide higher SNR efficiency for rs-EPI at acceleration factors higher than two.

Several other approaches assumed to increase the SNR have been limited in the current study due to the complex structure of the mandibular nerve: 1) decreasing the spatial resolution (ie, decreasing the matrix size while keeping the FoV constant) would have impaired tractography due to partial-volume effects; 2) increasing the number of signal averages and/or using additional diffusion encoding directions would have significantly extended the scan duration, which in turn might have increased the risk of motion artifacts, to which the mandibular nerve is especially susceptible.

In the present study, tractography was feasible in all volunteers using conventional rs-EPI and yielded quantitative diffusion parameters in line with the literature.[17,39–41] Two-fold-accelerated rs-EPI yielded comparable performance, but 3xSMS EPI yielded a lower number of tracts. In addition, tractography was not feasible in one out of eight volunteers when performing 3xSMS rs-EPI. This observation might be attributed to decreasing SNR with increasing acceleration, which might limit the accuracy of voxelwise tensor calculation.

In general, FA values were not significantly different between all three sequences. However, in the current study FA values showed a trend towards higher values with increased slice acceleration. This observation has been described,[42] but a stringent explanation is still missing.[29] Measured MD values were similar for conventional rs-EPI and 2xSMS rs-EPI, but lower for 3xSMS rs-EPI (Table 4). Since in peripheral nerves FA is assumed to represent the microstructural integrity while MD is assumed to represent the inverse measure of the density of the axonal membrane,[43] this observation might also be explained by the phenomena causing increased FA for increased slice acceleration (see above). Taken together, considering all factors potentially modulating the FA and MD values as well as their possible interactions is very challenging and requires further systematic research. Nevertheless, the present study suggests that 2-fold-accelerated rs-EPI yields a similar performance when compared to conventional rs-EPI, while 3xSMS rs-EPI seems to systematically provide altered quantitative measurements.

Evaluation of the qualitative parameters showed a tendency towards increased artifacts, decreased delineation of the bilateral mandibular nerve, and decreased overall image quality with increased slice acceleration. It is noted, however, that post-hoc analyses revealed that those effects are mostly explained by a lower performance of 3xSMS EPI, while 2xSMS rs-EPI provided similar qualitative results when compared to conventional EPI. Although 3xSMS rs-EPI requires considerably lower scan durations, which might decrease artifacts and thus increase overall image quality, the aforementioned drop in SNR might have caused a general loss of image quality.

To assess the feasibility of the simultaneous multislice excitation technique in a small number of patients, an acquisition of DTI data with an acceleration factor of two (2xSMS) was added to our established MRN protocol of the mandibular nerve. The DTI data were qualitatively robust and quantitatively within the range of previously reported values in peripheral MRN. The quantitative DTI values, particularly FA and MD, will be assessed and related to clinical findings in a larger study cohort to determine the reliability of these functional MRN parameters in a clinical context.

Regarding further potential applications in clinical neurography, the presented technique might be used to investigate pathologies of other delicate neuronal structures in patients in vivo. For example, accelerated rs-EPI might improve the detection of microstructural abnormalities of the trigeminal nerve in patients with trigeminal neuralgia with[44] and without neurovascular compression.[45] Furthermore, the presented technique might enable the assessment and preoperative visualization of the facial and/or cochlear nerve in patients with malignant pathologies.[46,47] In general, the obtained gain in SNR over time might be either invested in accelerated scan time or other parameters, such as increased spatial resolution, allowing a flexible adaptation

depending on the clinical context. Therefore, accelerated rs-EPI yields a promising clinical potential, which should be examined in future studies investigating pathologies of further cranial nerves.

We acknowledge several limitations of the current study. 1) Sample size. Only eight healthy volunteers were included in the present study. Our sample size is similar to other feasibility studies.[29] Nevertheless, data were consistent with low standard deviations regarding all quantitative parameters. Thus, it is unlikely that a larger sample size would change the outcome of our study. 2) Study population. Only one volunteer was 50 years of age, while the mean age of the study group was 27 years. Since diffusion properties are known to change with age[41] and the young volunteers did not have dental implants, it has to be verified whether the presented technique is applicable in the same way to older patients with dental implants and/or other metallic dental material.

In conclusion, the present study demonstrates the feasibility of DTI of the mandibular nerve using 2-fold-accelerated rs-EPI, which provided similar SNR, quantitative diffusion values, and overall image quality compared to conventional rs-EPI despite considerably faster acquisition. Furthermore, 2-fold-accelerated rs-EPI proved to be applicable in clinical patients in a robust fashion. Further studies assessing patients with a large variety of pathologies of the mandibular nerve are necessary to evaluate the potential clinical impact of the proposed technique.

Acknowledgment

The authors thank Markus Klarhöfer, PhD, Siemens Healthcare Switzerland, for his appreciated support.

Conflict of Interest

Wei Liu is an employee of Siemens Shenzhen Magnetic Resonance Ltd., Shenzhen, China. All other authors declare no conflict of interest. No external funding was received for the current study.

References

1. Tay AB, Lai JB, Lye KW, et al. Inferior alveolar nerve injury in trauma-induced mandible fractures. J Oral Maxillofac Surg 2015;73:1328–1340.
2. Hillerup S, Jensen R. Nerve injury caused by mandibular block analgesia. Int J Oral Maxillofac Surg 2006;35:437–443.
3. Pogrel MA. Damage to the inferior alveolar nerve as the result of root canal therapy. J Am Dent Assoc 2007;138:65–69.
4. Bataineh AB. Sensory nerve impairment following mandibular third molar surgery. J Oral Maxillofac Surg 2001;59:1012–1017; discussion 1017.
5. Seo K, Tanaka Y, Terumitsu M, Someya G. Characterization of different paresthesias following orthognathic surgery of the mandible. J Oral Maxillofac Surg 2005;63:298–303.
6. Hegedus F, Diecidue RJ. Trigeminal nerve injuries after mandibular implant placement—practical knowledge for clinicians. Int J Oral Maxillofac Implants 2006;21:111–116.
7. Chhabra A, Andreisek G, Soldatos T, et al. MR neurography: past, present, and future. AJR Am J Roentgenol 2011;197:583–591.
8. Eppenberger P, Andreisek G, Chhabra A. Magnetic resonance neurography: diffusion tensor imaging and future directions. Neuroimaging Clin N Am 2014;24:245–256.
9. Casselman J, Mermuys K, Delanote J, Ghekiere J, Coenegrachts K. MRI of the cranial nerves—more than meets the eye: technical considerations and advanced anatomy. Neuroimaging Clin N Am 2008;18:197–231, preceding x.
10. Bendszus M, Koltzenburg M, Wessig C, Solymosi L. Sequential MR imaging of denervated muscle: experimental study. AJNR Am J Neuroradiol 2002;23:1427–1431.
11. Filler AG, Kliot M, Howe FA, et al. Application of magnetic resonance neurography in the evaluation of patients with peripheral nerve pathology. J Neurosurg 1996;85:299–309.
12. Filler AG, Maravilla KR, Tsuruda JS. MR neurography and muscle MR imaging for image diagnosis of disorders affecting the peripheral nerves and musculature. Neurol Clin 2004;22:643–682, vi.
13. Andreisek G, Burg D, Studer A, Weishaupt D. Upper extremity peripheral neuropathies: role and impact of MR imaging on patient management. Eur Radiol 2008;18:1953–1961.
14. Takagi T, Nakamura M, Yamada M, et al. Visualization of peripheral nerve degeneration and regeneration: monitoring with diffusion tensor tractography. Neuroimage 2009;44:884–892.
15. Iba K, Wada T, Tamakawa M, Aoki M, Yamashita T. Diffusion-weighted magnetic resonance imaging of the ulnar nerve in cubital tunnel syndrome. Hand Surg 2010;15:11–15.
16. Guggenberger R, Nanz D, Puippe G, et al. Diffusion tensor imaging of the median nerve: intra-, inter-reader agreement, and agreement between two software packages. Skeletal Radiol 2012;41:971–980.
17. Guggenberger R, Nanz D, Bussmann L, et al. Diffusion tensor imaging of the median nerve at 3.0 T using different MR scanners: agreement of FA and ADC measurements. Eur J Radiol 2013;82:e590–596.
18. Simon NG, Lagopoulos J, Gallagher T, Kliot M, Kiernan MC. Peripheral nerve diffusion tensor imaging is reliable and reproducible. J Magn Reson Imaging 2016;43:962–969.
19. Breckwoldt MO, Stock C, Xia A, et al. Diffusion tensor imaging adds diagnostic accuracy in magnetic resonance neurography. Invest Radiol 2015;50:498–504.
20. Hsu JJ, Glover GH. Mitigation of susceptibility-induced signal loss in neuroimaging using localized shim coils. Magn Reson Med 2005;53:243–248.
21. Koch KM, Rothman DL, de Graaf RA. Optimization of static magnetic field homogeneity in the human and animal brain in vivo. Prog Nucl Magn Reson Spectrosc 2009;54:69–96.
22. Porter DA, Heidemann RM. High resolution diffusion-weighted imaging using readout-segmented echo-planar imaging, parallel imaging and a two-dimensional navigator-based reacquisition. Magn Reson Med 2009;62:468–475.
23. Holdsworth SJ, Yeom K, Skare S, Gentles AJ, Barnes PD, Bammer R. Clinical application of readout-segmented-echo-planar imaging for diffusion-weighted imaging in pediatric brain. AJNR Am J Neuroradiol 2011;32:1274–1279.
24. Yeom KW, Holdsworth SJ, Van AT, et al. Comparison of readout-segmented echo-planar imaging (EPI) and single-shot EPI in clinical application of diffusion-weighted imaging of the pediatric brain. AJR Am J Roentgenol 2013;200:W437–343.
25. Holdsworth SJ, Skare S, Newbould RD, Bammer R. Robust GRAPPA-accelerated diffusion-weighted readout-segmented (RS)-EPI. Magn Reson Med 2009;62:1629–1640.
26. Holdsworth SJ, Skare S, Newbould RD, Guzmann R, Blevins NH, Bammer R. Readout-segmented EPI for rapid high resolution diffusion imaging at 3 T. Eur J Radiol 2008;65:36–46.

27. Setsompop K, Gagoski BA, Polimeni JR, et al. Blipped-controlled aliasing in parallel imaging for simultaneous multislice echo planar imaging with reduced g-factor penalty. Magn Reson Med 2012;67:1210–1224.
28. Frost R, Jezzard P, Douaud G, et al. Scan time reduction for readout-segmented EPI using simultaneous multislice acceleration: Diffusion-weighted imaging at 3 and 7 Tesla. Magn Reson Med 2014 [Epub ahead of print].
29. Filli L, Piccirelli M, Kenkel D, et al. Accelerated magnetic resonance diffusion tensor imaging of the median nerve using simultaneous multislice echo planar imaging with blipped CAIPIRINHA. Eur Radiol 2016;26:1921–1928.
30. Manoliu A, Ho M, Nanz D, et al. MR neurographic orthopantomogram: Ultrashort echo-time imaging of mandibular bone and teeth complemented with high-resolution morphological and functional MR neurography. J Magn Reson Imaging 2016;44:393–400.
31. Reeder SB, Wintersperger BJ, Dietrich O, et al. Practical approaches to the evaluation of signal-to-noise ratio performance with parallel imaging: application with cardiac imaging and a 32-channel cardiac coil. Magn Reson Med 2005;54:748–754.
32. Nordmeyer-Massner JA, Wyss M, Andreisek G, Pruessmann KP, Hodler J. In vitro and in vivo comparison of wrist MR imaging at 3.0 and 7.0 Tesla using a gradient echo sequence and identical eight-channel coil array designs. J Magn Reson Imaging 2011;33:661–667.
33. Manoliu A, Spinner G, Wyss M, et al. Magnetic resonance imaging of the temporomandibular joint at 7.0 T using high-permittivity dielectric pads: a feasibility study. Invest Radiol 2015;50:843–849.
34. Landis JR, Koch GG. The measurement of observer agreement for categorical data. Biometrics 1977;33:159–174.
35. Kundel HL, Polansky M. Measurement of observer agreement. Radiology 2003;228:303–308.
36. Khalil C, Hancart C, Le Thuc V, et al. Diffusion tensor imaging and tractography of the median nerve in carpal tunnel syndrome: preliminary results. Eur Radiol 2008;18:2283–2291.
37. Pruessmann KP, Weiger M, Scheidegger MB, Boesiger P. SENSE: sensitivity encoding for fast MRI. Magn Reson Med 1999;42:952–962.
38. Piccirelli M, DeZanche N, Nordmeyer-Massner JA, et al. Carotid artery imaging at 7T: SNR improvements using anatomically tailored surface coils. Proc 16th Annual Meeting ISMRM, Toronto; 2008. p 735.
39. Andreisek G, White LM, Kassner A, Sussman MS. Evaluation of diffusion tensor imaging and fiber tractography of the median nerve: preliminary results on intrasubject variability and precision of measurements. AJR Am J Roentgenol 2010;194:W65–72.
40. Guggenberger R, Eppenberger P, Markovic D, et al. MR neurography of the median nerve at 3.0T: optimization of diffusion tensor imaging and fiber tractography. Eur J Radiol 2012;81:e775–782.
41. Guggenberger R, Markovic D, Eppenberger P, et al. Assessment of median nerve with MR neurography by using diffusion-tensor imaging: normative and pathologic diffusion values. Radiology 2012;265:194–203.
42. Lau AZ, Tunnicliffe EM, Frost R, et al. Accelerated human cardiac diffusion tensor imaging using simultaneous multislice imaging. Magn Reson Med 2015;73:995–1004.
43. Alexander AL, Hurley SA, Samsonov AA, et al. Characterization of cerebral white matter properties using quantitative magnetic resonance imaging stains. Brain Connect 2011;1:423–446.
44. Moisset X, Villain N, Ducreux D, et al. Functional brain imaging of trigeminal neuralgia. Eur J Pain 2011;15:124–131.
45. Neetu S, Sunil K, Ashish A, Jayantee K, Usha Kant M. Microstructural abnormalities of the trigeminal nerve by diffusion-tensor imaging in trigeminal neuralgia without neurovascular compression. Neuroradiol J 2016;29:13–18.
46. Song F, Hou Y, Sun G, et al. In vivo visualization of the facial nerve in patients with acoustic neuroma using diffusion tensor imaging-based fiber tracking. J Neurosurg 2016;125:787–794.
47. Yoshino M, Kin T, Ito A, et al. Combined use of diffusion tensor tractography and multifused contrast-enhanced FIESTA for predicting facial and cochlear nerve positions in relation to vestibular schwannoma. J Neurosurg 2015;123:1480–1488.